DIGITAL OUTCROP MODELS OF THE EAGLE FORD GROUP IN LOZIER CANYON, TERRELL COUNTY, TEXAS

A Thesis

by

DREW EDWARD DAVIS

Submitted to the Office of Graduate and Professional Studies of
Texas A&M University
in partial fulfillment of the requirements for the degree of

MASTER OF SCIENCE

Chair of Committee,	Juan Carlos Laya
Committee Members,	Michael Pope
	Walter Ayers
Head of Department,	Michael Pope

May 2017

Major Subject: Geology

ABSTRACT

The Eagle Ford group was a prolific producer of unconventional oil and gas in south Texas during the last decade. Operators typically target the Lower Eagle Ford formation to drill horizontal wells with lateral lengths averaging nearly 1 mi (1.61 km). Geologic variability can be significant at these distances, thus an understanding of lateral variability of reservoir thicknesses, facies distributions, and fractures paired with geochemical and petrophysical data is valuable in characterizing unconventional reservoirs.

High-resolution digital outcrop models (DOMs) using photogrammetry techniques provide a unique tool to study variability of Eagle Ford group strata in outcrops in Lozier Canyon in Terrell County, West Texas. Stratigraphic variability within the Eagle Ford group is well documented; however, lateral variability of Eagle Ford strata is minimally understood and is fundamental to developing this productive unconventional play. This project focuses on world-class outcrops that expose complete vertical sections of the Eagle Ford group. The study area covers a north-to-south straight line distance of 6.2 mi (10 km) allowing analysis at reservoir-scale.

The average gross stratigraphic thickness of the Eagle Ford group increases by approximately 27.8 ft (8.47 m), a 13.59% increase, from the Scott Ranch site in north Lozier Canyon to south Lozier Canyon. Each Eagle Ford facies increases in thickness from north-to-south Lozier Canyon with Facies C exhibiting the largest percent change in thickness at 20.18%. Skeletal packstone-grainstone bedforms in Facies B are less laterally

continuous up-section from the base of the Sub-facies B2 – B3 contact into the mud-dominated uppermost Facies B (B5). A characterization of fractures traced in two-dimensional (2-D) orthomosaics is related to bedding features in Facies B and Facies C. Fractures are generally shorter (vertically and laterally), more closely spaced, and have higher intensities in Facies B than in Facies C at each respective study site. Furthermore, our findings indicate that, as apparent fracture spacing decreases, apparent fracture dip increases. This inverse relationship between apparent fracture spacing and apparent fracture dip is related to outcrop strike and used to estimate the orientation of dominant fracture sets in Lozier Canyon.

This study highlights the practicality of using unmanned aerial vehicles (UAVs) and photogrammetry techniques to study vast areas of largely inaccessible outcrop. DOMs were interpreted and imported into Schlumberger's Petrel 2014 and will be used to construct improved reservoir models of the Eagle Ford group in future studies. These models may have application in helping to predict subsurface reservoir variability in the Eagle Ford and may be valuable for improving our understanding of other unconventional carbonate mudstone reservoirs, such as the Haynesville and Utica shales.

ACKNOWLEDGMENTS

This research would not be possible if not for generous contributions and funding from Statoil, the Berg-Hughes Center, and the support of Dr. Bruce Hart, Dr. Art Donovan, and Dr. Carlos Dengo. I would like to thank my committee chair, Dr. Juan Carlos Laya, and my committee members Dr. Mike Pope and Dr. Walter Ayers for their guidance and continued support. Dr. Jim DeGraff and Philipp Tesch were instrumental in helping me to complete this research.

I want to extend my thanks to Robert Youens, Billy Foster, Susan Goble, Colonel Lon Ratley, the Judge Roy Bean Visitor Center, and the ranchers of Val Verde and Terrell County, Texas who have been so kind and were willing to help our group collect field data. Field assistance was generously provided by Billy Foster, Philipp Tesch, Julio Batista, Paolo Stefano, Jingqi Xu, Dr. Juan Carlos Laya, Dr. Mike Pope, Roy Conte, and Glenn Davis. Undergraduate students James Martell and Gustavo Beas were extremely valuable in helping me complete this study. Dr. Ryan Ewing, Ryan Baldauf, and Mark McCann were especially helpful in recommending, securing, and maintaining software licenses used in this work. Eric Peavey was very helpful during preparation for my thesis defense.

I would also like to sincerely thank my office mates: Jonathan Sulaica, Philipp Tesch, Xiaodong Zhang, Lisa McLaughlin, and Mario Lira during my time at Texas A&M University. Jonathan, Phil, and Mario were especially kind to me when I was the new guy and I am truly grateful for that. Texas A&M University has been a terrific place

to study and conduct research and I am thankful to the professors for granting me the opportunity to pursue a graduate degree at this prestigious university.

I want to thank Jim Puckette for inspiring me to become a geologist. I would also like to thank Ryan Davis and Paul Guthrie for encouraging me to pursue a master's degree in geology. Jeffery Byrnes, Michael Grammer, Jerid Patterson, and Doug Winzeler were instrumental in guiding and supporting me during my time in the Boone Pickens School of Geology at Oklahoma State University. Jerid and Doug took a chance on me and let me be part of their team at Eland/Sundown Energy to learn and gain experience, and for that I will be forever thankful. Michael Kirkendoll, my undergraduate music professor, was especially kind in helping me in the application process to pursue a graduate degree in geology. He is an excellent music professor and an even better person.

Finally, I would like to thank my best friend and my family for their unwavering support. Jolene was always there to listen, give advice, and support me on the good days and the difficult ones too. Grandmother Nita and Kevin were always there to check-in and encourage me. My mother, father, brother, and sister have helped and encouraged me in everything I have ever done. I could not ask for a better team than our family. Thanks mom, dad, Ryan, and Les.

Drew

CONTRIBUTORS AND FUNDING SOURCES

Contributors

This work was supported by a thesis committee consisting of Professor Juan Carlos Laya and Michael Pope of the Department of Geology & Geophysics and Professor Walter Ayers of the Harold Vance Department of Petroleum Engineering.

Photographs used to build digital outcrop models were acquired by Robert Youens of Camera Wings Aerial Photography. All other work for the thesis was completed by the student independently.

Funding Sources

Graduate study was supported by Statoil under Research Agreement Number M1502747, and a summer 2016 fellowship from the Berg-Hughes Center for Petroleum and Sedimentary Systems at Texas A&M University.

NOMENCLATURE

2-D	Two-dimensional
3-D	Three-dimensional
BL	Brightness Log
CAD	Computer-aided Design
DEMs	Digital Elevation Models
DOMs	Digital Outcrop Models
GCPs	Ground Control Points
GPS	Global Positioning System
GR	Gamma-ray
GS	Grainstone (Dunham Classification)
MS	Mudstone (Dunham Classification)
OAE 2	Oceanic Anoxic Event 2
PS	Packstone (Dunham Classification)
RGB	Red, Green, and Blue
TOC	Total Organic Carbon
UAVs	Unmanned Aerial Vehicles
WGS 84	World Geodetic System 1984
WIS	Western Interior Seaway
WS	Wackestone (Dunham Classification)

TABLE OF CONTENTS

Page

LIST OF FIGURES

Page

LIST OF TABLES

Page

1. INTRODUCTION

High-resolution digital outcrop models (DOMs) are increasingly used as a tool to quantitatively study outcrop geology. DOMs allow geologists to visualize and interpret outcrop using three-dimensional (3-D) reconstruction software. DOMs display 3-D point clouds that allow for the interpretation and correlation of surfaces over large areas that can be comparable to 3-D seismic scale. The advantage that DOMs provide when compared to seismic data is that DOMs have much greater data resolution, often as much as 100 times greater than seismic as suggested by this research. Common industry practice is to analyze geologic reservoirs using large-scale 3-D seismic data and limited well data. The vast difference in resolution between 3-D seismic data and individual well data often results in poor reservoir models (Qiao et al., 2015). DOMs are useful in filling this resolution gap between 3-D seismic and limited well data.

Photogrammetry is a technique used to accurately project 3-D data from two or more two-dimensional (2-D) images of an object, or scene (Birch, 2006). It involves calculating 3-D locations of points shared in two overlapping photographs relative to camera position, which results in 3-D point clouds (Bemis et al., 2014). Point cloud data typically are acquired manually using light detection and ranging (LIDAR) scans, or photographs (Jacquemyn et al., 2015). In the past, photogrammetry was performed manually using photographic film. This method required that film be developed, copied to a positive, scanned and then submitted to triangulation (Leberl et al., 2009). This process was lengthy and led most researchers to prefer LIDAR methods that could

provide more instantaneous results (Leberl et al., 2009). However, with the advent of digital fully-automated photogrammetric workflows, photogrammetry has now surpassed LIDAR scanning in efficiency and accuracy. 3-D automated reconstruction software can easily build 3-D point clouds from LIDAR or photographic data. Once scaled and geospatially referenced, dense point cloud data may be used to measure and analyze outcrop. Image-based photogrammetry can have a geometric accuracy equal to, or greater than, traditional LIDAR data, and photogrammetry point densities may be 100 times richer than LIDAR points (Leberl et al., 2010). Furthermore, with an aerial camera, a flying mission for photogrammetry may be completed in 10% of the time of an aerial LIDAR scan (Leberl et al., 2010). Photogrammetry-based DOMs with integrated geochemical, sedimentological, and physical property data may be implemented to construct subsurface reservoir models and are especially useful in characterizing unconventional petroleum systems such as the Eagle Ford group (Jacquemyn et al., 2015).

Unconventional petroleum systems refer to any petroleum system that relies on special recovery practices such as hydraulic fracturing or steam injection to produce hydrocarbons (Miskimins, 2008). Put simply, unconventional reservoirs contain hydrocarbons, but lack the permeability needed to effectively produce those hydrocarbons without stimulation. Mudstone reservoirs, often loosely referred to as shale, are common unconventional reservoirs. In recent years, unconventional mudstone reservoirs, like the Eagle Ford group have added substantially to the hydrocarbon resources and reserves of the United States. From 2005 to 2015, the United States nearly

doubled its domestic petroleum production and cut net imports of foreign petroleum by more than half, due in large part to unconventional oil and gas resource play development (U.S. Energy Information Administration, 2015).

In the past, unconventional mudstone reservoirs were sometimes described as uniformly homogenous, exhibiting little variability in sedimentological and physical properties. However, this conventional thinking was challenged with the recent surge in unconventional production, as it became increasingly apparent that well-production rates vary significantly within unconventional mudstone resource plays (Donovan et al., 2012). This discrepancy in hydrocarbon production within seemingly similar mudstone reservoirs indicates geologic variability. Considering this geologic variability and the difficulties associated with extracting hydrocarbons from complex unconventional reservoirs, DOMs are a useful tool to display, quantify, and interpret intricate facies variations within these reservoirs. Traditionally, outcrop studies were used to provide qualitative descriptions, however, with technological advancements in computer modelling, outcrops are the object of intensive numerical studies as the oil industry seeks to better understand subsurface reservoirs using outcrops as analogs. As a result, DOMs are instrumental in predicting sweet spots in unconventional reservoirs in the subsurface and are proving a useful tool to improve reservoir models reducing geologic uncertainty (Bowman and Smyth, 2016).

In recent years, the Eagle Ford group was a major producer of unconventional oil and gas in south Texas (Figure 1). Operators typically drill horizontal wells in the Lower Eagle Ford formation with horizontal laterals averaging 4,500 feet (1372 m) in length

(Gardner et al., 2013). Previous outcrop studies indicate the Eagle Ford group is vertically heterogeneous in sedimentary structure, total organic carbon (TOC), bentonite clay content, and faunal assemblage (Donovan and Staerker, 2010; Donovan et al., 2012; Freeman, 1961, 1968; Hazzard, 1959; Lock and Peschier, 2006; Peschier, 2006; Pessagno, 1969; Trevino, 1988). This heterogeneity led the Eagle Ford group to be sub-divided and described in numerous nomenclature schemes as summarized by Donovan and Staerker (2010).

Lozier Canyon and Antonio Creek are dry tributaries to the Rio Grande River in Terrell County, Texas. Lozier Canyon spans approximately 6.2 mi (10 km) north-to-south from U.S. Route 90 to where it spills into the Rio Grande River along the United States – Mexico international border. Cut-bank exposures of Lozier Canyon expose complete sections of the Eagle Ford group at several sites throughout the canyon (Figure 2). Eagle Ford group outcrops in both northern Lozier Canyon and the tributary Antonio Creek were studied in detail; however, recent access to the southern end of Lozier Canyon has provided an abundance of well-preserved outcrops that were never previously studied. High-resolution DOMs constructed using photogrammetry techniques provide a unique opportunity to study lateral continuity of Eagle Ford group strata within these outcrops at reservoir-scale covering an approximate surface area of 0.65 mi^2 (1.68 km^2) and a 3.5 mi (5.63 km) perimeter in southern Lozier Canyon. Over an area this large, drones are especially useful in imaging outcrop quickly from different vantage points that could never be achieved on foot, resulting in accurate 3-D reconstructions of outcrop geology.

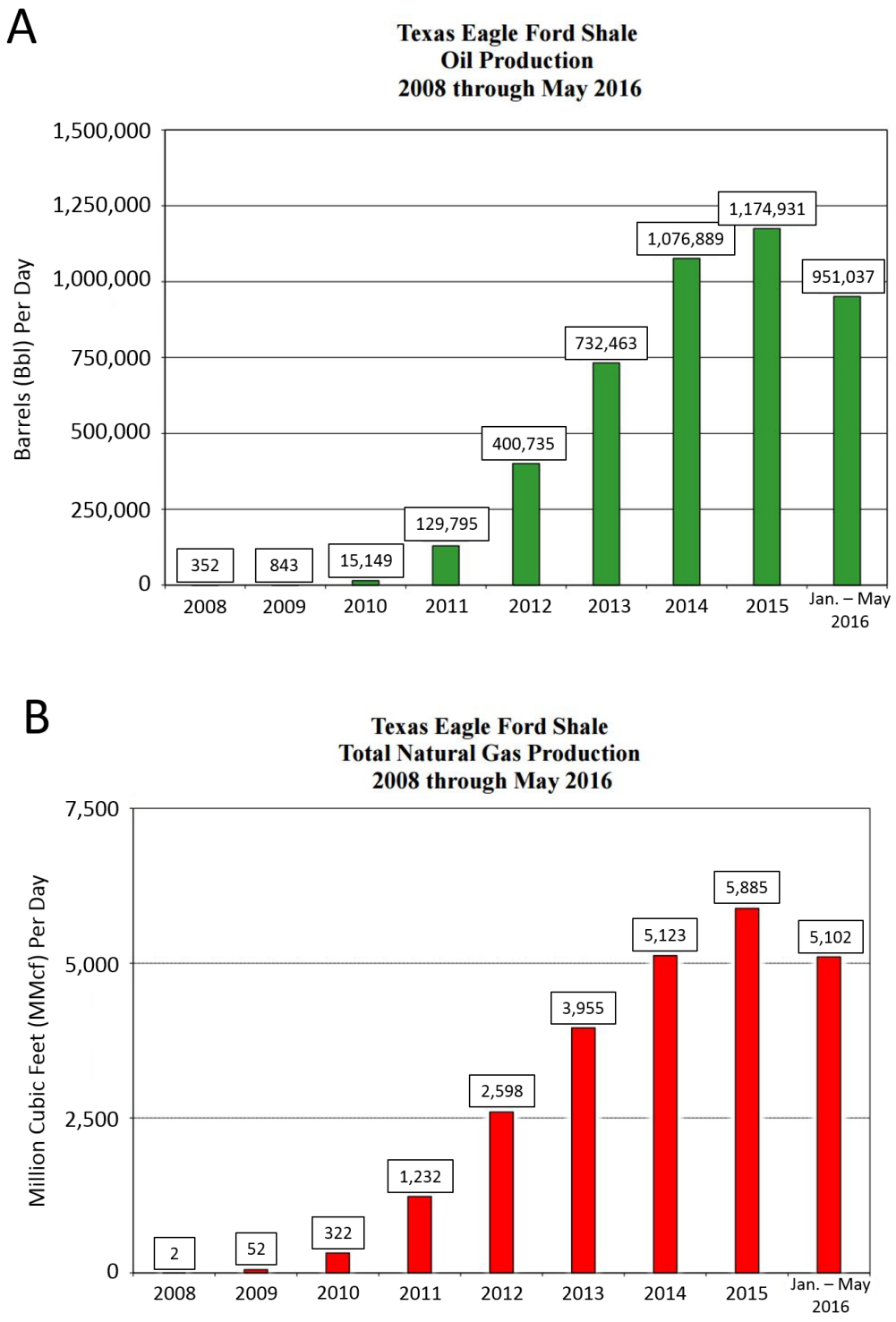

Figure 1. (A) Eagle Ford Total Oil Production from 2008 – May 2016 reported in Barrels Per Day. (B) Eagle Ford Total Natural Gas Production from 2008 – May 2016 reported in Million Cubic Feet Per Day (Railroad Commision of Texas, 2016).

The main objectives of this thesis are to determine the lateral stratigraphic variability of the Eagle Ford group at Lozier Canyon and to characterize fractures and their association with bedding features in primary hydrocarbon-producing zones. We have hypothesized that stratigraphic variability and fracture characteristics can be resolved using DOMs and high-resolution image analysis. Image brightness values, measured from orthorectified photos of Eagle Ford group exposures, are used to generate outcrop brightness logs (BLs). These BLs are useful in differentiating between mudstone and limestone beds, and correlating outcrop with gamma-ray (GR) signatures when acquired under the right conditions: uniform lighting, minimal vegetation, and minimal debris.

This project incorporates data from previous studies in northern Lozier Canyon with southern Lozier Canyon and integrates measured sections, GR profiles, and high-resolution reservoir-scale outcrop modelling of the Eagle Ford group. This model may be used to better understand lateral variability of Eagle Ford group strata in west Texas, and will be used in the future as a framework to supplement with sedimentological, structural, and geochemical data. The resulting model may have applications in characterizing and predicting lateral variability in the south Texas subsurface and analogous unconventional reservoirs around the world.

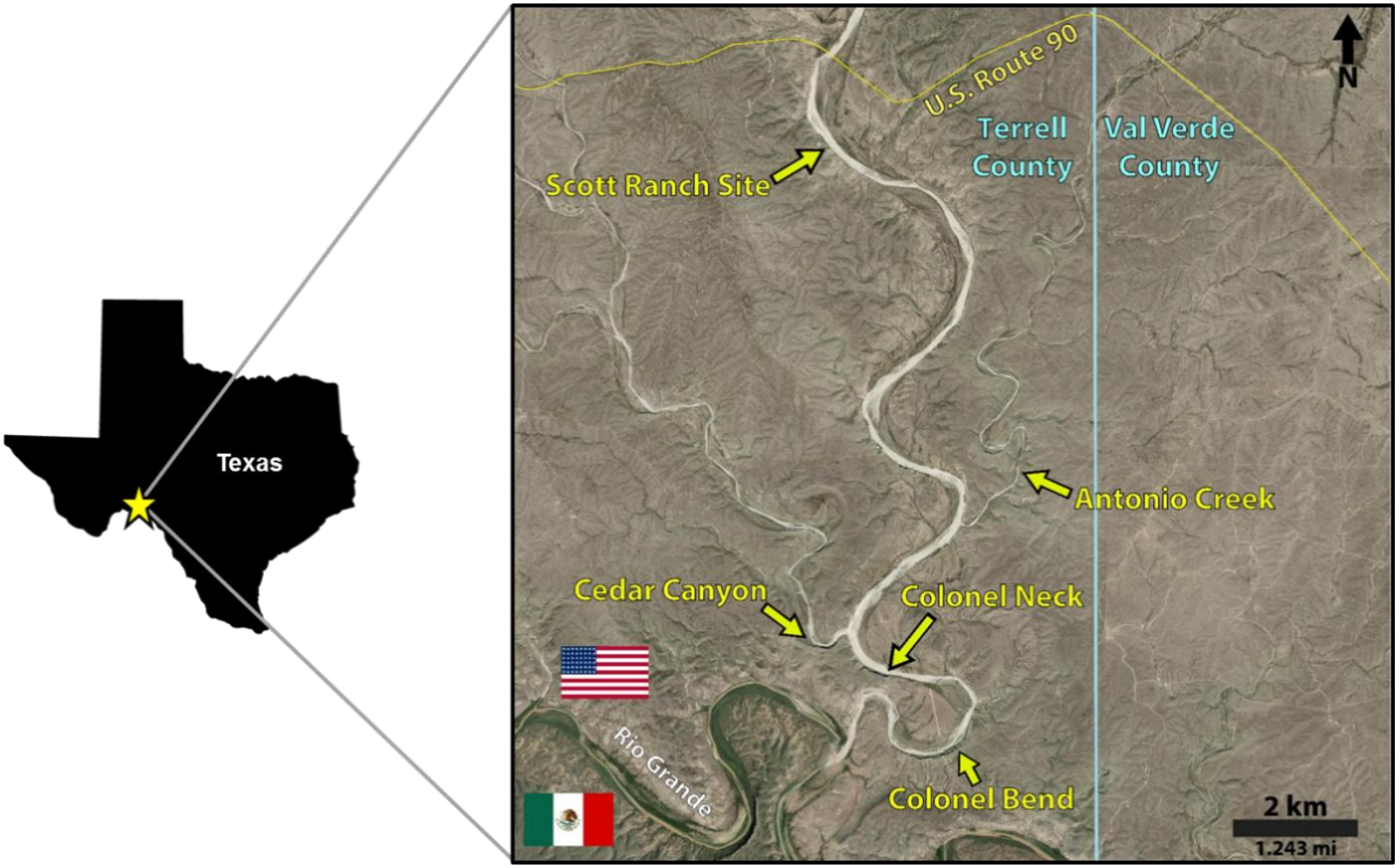

Figure 2. Map view of Lozier Canyon stretching from U.S. Route 90 to the Rio Grande River. The Scott Ranch site, Antonio Creek, and South Lozier Canyon (Colonel Neck and Colonel Bend) were the primary study locations.

2. GEOLOGICAL BACKGROUND

2.1 Geologic Setting and Tectonic History

In the Late Triassic through the Middle Jurassic, an extensional margin setting led to the creation and opening of the Gulf of Mexico (Montgomery et al., 2002). By the end of the Late Jurassic, rifting had mostly ceased and shallow shelf areas had formed around the Gulf of Mexico (Montgomery et al., 2002; Winker and Buffler, 1988). By the Early Cretaceous, the Maverick Basin, an Eagle Ford producing basin located roughly 100 miles (161 km) southeast of the Lozier Canyon area, had begun to form over a rift zone with faults oriented northwest-to-southeast (Hackley, 2012). Rifting in addition to thermal subsidence encouraged increased basinal subsidence and this subsidence may have continued into the Eocene (Workman, 2013). A north-to-northwest trending anticline known as the San Marcos Arch formed in central Texas by the Early-to-Middle Cretaceous (Laubach and Jackson, 1990). This topographic high influenced carbonate deposition across the state as shallow marine environments dominated central Texas along the arch and deeper shelf environments developed on the margins (Workman, 2013).

In the Middle Cretaceous, the earth experienced greenhouse conditions with warming climates and high eustatic sea level favoring expansion of carbonate factories around the world (Barron and Washington, 1984). Average global surface temperatures were likely more than 10° C higher than today, and tropical sea-surface temperatures may have been

as high as 35° C in the Late Cenomanian and Early Turonian (Bice and Norris, 2002; Norris et al., 2002). In south Texas, a north-south trending epicontinental Western Interior Seaway (WIS) developed in a foreland basin formed by flexural subsidence during the Sevier Orogeny (Kauffman, 1977). Carbonate production within the WIS during transgressive maxima led to the development of several carbonate platforms (Figure 3) that coalesced to form the Comanche Platform (Hill, 1887; Scholle et al., 1983; Workman, 2013). Prior to Eagle Ford deposition, rudist reef buildups (Figure 3) developed on the outer margins of the platform shelf (Young, 1972). The paleobathymetry shaped during this period greatly influenced the deposition of the Eagle Ford (Gardner et al., 2013). Lozier Canyon and Antonio Creek are located on what was the southwestern edge of this carbonate platform. The WIS was bordered to the east by a relatively low-relief landmass and to the west by the active Sevier orogenic thrust belt responsible for a significant amount of volcanism throughout the Cretaceous (Deluca, 2016; Scholle et al., 1983).

In the United States, the most complete section of Cretaceous marine strata occurs in the state of Texas (Hill, 1887). A continuous belt of uniform Cretaceous deposits such as the Del Rio, Buda, Eagle Ford, and Austin Chalk units stretch across the state from the northeast to the southwest (Figure 4). Generally, these units dip southward toward the Gulf of Mexico and crop out along the northern side of this Cretaceous belt.

Hill (1887) divided the south Texas Cretaceous into two series known as the Comanchean and Gulfian. The carbonate-dominated Comanchean series referred to the entire Aptian and Albian stages of the Early Cretaceous (Donovan et al., 2016). The

siliciclastic-dominated Gulfian series denoted the Middle to Late Cretaceous, including the Cenomanian and Turonian (Donovan et al., 2016). In south and west Texas, the Comanchean/Gulfian boundary is marked by the Buda Formation and Eagle Ford group contact (Gardner et al., 2013).

The Eagle Ford group was deposited within the unconformity-bounded Zuni sequence which ranged in age from the Middle Jurassic to the Late Cretaceous (Sloss, 1963) during the T6 – R6 Cenomanian-Turonian transgressive-regressive cycle (Donovan et al., 2015; Hart, 2015). The Eagle Ford group was deposited near the maximum flooding surface of this eustatically-driven transgressive sequence at a time when the Tethys seaway (modern Gulf of Mexico) to the south was connected with the Arctic Ocean to the north (Gardner et al., 2013; Hart, 2015). The width of the WIS at this time was nearly 1500 km (932 mi) (Scholle et al., 1983). The Zuni sequence contains Oceanic Anoxic Event 2 (OAE 2) that marks the Cenomanian-Turonian boundary (94.10 ± 0.13 Ma) (Eldrett et al., 2015; Schlanger and Jenkyns, 1976). This boundary is partially preserved at Lozier Canyon and it separates the predominantly anoxic Lower Eagle Ford formation from the dysoxic-to-oxygenated Upper Eagle Ford formation (Donovan et al., 2015; Wehner et al., 2015).

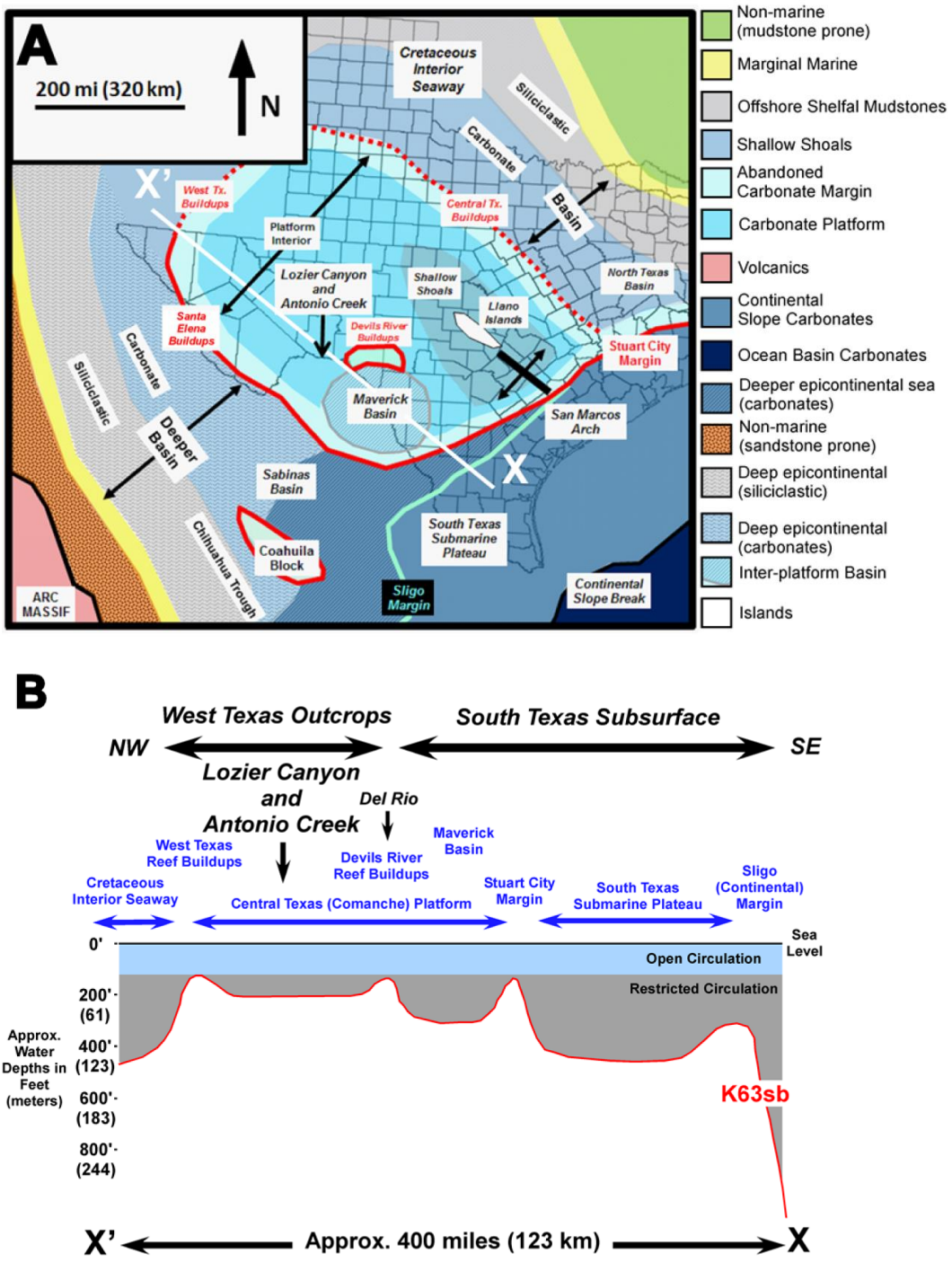

Figure 3. (A) Generalized paleogeographic map of the late Cenomanian Comanche Platform. Reef buildups are illustrated with red lines. (B) Generalized paleotopographic cross section labeled X to X' of the late Cenomanian Comanche Platform. From Gardner et al. (2013).

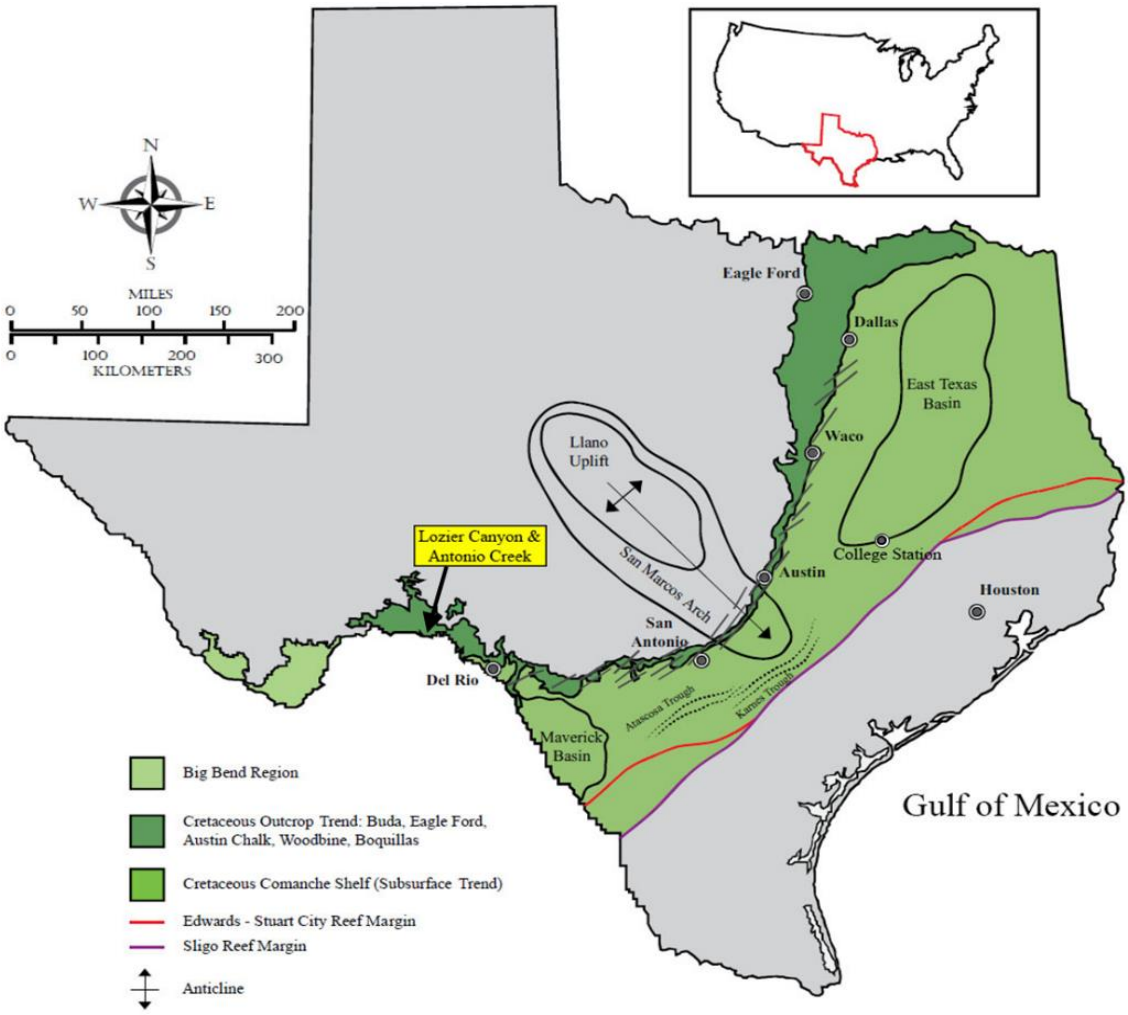

Figure 4. The Cretaceous trend across the state of Texas with the Lozier Canyon and Antonio Creek study site highlighted. Geology of Texas modified after Workman (2013).

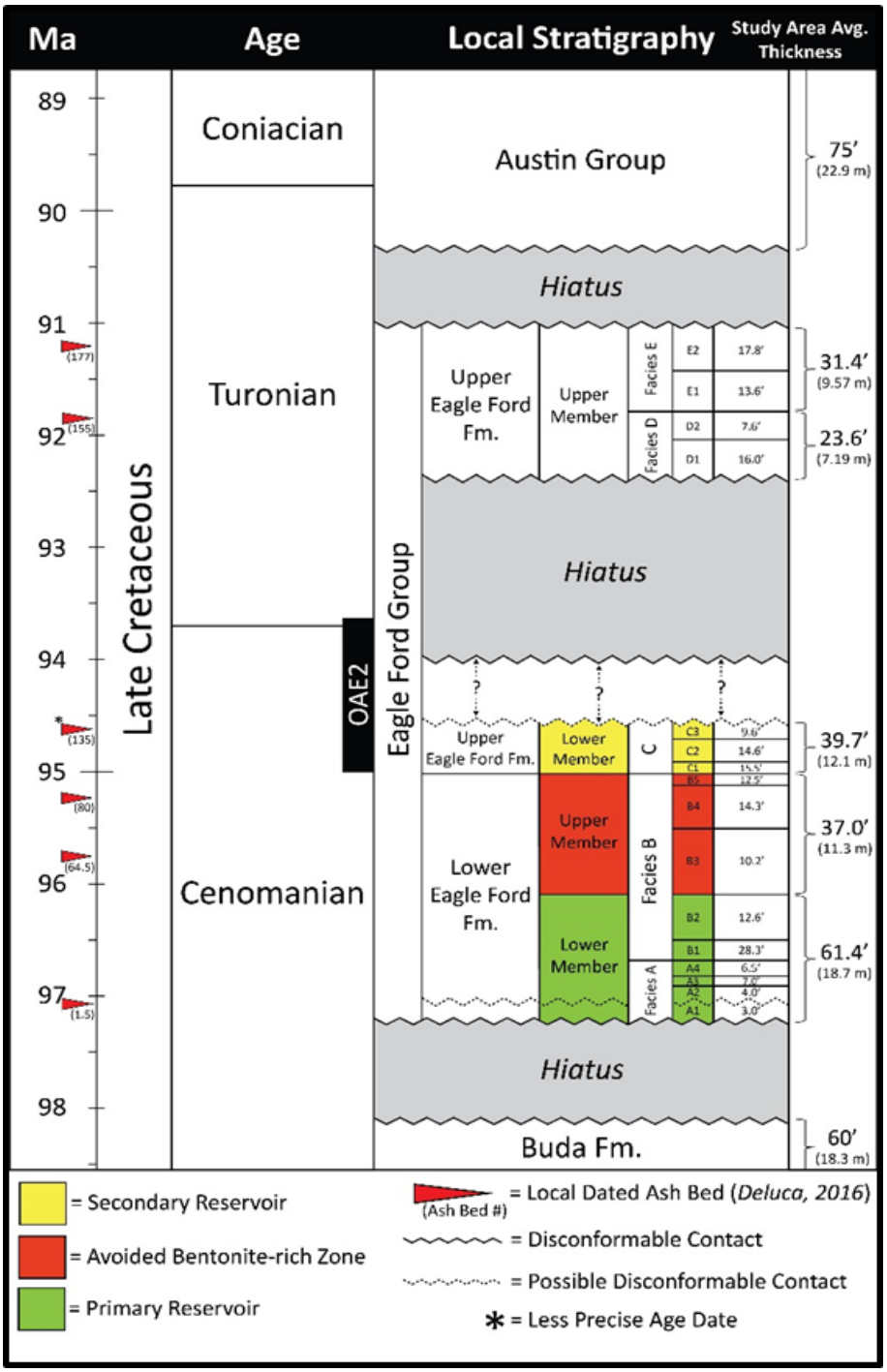

Figure 5. Generalized chronostratigraphic chart of the Eagle Ford group in the Lozier Canyon study area based on ash bed dates from Deluca (2016). Age constraints of deposition of the Eagle Ford group are listed in red. Modified after (Deluca, 2016; Donovan et al., 2016; Freeman, 1968; Wehner et al., 2015).

Lower Eagle Ford Formation ⟸ ⟹ Upper Eagle Ford Formation ⟹

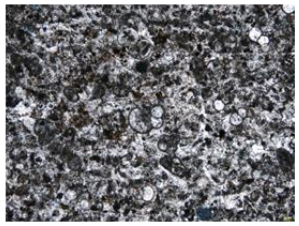

A.) Foraminiferal PS – GS

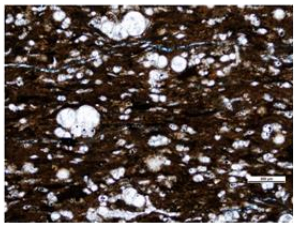

B.) Foraminiferal Mudstone

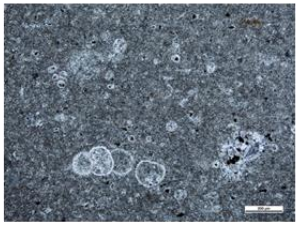

C.) Foraminiferal WS – PS

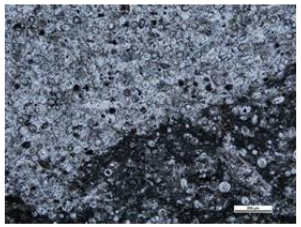

D.) Nodular Foraminiferal Packstone

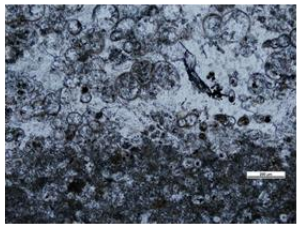

E.) Foraminiferal Packstone

Facies:	A	B	C	D	E
Lithology	Light gray thick bed sets of skeletal grainstone 1-12 in (3-30 cm) interbedded with brownish-gray calcareous mudstone, abundant foraminifera, pellets, bivalves, echinoderm fragments	Dark gray-to-black calcareous-mudstone interbedded with 1-6 in (3-15 cm) skeletal packstone-grainstone; <1-6 in thick (<3-15 cm) bentonite beds; abundant planktonic foraminifera, micrite clasts, common bivalves	Medium gray calcareous mudstone interbedded with 2-12 in thick (6-30 cm) bed sets of skeletal wackestone-packstone; thin <1 in (<3 cm) bentonite beds; abundant foraminifera, bivalves, pellets	1-8 in thick (3-20 cm) nodules of pale-yellow-ochre skeletal wackestone-packstone; bedding destroyed by burrows, interbedded calcareous mudstone; thin <1 in (<3 cm) bentonite beds; abundant foraminifera, pellets, bivalves, brachiopods, ammonites	1-12 in thick (3-30 cm) yellow-ochre skeletal packstone-grainstone; interbedded calcareous mudstone; 1-8 in (3-20 cm) thick bentonite beds; abundant foraminifera, pellets, bivalves, brachiopods
Sed. Structures	Hummocky cross-stratification, wave ripples, soft sediment deformation; horizontal burrows	Abundant horizontal laminations, low-angle inclined laminations, cross stratification, horizontal burrows	Abundant burrows, cross laminations, low-angle inclined laminations, ripple laminations	Abundant burrows; rare preserved cross stratified laminations in nodules	Abundant burrows, ripple laminations, cross stratification
Environment	Restricted shelf episodically above storm wave base; anoxic	Restricted shelf, episodically above storm wave base; anoxic	Open shelf, above storm wave base; oxic	Open shelf, above storm wave base; oxic	Open shelf, above storm wave base; oxic

Figure 6. Description of Eagle Ford facies lithology, sediment structures, and interpreted depositional environments based on Donovan et al. (2012) and Gardner et al. (2013). Thin section images of each Scott Ranch site Eagle Ford group facies acquired by Gardner et al. (2013) are shown above the table.

2.2 Eagle Ford Group Stratigraphy

In West Texas, the Eagle Ford group unconformably overlies the white skeletal wackestone of the Buda Limestone Formation, and is unconformably overlain by the tan and blocky Austin Chalk Formation (Donovan et al., 2015). To be consistent with recent work in west Texas, this research will follow the informal naming convention suggested by Donovan and Staerker (2010), which refers to the gross package of Eagle Ford deposits as the Eagle Ford group. Donovan and Staerker (2010) sub-divided the Eagle Ford group just below the Cenomanian – Turonian boundary into two separate formations: The Lower Eagle Ford formation and the Upper Eagle Ford formation, containing two distinct depositional sequences (Figure 5 & Figure 6) separated by a regional unconformity representing 10's – 100's ky of missing time (Deluca, 2016; Donovan et al., 2012). Donovan and Staerker (2010) further sub-divided the Eagle Ford group into five distinct facies: Facies A (oldest) – E (youngest). The Lower Eagle Ford formation includes Facies A and B, while the Upper Eagle Ford formation contains Facies C, D, and E (Donovan et al., 2012). These facies may be further sub-divided into 16 alphanumeric sub-facies based on GR response (Donovan et al., 2012). The majority of the Eagle Ford group (Figure 5) in west Texas was deposited between 97.14 ± 0.36 Ma and 91.23 ± 0.13 Ma based on zircon dating (Deluca, 2016).

Facies A is the basal unit of the Eagle Ford group (Figure 5 & Figure 6). It unconformably overlies the Buda Formation and signals a drowning event (Hart, 2015). It is approximately 20 – 25 feet (6.1 – 7.6 m) thick throughout the study area and is

composed of alternating thinly laminated beds of brownish-gray calcareous mudstone and light-gray foraminiferal packstone-grainstone beds (PS – GS beds) (Donovan and Staerker, 2010). Individual skeletal PS – GS beds are < 15 cm thick and commonly are discontinuous, pinching out over a length of approximately 9 meters (Lyon, 2015). Cross-bedded sedimentary structures in this unit are interpreted as hummocky and swaley cross-stratification produced by storm events. Contorted bedding and soft sediment deformation are common (Figure 7A). Oyster shells are prevalent at the top of Facies A (Donovan and Staerker, 2010; Donovan et al., 2012). Facies A is not present in producing intervals of the Eagle Ford group in south Texas. In the Lozier Canyon study area, the basal sub-unit of Facies A, Sub-facies A1, is proposed to be remnants of the Pepper Shale based on an abundance of clay, a distinct low resistivity anomaly, and ash bed date (Deluca, 2016; Donovan et al., 2015; Donovan et al., 2016). While there is little evidence, this may imply a disconformable contact between Sub-facies A1 and A2 at Lozier Canyon (Figure 5).

Facies B was deposited directly above Facies A and contains the highest TOC values (> 6% in Sub-facies B1 and B2) of any facies within the Eagle Ford group (Donovan et al., 2012). Facies B is composed mainly of dark gray-to-black organic-rich calcareous mudstone (MS) with few light gray interbedded skeletal PS – GS beds generally less than 6 in (15.2 cm) thick (Figure 6). These skeletal PS – GS beds may be laterally continuous pinch-and-swell beds, or discontinuous beds broken up into lenses (Figure 7B). Generally, these skeletal PS – GS lenses have shorter lens lengths and become less frequent up-section towards the Facies B-C contact. Bentonite ash beds are

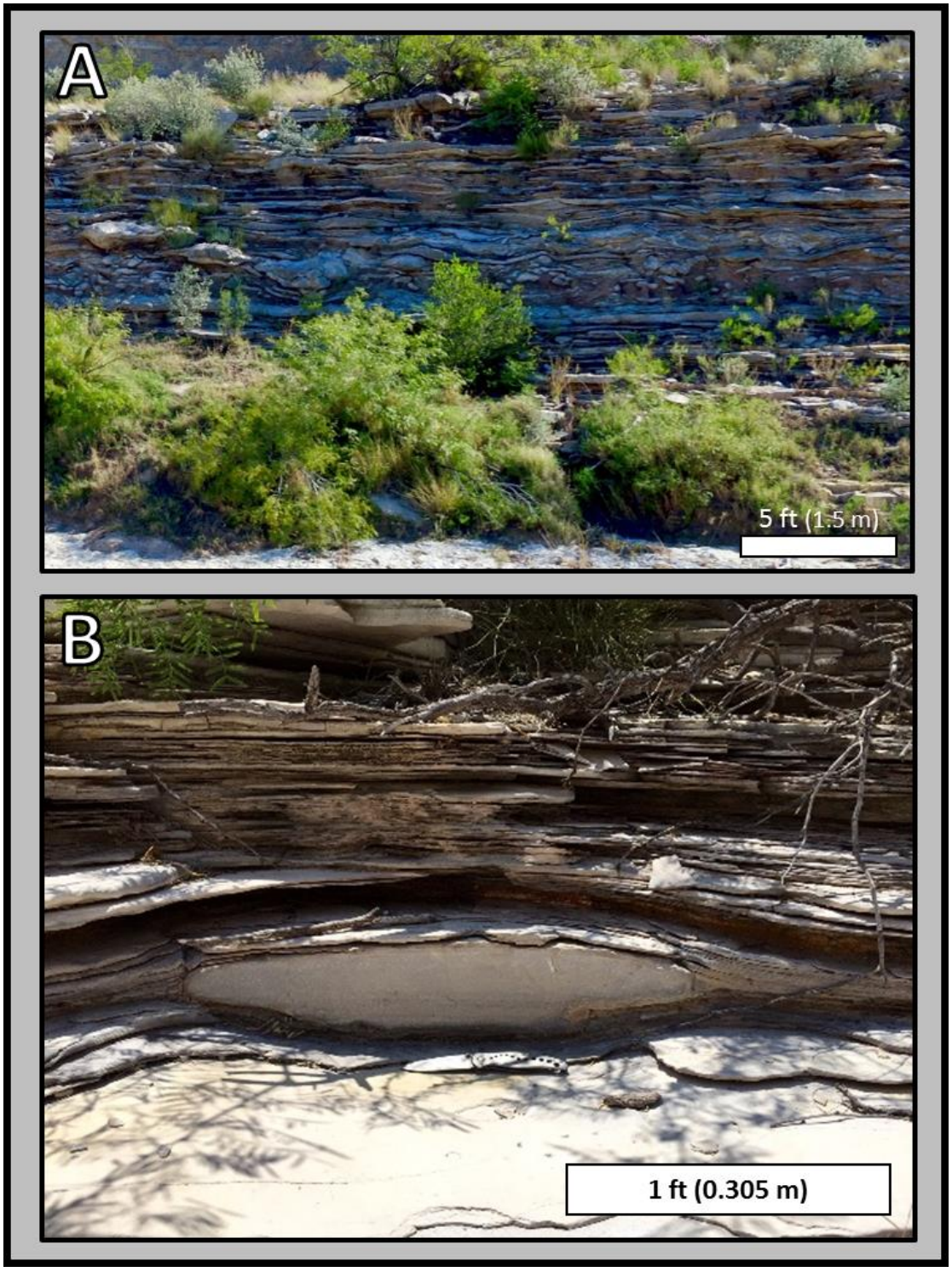

Figure 7. (A) Contorted bedding and soft sediment deformation in the Eagle Ford Facies A at the Colonel Bend site. (B) Skeletal Packstone – Grainstone lens in Eagle Ford Facies B at Antonio Creek.

not very common in Sub-facies B1 and B2. However, they are abundant from the base of Sub-facies B3 (middle-to-upper Facies B) to the Facies B – C contact (Donovan et al., 2012). The influx in bentonite ash beds corresponds to a decrease in TOC values in Sub-facies B3, B4, and B5. Planktonic foraminifera and muddy clasts are present throughout Facies B (Gardner et al., 2013). On average, Facies B is about 70 feet (21.3 m) in thickness throughout the Lozier Canyon and Antonio Creek study area.

Facies C was deposited above Facies B. The Facies B – C contact marks the base of the Upper Eagle Ford formation (Figure 5). It is composed of mostly light gray bioturbated thick-bedded foraminiferal wackestone – packstone beds (WS – PS beds), 8-24 inches (20.3-61 cm) thick, interbedded with brownish gray calcareous mudstone (Figure 6) (Donovan and Staerker, 2010; Donovan et al., 2012). These skeletal WS – PS beds are generally laterally continuous throughout Lozier Canyon. Facies C averages 45 feet (13.7 m) in thickness in the study area, and a few thin bentonite beds are present throughout the unit. The abundance of burrows indicates that the depositional environment experienced more oxygenated conditions (Gardner et al., 2013). The Cenomanian – Turonian boundary is interpreted to be the Sub-facies C2 – C3 contact based on biostratigraphic constraints and the associated $\delta^{13}C$ isotopic excursion profile corresponding to OAE2 (Donovan et al., 2015).

Facies D was deposited unconformably above Facies C (Figure 5 & Figure 8A) and is a yellowish-to-gray, nodular skeletal WS – PS (Figure 6) (Gardner et al., 2013). Echinoids and ammonites are abundant within Facies D, and it is highly burrowed, which destroyed original sedimentary bedding structures explaining the scarcity of well-

preserved laminations (Figure 8B). Facies D has lower TOC values and greater carbonate content than Facies C. Similar to Facies B, lenses of skeletal packstone (PS) that pinch-and-swell laterally are common in Facies D. Facies D is on average about 21 feet (6.4 m) thick and contains massive bentonite beds, with some measuring 4 to 6 feet (1.2 – 1.8 m) thick (Donovan et al., 2012).

Facies E, the uppermost unit of the Eagle Ford group, conformably overlies Facies D and is unconformably overlain by the Austin Chalk. Facies E consists of light gray interbedded foraminiferal grainstone (GS) and thinly-laminated yellow-to-ochre colored calcareous mudstone beds similar to Facies A (Donovan and Staerker, 2010; Donovan et al., 2012). Bentonite beds occur in Facies E, and small hummocks, burrows, and wave ripples commonly are observed sedimentary structures (Gardner et al., 2013). Thickening upward packages of ripple laminated skeletal PS – GS beds occur in Facies E (Gardner et al., 2013). Facies E is approximately 28 feet (8.5 m) thick in the Lozier Canyon and Antonio Creek study area.

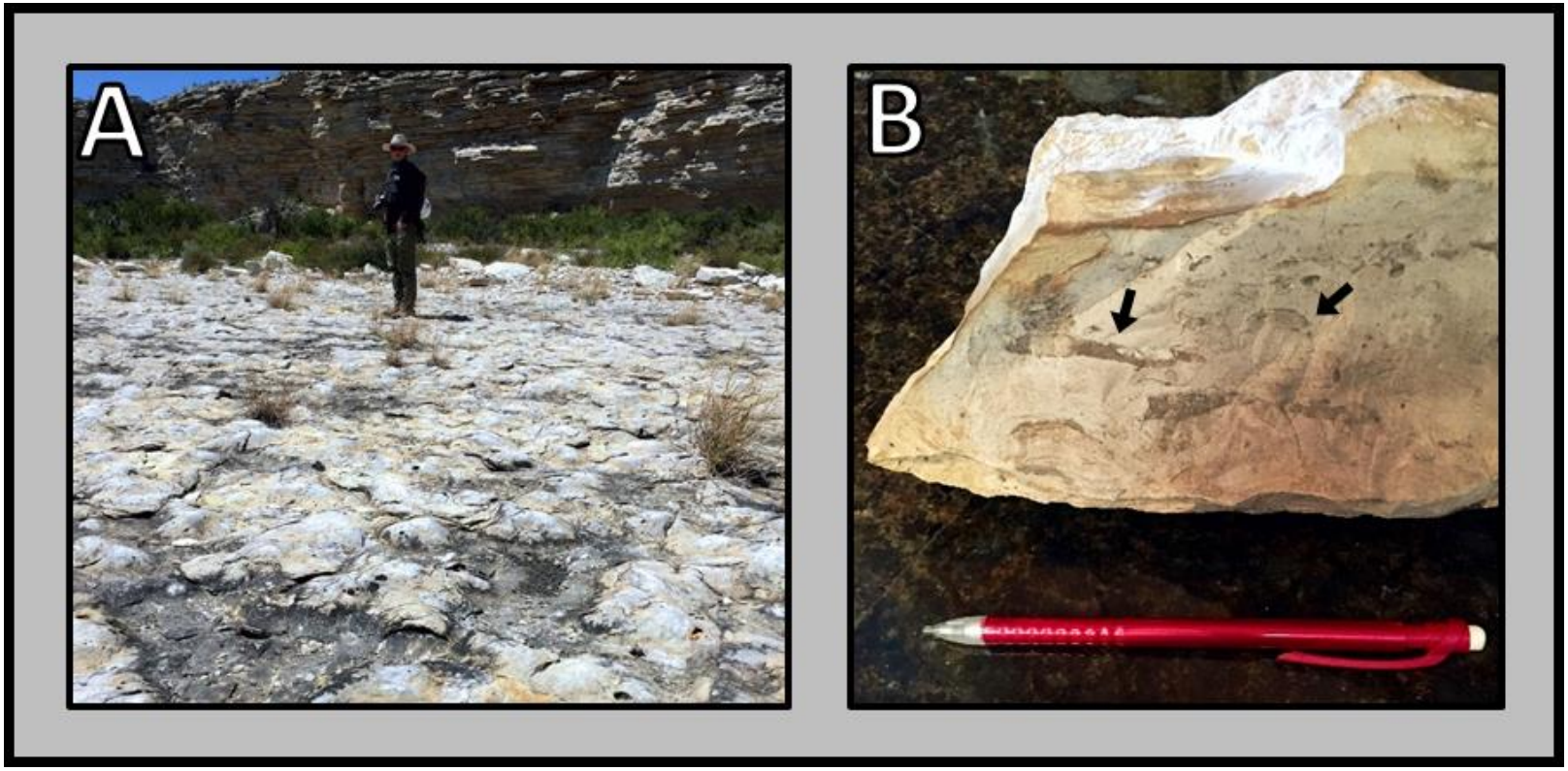

Figure 8. (A) Eagle Ford Facies D Nodular Skeletal Wackestone-Packstone pavement at Antonio Creek. (B) Black arrows indicate *Nereites* trace fossils in the Eagle Ford Lower Facies D located off of U.S. Route 90 near Langtry, TX.

3. METHODS

3.1 Data Collection

Unmanned Aerial Vehicles (UAVs) were used to capture over three thousand high-resolution images (Appendix A) at four primary locations: Scott Ranch site (north Lozier Canyon); Antonio Creek; Colonel Neck site (south Lozier Canyon); and Colonel Bend site (south Lozier Canyon). In this study, the term "south Lozier Canyon" is used to encompass the Colonel Neck and Colonel Bend field sites (Figure 2). At all four primary study locations, UAVs were used to image each outcrop in two different perspectives: aerial map view and outcrop face view (Figure 9). In both views, digital photographs were taken from multiple camera positions in sequential order with 60% overlap between adjacent photographs. Images were captured in this manner so that DOMs could be constructed using photogrammetry techniques. The DZ-3200 Drone Aircraft and Sony ILCE-5100 camera were used to image Lozier Canyon and Antonio Creek in aerial map view. The DJI Inspire 1 Professional UAV and DJI FC550 camera were used to image outcrop faces. Camera and image specifications varied between the two aircraft (Table 1). Orange traffic cones were used as ground control points (GCPs) and were carefully placed next to the outcrop wall at 100 foot (30.48 m) spacing. Global Positioning System (GPS) waypoints with an accuracy of 10 feet (3.048 m) were taken at each GCP. In an effort to insure that each photo had effective overlap, and to improve data processing speed, UAVs flew in a down-and-back flight pattern (Figure 10).

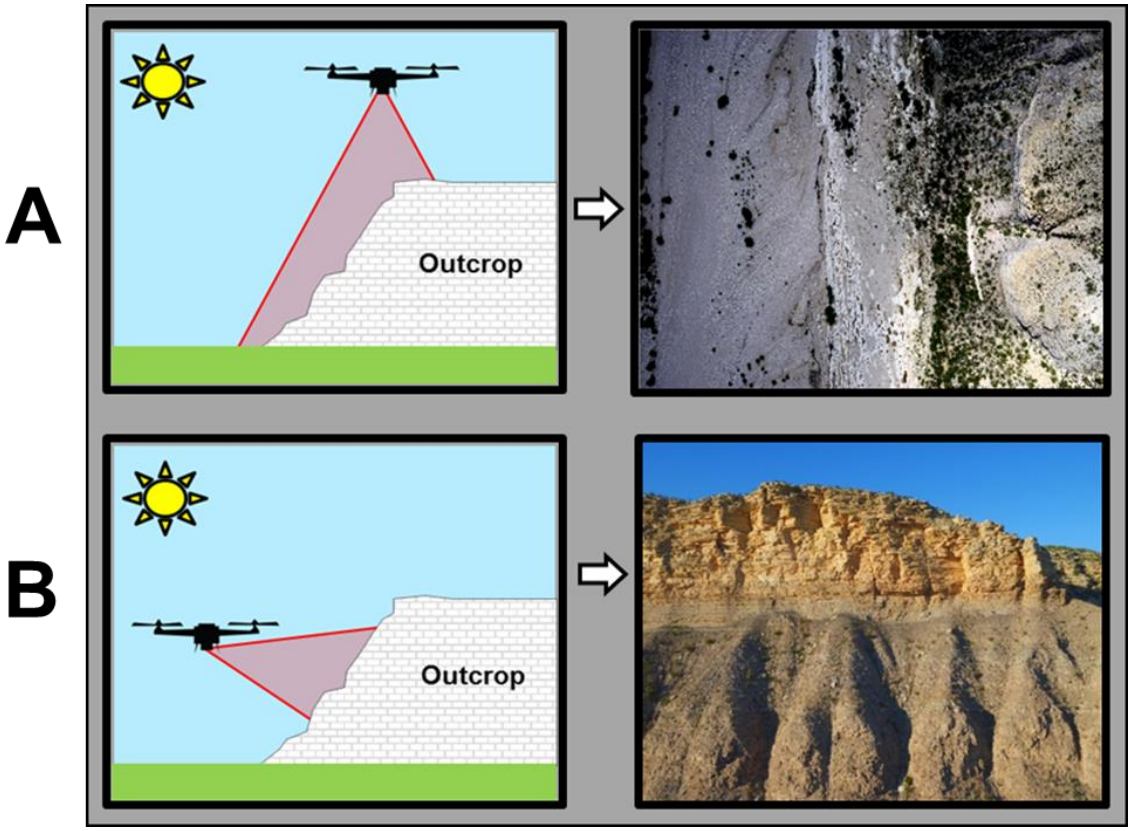

Figure 9. (A) Illustration depicting aerial map view image acquisition with UAV. (B) Illustration depicting outcrop face view image acquisition with UAV.

Table 1. Camera and Image Specifications for UAV Acquired Photographs.

UAV	**View**	**Camera Specifications**			**Image Specifications**	
		Model	*Focal Length*	*Average Exposure*	*Dimensions (width X height)*	*Resolution (Hor. / Vert.)*
DZ-3200	Map	SONY ILCE-5100	20 mm	1/1000 sec.	6000 pix X 4000 pix	350 DPI
DJI Inspire 1 Pro	Faces	DJI FC550	15 mm	1/200 sec.	4608 pix X 3456 pix	72 DPI

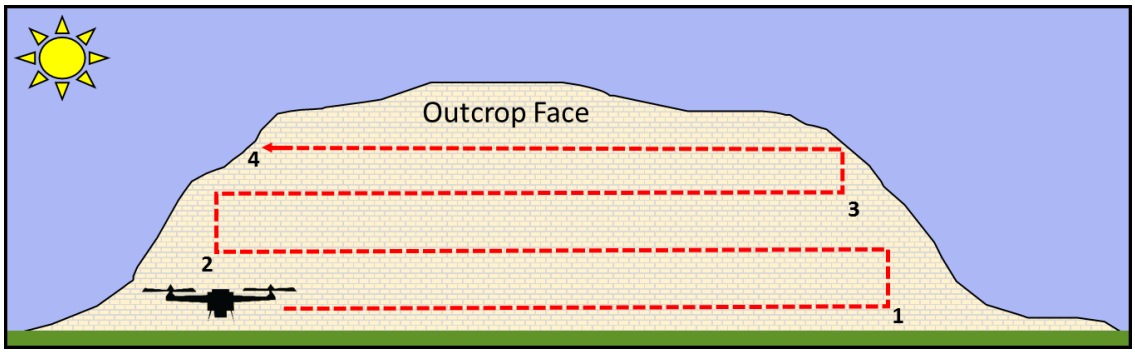

Figure 10. Illustration depicting flight pattern for outcrop view UAV photography.

3.2 Building Digital Outcrop Models

DOMs of the Scott Ranch, Colonel Neck, and Colonel Bend sites were constructed using Agisoft PhotoScan Professional Edition, version 1. 1.6 build 2038 (64 bit). DOMs of Antonio Creek were not produced as part of this study. To construct the models used in this study, photos were first grouped by UAV flight and organized so that overlapping pairs of photos were in order. Photos were then added to a chunk folder in Agisoft PhotoScan and the image quality was estimated. Photos below a 0.5 unit image quality were discarded to maintain a higher model resolution. Once the photos were in order and quality-checked, clipping masks were used to mask objects that were not of interest, such as vegetation and the sky, so that they would not be considered in point cloud generation. This allowed for the software to focus the limited number of tie points on rock features which improved model accuracy. Following masking, camera calibrations were loaded into Agisoft PhotoScan for the two cameras that were used, Sony ILCE-5100 and DJI FC550 (Appendix B). Photos were then aligned using the

specifications depicted in Figure 11. To align photos, the software automatically searched for matching tie points within overlapping photographs to tie one pixel to another. When this process was completed, a thin point cloud was generated. Dense point clouds were then built using specifications depicted in Figure 11.

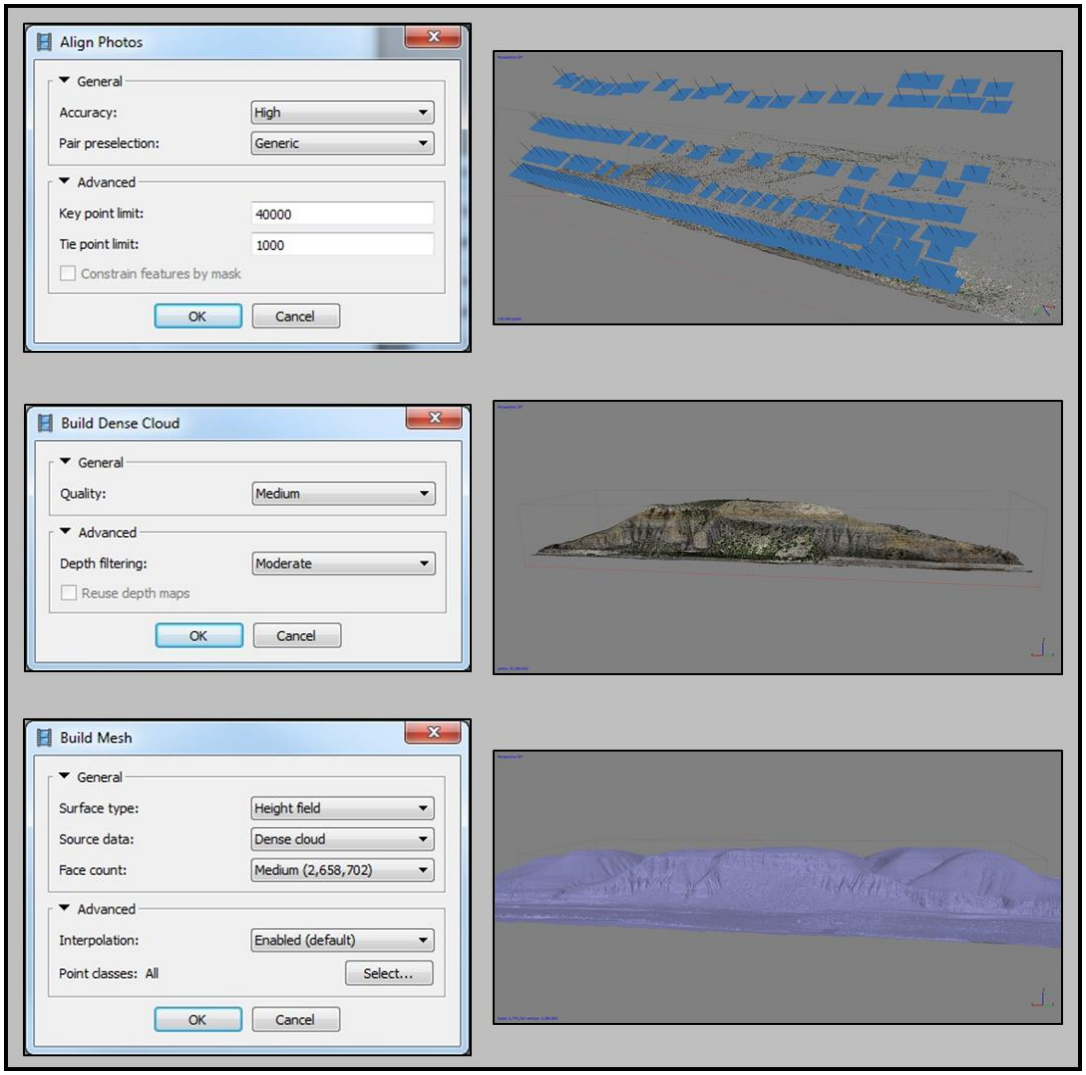

Figure 11. Settings used in Agisoft PhotoScan Professional to produce DOMs. Screenshots of the Scott Ranch site model after completing each step is displayed on the right. Blue rectangles in the align photos screenshot represent camera positions of each photo. A wireframe mesh is displayed in the build mesh screenshot.

Following the generation of a dense point cloud, a mesh was built to interpret and express geometries of the outcrops based on the dense point cloud (Figure 11). After building the dense point cloud, markers were manually placed on GCPs visible in each photograph.

Reference settings were set to World Geodetic System 1984 (WGS 84), and GPS latitude and longitude data for each GCP was entered manually. GPS error accuracy was set at 9.8 feet (3 m). Scale bars were created between each GCP and the scale bar error was set at 0.16 feet (0.05 m). Once all GCPs were entered, reference settings were updated and cameras were optimized to fix estimates of radial distortion coefficients (k1, k2, k3, and k4) and tangential distortion coefficients (p1 and p2). After completing camera optimization, a new and final dense point cloud and mesh were built using the same settings previously described.

3.3 Generating Isopach Maps

After achieving satisfactory results in Agisoft PhotoScan, the georeferenced dense point clouds were exported in LAS file format. The dense point clouds were then imported into Maptek I-Site Studio 5.0 as a scan file. DOMs were cropped to show only features of interest. After a scan was successfully imported and cropped, the spherical triangulation tool was used to create a surface. Once this surface was created, the create line tool was used to interpret surfaces across the outcrop face (Figure 12). The Eagle Ford group facies contact and B2 – B3 Sub-facies contact was interpreted in this manner

at each study site (Scott Ranch, Colonel Neck, and Colonel Bend). Once complete, these lines were saved in the Maptek computer-aided design (CAD) folder. Lines were then exported from the CAD folder as custom text files.

These lines were then imported into Schlumberger's Petrel 2014 software as points with attributes (Figure 13). Surfaces were produced for the Scott Ranch site and south Lozier Canyon (Colonel Neck and Colonel Bend). Isopach maps were created using the surface calculator tool in Petrel 2014. Isopach statistics such as minimum, maximum, mean, range, and standard deviation of thicknesses were generated in Petrel 2014 and exported to Microsoft Excel for data analysis. All Eagle Ford group sub-facies were only able to be reliably interpreted at the Scott Ranch site using the Gardner et al. (2013) measured section and the BP petrophysical logs (Donovan et al., 2015; Donovan et al., 2016). Only the B2 – B3 Sub-facies contact was interpreted at each site because it was distinguishable and critical in defining the lower and Upper members of the Lower Eagle Ford formation.

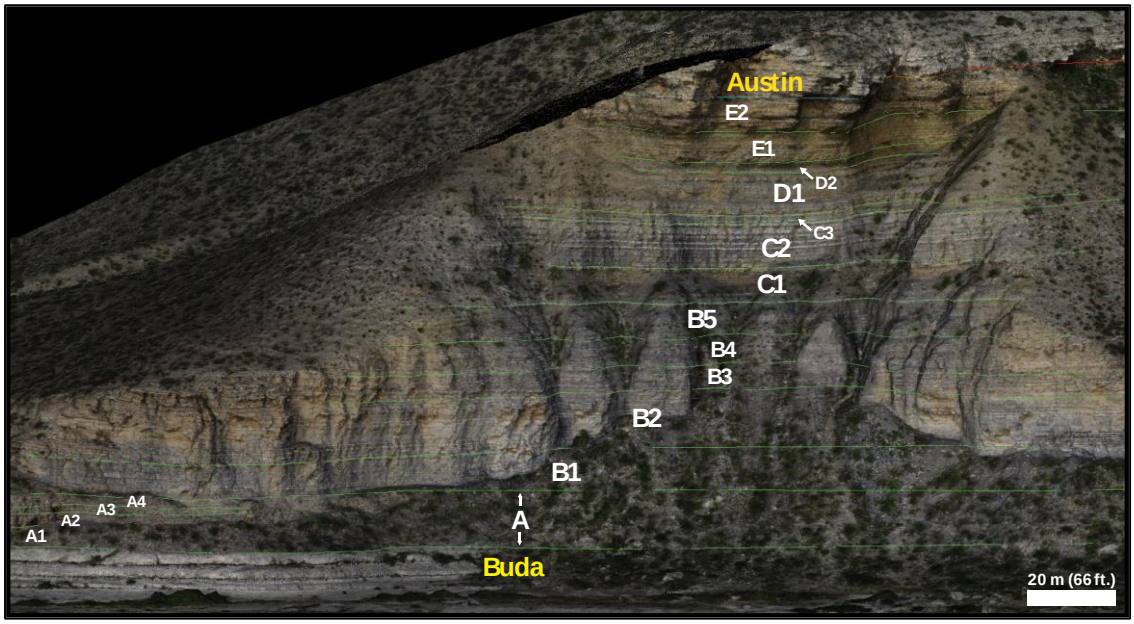

Figure 12. A spherical surface of the Scott Ranch site produced in Maptek I-Site Studio 5.0 with line interpretations for each facies and sub-facies contact of the Eagle Ford group.

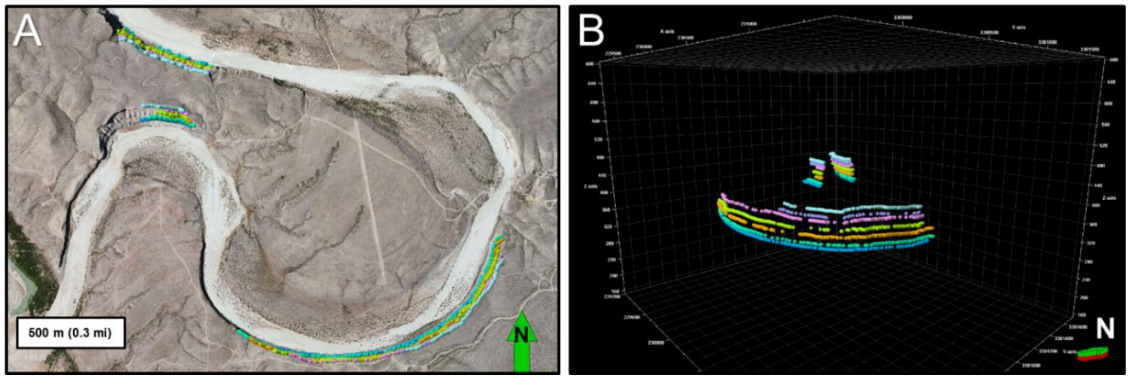

Figure 13. (A) Petrel 2014 imported points with attributes for each Eagle Ford group facies contact. Points are plotted on an aerial map of south Lozier Canyon to show the location of interpreted section. (B) Petrel 2014 imported points with attributes for each Eagle Ford group in south Lozier Canyon shown in a 3-D window.

3.4 Stratigraphic Analysis using High-Resolution Orthomosaics

Stratigraphic analysis was conducted using high-resolution 2-D orthomosaics of outcrop faces at the Scott Ranch site, Colonel Neck site, and Colonel Bend site. 2-D orthomosaics were constructed in Agisoft PhotoScan using the "Build Orthomosaic" tool. Orthomosaics are generated using orthorectification, a process that removes camera distortion and produces high-resolution images useful for mapping outcrop (Bemis et al., 2014). These orthomosaics are of much higher resolution than any produced dense point cloud. Orthomosaics were used to trace prominent skeletal PS – GS lenses in Facies B observable in outcrop. Facies B was specifically chosen for high-resolution stratigraphic analysis because interbedded, and lighter-colored, skeletal PS – GS lenses were identifiable from surrounding mudstone in outcrop imagery, and because Facies B constitutes the primary reservoir produced by operators in the south Texas subsurface. Prominent skeletal PS – GS lenses observable in outcrop faces were traced in Adobe Illustrator Creative Cloud with 1-point stroke lines (Figure 14). Scale bars were drawn in Adobe Illustrator based on DOM measurements. An effort was made to only trace planar outcrop surfaces to avoid potential distortion and inaccurate measurements from 2-D orthomosaics. Once all skeletal PS – GS lenses in the area of interest were traced in Adobe Illustrator, the 2-D orthomosaic background was hidden using the "Layer Visibility" tool in Adobe Illustrator and only the traced lines and scale bar remained visible. This image was exported and saved as a TIF file. The TIF was then opened using ImageJ, which is an image processing and analysis java-based program free to the

public. Scale was entered in the known distance space within the “Set Scale” function. Image type was then changed to 8-bit, and the image threshold was adjusted to a range of 0 – 254. Next, the “Set Measurements” option was selected and the area, standard deviation, bounding rectangle, shape descriptors, and perimeter boxes were checked. Finally, the “Analyze Particles” function was selected and was configured to show trace outlines and display results. After running the analysis, a drawing showing the numbered trace outline of each skeletal PS – GS lens was displayed (Figure 15) along with a results table. Both the drawing and results table were saved. As part of the analysis, the scale bar was also outlined and statistics were generated in a row of the results table for the scale bar. After saving the results table as a CSV file, the file was opened in Microsoft Excel and the scale bar row was deleted from the spreadsheet to correct this issue. Trace lines were then analyzed using the data analysis tool in Microsoft Excel. 2-D trace line measurements represented apparent lens lengths observed in outcrop faces. This process was repeated for each model. It is important to note that not every skeletal PS – GS lens in the area of interest could be analyzed in this study. Only prominent lenses that were observable and not hidden by talus and vegetation were considered (Figure 16).

After intensive study, Facies B was chosen exclusively for analysis. Skeletal WS – PS beds in Facies C were visibly determined to be laterally continuous and mostly correlative across the study area. While there were no observed grainy pinch-and-swell lenses in Facies C, in a few minor occurrences, there were small gaps in otherwise blocky continuous beds. However, it was unable to be determined if this was a product of depositional discontinuity, or simply the result of slope failure, vegetation, or debris

cover. For this reason, a facies analysis was conducted solely on Facies B at the Scott Ranch, Colonel Neck, and Colonel Bend study sites. An analysis of the sub-facies within Facies B was completed at the Scott Ranch site where contacts between Sub-facies B1, B2, B3, B4 and B5 were thoroughly interpreted based on previous field studies.

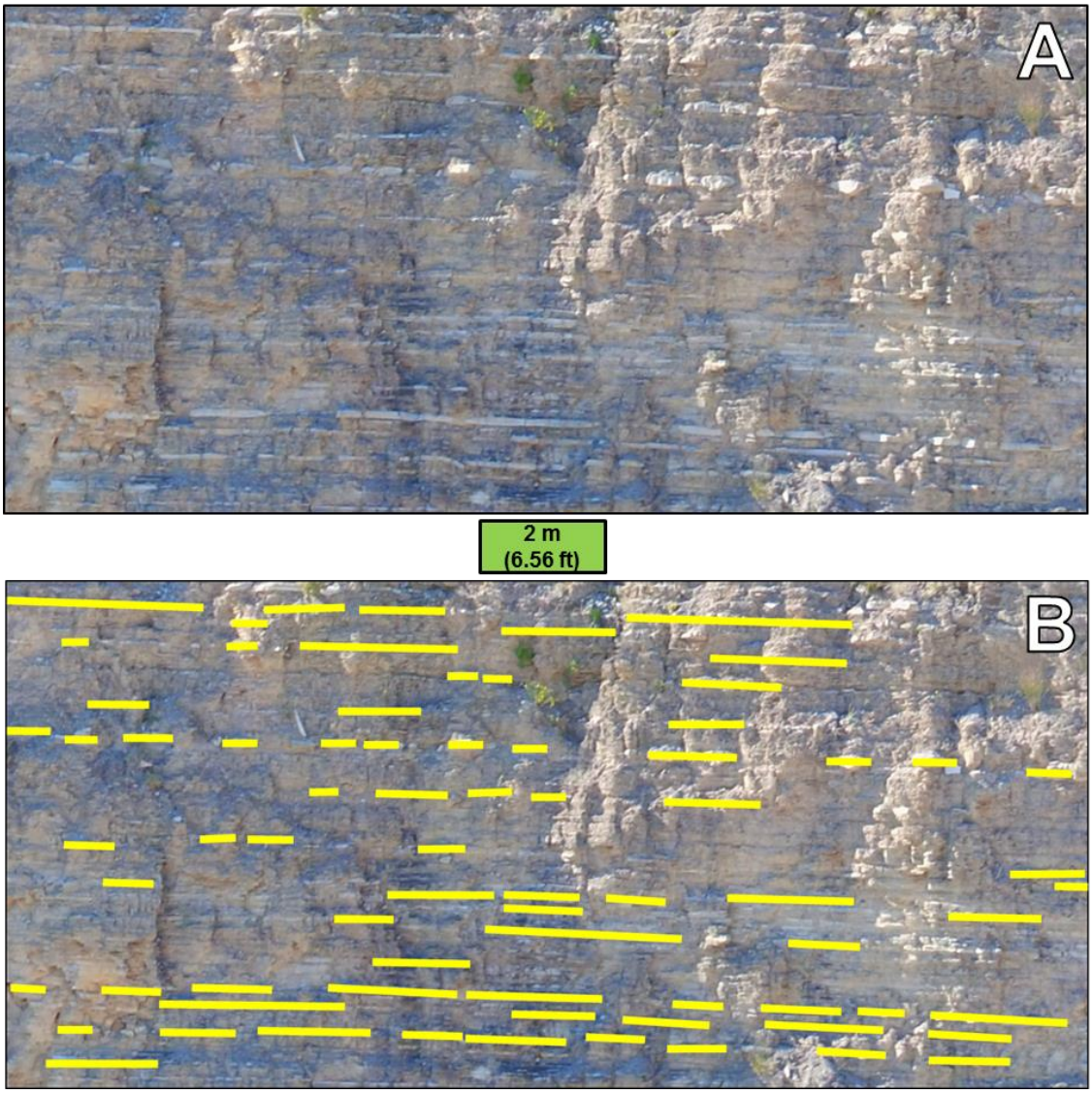

Figure 14. (A) A 2-D photo of Facies B taken from the Colonel Neck North site. (B) Apparent skeletal packstone-grainstone lenses in Facies B are traced in yellow lines.

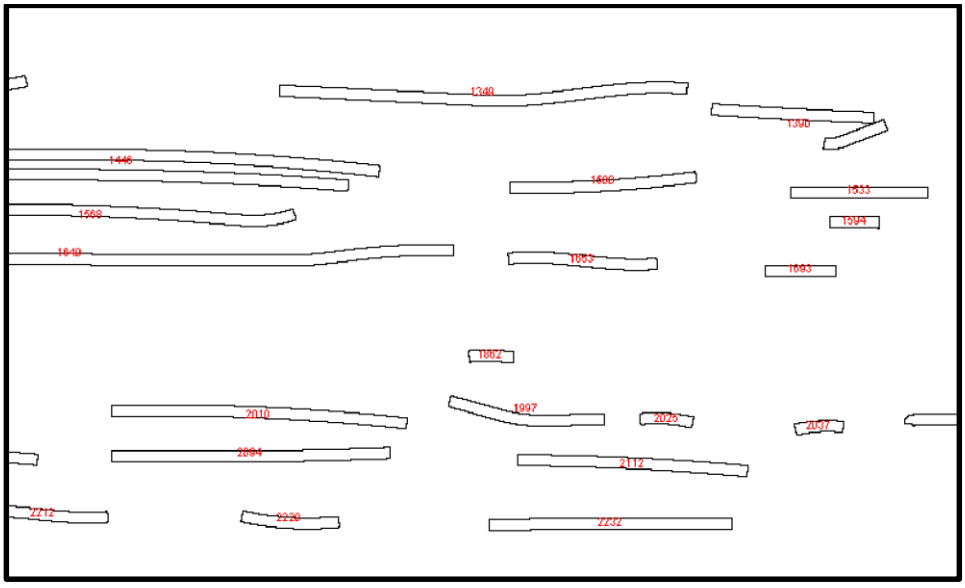

Figure 15. Drawing of outlined skeletal packstone-grainstone traces labeled with red numbers at the Colonel Neck North site analyzed using ImageJ.

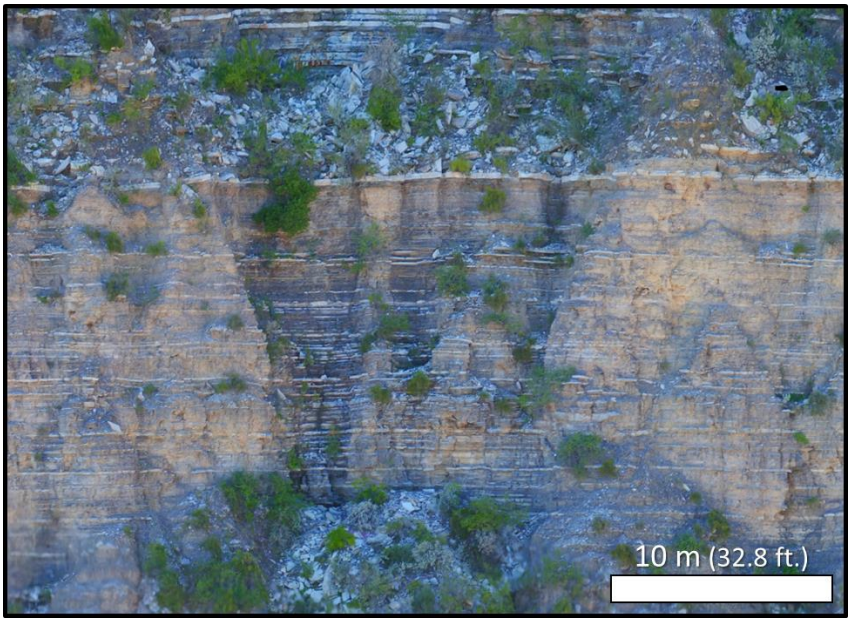

Figure 16. Example of Facies B skeletal packstone-grainstone (PS – GS) lenses discernible in outcrop from the Colonel Neck North orthomosaic. Thinner PS – GS lenses in the more weathered surfaces on the far left and far right side of the image are much more difficult to trace compared to PS-GS lenses in the center of the image which are exposed on a fresher surface with less debris.

3.5 Outcrop Brightness Analysis

Outcrop color and brightness were analyzed using 2-D orthomosaics from three outcrop locations in this study: Scott Ranch North site, Colonel Neck North site, and the Colonel Bend East site. At each site, a vertical line with maximum line thickness was drawn in ImageJ on the exposed outcrop wall from the Buda Formation to the Austin Chalk Formation. Great care was taken in avoiding outcrop with irregular lighting conditions, debris, or vegetation. This resulted in multiple vertical lines that could be combined to form a composite section (Figure 17). Once each vertical line was drawn, the red, green, and blue (RGB) color values were analyzed for the length of the line using the "RGB Measure" tool in the "Plugins" menu. The resulting values characterize the average RGB color values measured across the thickness of the line at a vertical interval of about 2 in (5 cm). These results were saved and exported as CSV files to be analyzed in Microsoft Excel.

In Microsoft Excel, the data from each vertical line was combined to form one composite section. RGB values from each measurement were summed and averaged to yield an average brightness value for each individual measurement (Equation 1). These values were recorded and an outcrop brightness log (BL) was created using these data (Figure 18).

Equation 1

$$Average\ Brightness\ Value = \frac{(Red + Green + Blue)}{3}$$

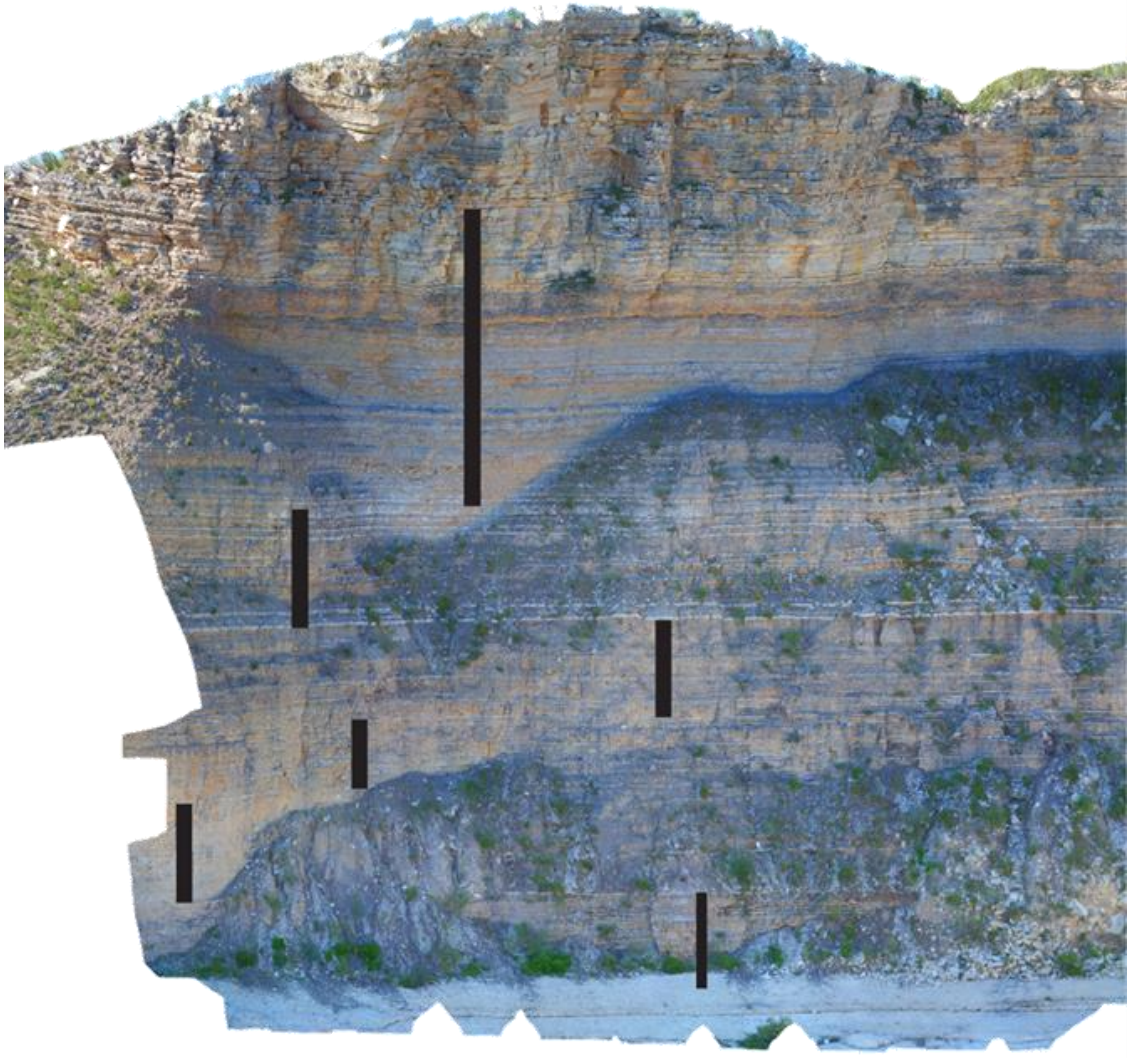

Figure 17. Composite section (black lines) of rock with little debris and vegetation at the Colonel Neck site used to construct an outcrop brightness log. Brightness values for each strip of the composite section were added together to construct one complete composite section for analysis. Debris slopes covered in vegetation commonly form above the Facies A – B & Facies B – C contacts throughout Lozier Canyon. Outcrop measured in this composite section are shaded. Outcrop in the top left of the image provides an extreme example of differential lighting.

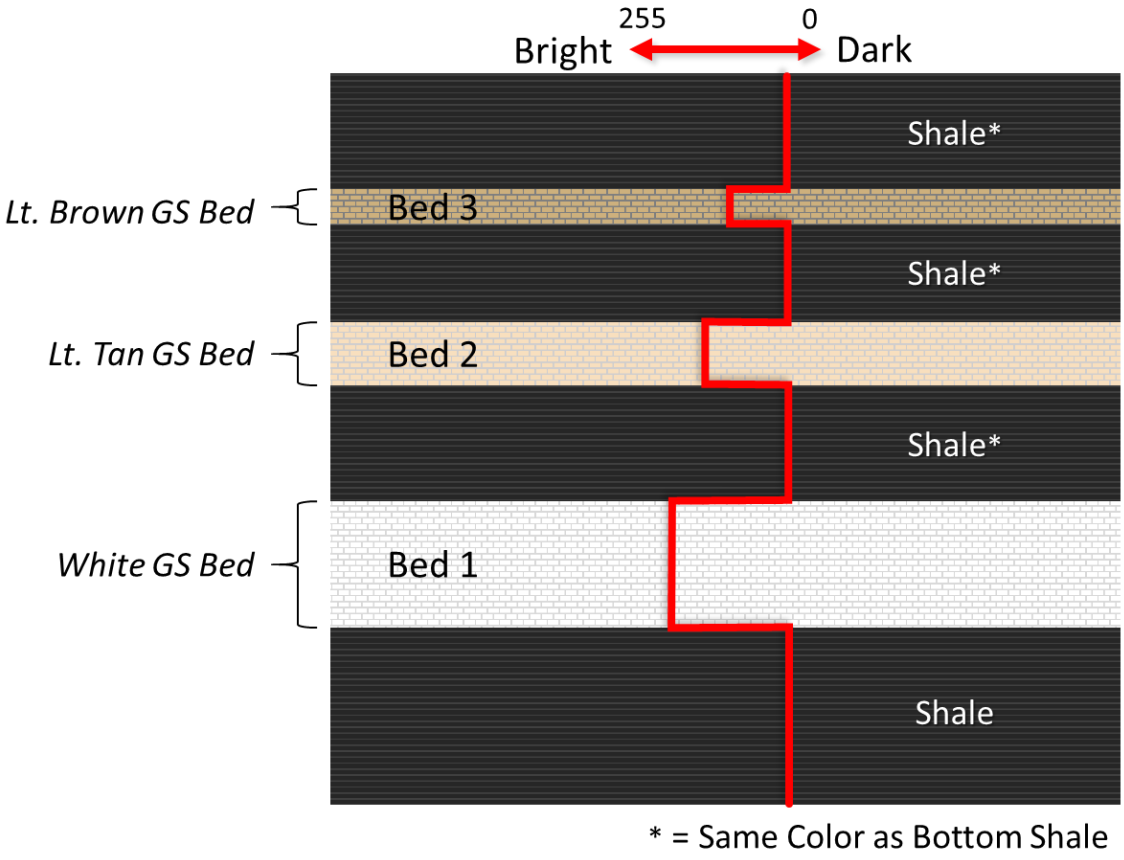

Figure 18. Example of an outcrop brightness log (BL). “0” is the lowest brightness value and “255” is the highest brightness value. Three grainstone (GS) beds are depicted. Bed 1 is brighter than any other bed, thus it has the highest brightness value. Bed 3 is darker than Beds 1 & 2, thus it has the lowest brightness value. Likewise had the shale units differed in color, they too would exhibit variable brightness value responses in the BL.

Outcrop BLs were constructed for two reasons: to attempt to differentiate and quantify the abundance of the two main lithofacies (dark calcareous mud and light grain-rich limestone) in outcrop, and to correlate outcrop brightness to GR logs. This correlation between brightness and GR response assumes that darker-colored beds contain a higher abundance of radioactive elements, whereas lighter-colored beds are less radioactive. Indeed, this link between color and radioactivity in shale was determined by Russell (1945) in determining that darker-colored marine shale are associated with higher radioactivity than lighter colored shale, regardless of the type of organic matter (Russell, 1945). Conversely, unlike marine shales, limestone beds express inherently low radioactivity. Color differences within limestone beds are generally related to mineral pigment and degree of fineness, with the purest limestone beds being lightest in color (McNeal, 1959). Pure limestone beds lack mineral pigments such as glauconite, carbonaceous material, siliceous material, and clays that would increase the radioactivity of the rock (McNeal, 1959). Therefore, it is reasonable to assume that in this marine system the lightest colored limestone marker beds are the purest limestones and consequently have the lowest traces of radioactive elements. Thus, the BL signature of a particular outcrop should mimic to some degree the GR profile of that same outcrop.

An assessment of the abundance of muddy and grainy sediments of each facies of the Eagle Ford group was attempted. A fifth-order polynomial trend line was applied to the BL curve from each study site. This trend line was used as a rudimentary cutoff marking the transition from grain-dominated rock textures to mud-dominated rock textures. Brightness log values greater than the trend line values were considered grain-

dominated texture, whereas brightness log values less than the trend line values were considered mud-dominated texture. Polynomial trend lines were chosen because they best mimicked the sinuous nature of the BLs while accounting for variable lighting of the outcrop and differential weathering. For example, skeletal PS – GS beds in Facies B, which is predominantly mud-dominated, may appear darker than skeletal WS – PS beds in Facies C because of the dark gray-to-black color of the interbedded calcareous mudstone in Facies B. Facies C skeletal WS – PS beds are generally thicker and interbedded with light gray calcareous mudstone which would not stain the grain-rich beds as dark as grain-rich beds in Facies B.

3.6 Measured Sections

Two measured sections were used to quality check the results of DOM measurements. One measured section used was from the south side of the Scott Ranch site (Figure 19) in north Lozier Canyon and was previously measured by Gardner et al. (2013). The other measured section was taken along the southern side of the Colonel Neck site in south Lozier Canyon in this study (Figure 19 & Figure 20). Only measurements of formation contacts and major Eagle Ford group facies contacts (A, B, C, D, & E) were attempted in this measured section because of limited visibility due to slumping, debris, and vegetation (Figure 20). While Eagle Ford group facies measured contacts were considered unreliable due to limited visibility, the Buda Formation – Eagle

Ford group contact and the Eagle Ford group – Austin Formation contact were *in-situ* and readily visible, thus providing reliable measurements to compare with DOMs.

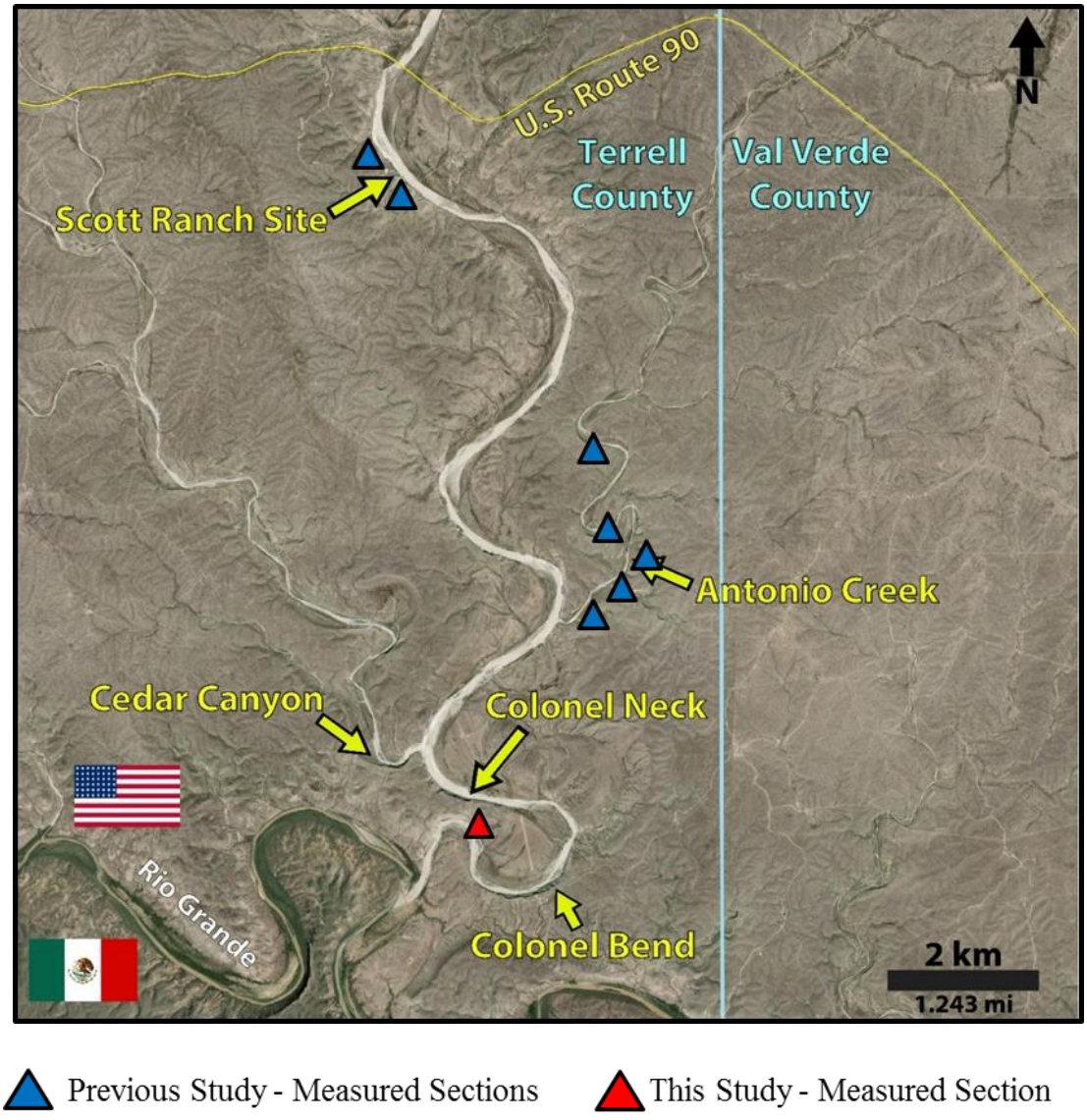

Figure 19. Measured section locations at the Lozier Canyon study area. Blue triangles represent previously acquired measured sections by Gardner et al. (2013). The red triangle indicates the location of the section measured in this study at the Colonel Neck site. Sections at the red triangle and the southernmost blue triangle at the Scott Ranch site were used to quality check DOMs in this study.

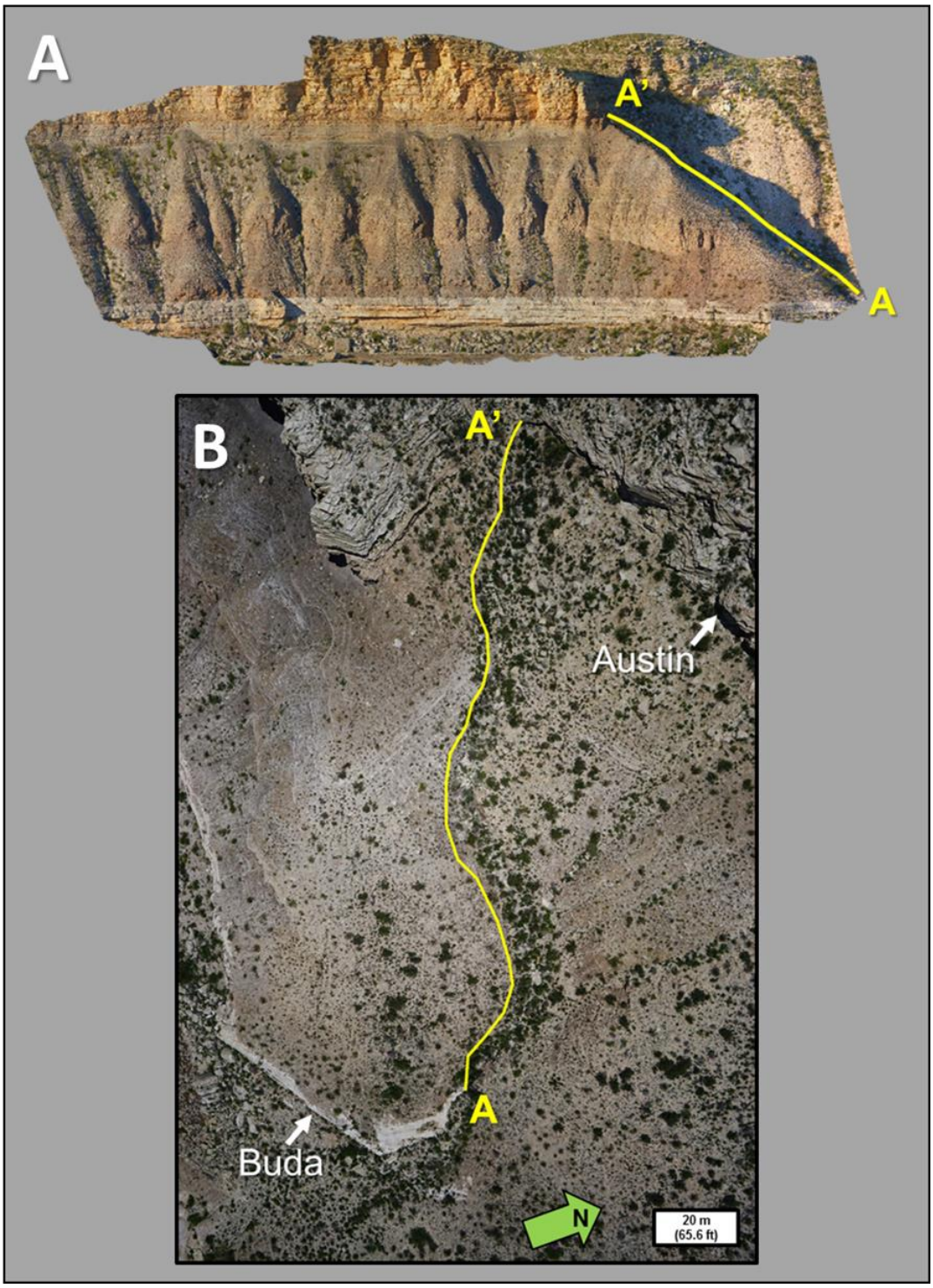

Figure 20. (A) Southern Colonel Neck orthomosaic with yellow line (A – A') indicating measured section path. (B) Aerial view of southern Colonel Neck with measured section path in yellow.

3.7 Fracture Characterization

A simplified fracture analysis was conducted using 2-D orthomosaics of outcrop faces at the Scott Ranch site, Colonel Neck site, and Colonel Bend site. Visible fractures in the Eagle Ford group were traced manually using Adobe Illustrator Creative Cloud software with 1 pt. stroke lines. Apparent vertical and lateral fracture extents, apparent fracture dip, apparent fracture intensity, and apparent fracture spacing were measured using the scaled 2-D orthomosaics in an automated approach with the ImageJ "Analyze Particles" function (Figure 21).

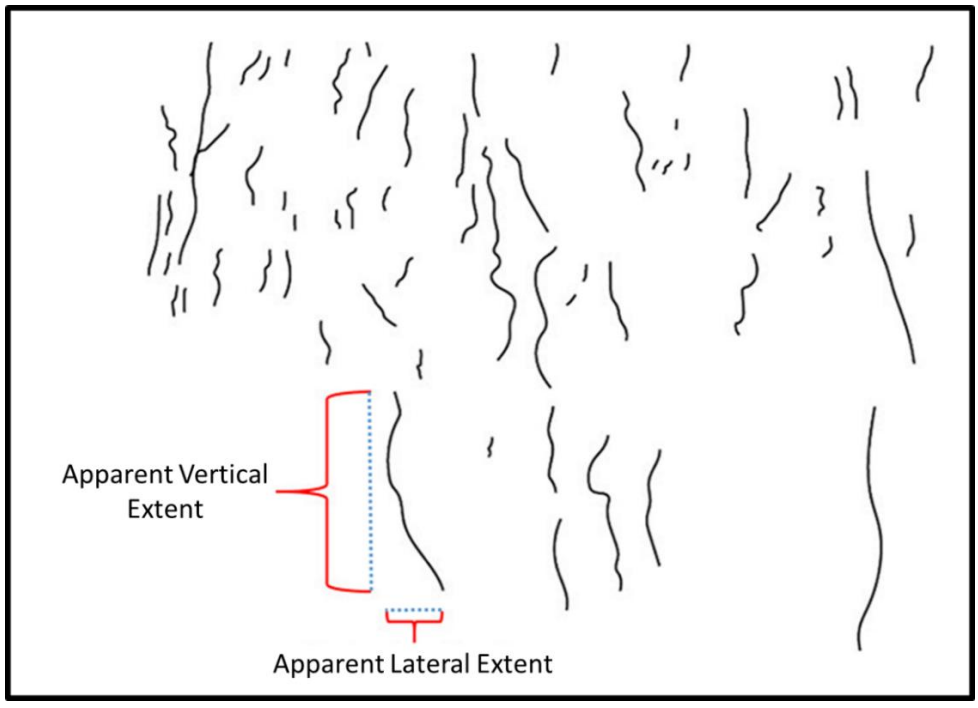

Figure 21. Schematic diagram depicting a vertical projection of fractures intersecting an outcrop face traced from 2-D orthomosaics. Black lines are fractures. Blue dashed lines indicate the apparent vertical and lateral extents of the adjacent fracture and illustrate how measurements were reported in this study. *No vertical exaggeration.*

In total, 10,096 fractures were traced at the three primary study sites. All fractures visible in Facies B and Facies C were traced first in each study site orthomosaic. If a fracture in Facies B or Facies C was through-going into an adjacent facies, such as a fracture that cuts through both Facies B and Facies A, then the fracture was traced to its full visible extent. Likewise fractures in Facies C that extended into Facies D were traced to their full extent. However, fractures that were limited to just Facies A or Facies D without cutting through either Facies B or Facies C were not traced. This was because this fracture study was intended to focus primarily on the two producing reservoir facies: Facies B and Facies C. Lumping fractures in Facies A with Facies B may have yielded misleading results as Facies A does not occur in the producing intervals in south Texas. The few fractures that cut through both Facies B and Facies C were not included in this study as debris at the B – C contact commonly obstructed visibility, and there was a large sample size of isolated fractures from both Facies B and Facies C to study. This methodology, illustrated in Figure 22, was intended to provide approximate fracture characteristics for Facies B and Facies C, the two producing reservoirs in south Texas.

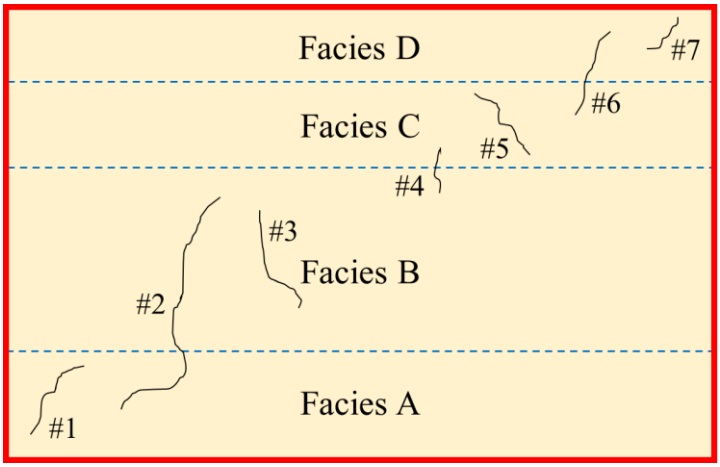

Figure 22. Illustration of the methodology used to characterize fractures from 2-D orthomosaics. Facies contacts are drawn in blue dashed lines. Fractures are numbered, drawn in thin black lines. Fractures #2 and #3 would be counted as Facies B fractures in this study. Fractures #5 and #6 would be counted as Facies C fractures. All other fractures (#1, #4, & #7) would not have been analyzed.

Once Facies B and Facies C fractures were traced, they were analyzed separately at each outcrop. Apparent vertical and lateral fracture extents were measured using the "Analyze Particles" function and reported in the ImageJ results table. Apparent fracture dip was then calculated using Equation 2.

Equation 2.

$$Apparent\ Fracture\ Dip° = \tan^{-1}\left[\frac{Apparent\ Vertical\ Fracture\ Extent}{Apparent\ Lateral\ Fracture\ Extent}\right]$$

To quickly approximate the trace length of each fracture, an apparent hypotenuse extent for each fracture was calculated using the apparent vertical and lateral fracture extents and the Pythagorean theorem (Equation 3). The sum of all apparent hypotenuse extents within a given surface area was then used to calculate a P_{21} apparent fracture

intensity (Equation 4) based on methodology outlined in Mauldon and Dershowitz (2000) and Mauldon et al. (2001).

Equation 3.

$$App.Lateral\ Fracture\ Extent^2 + App.Vertical\ Fracture\ Extent^2 = App.Hypotenuse\ Extent^2$$

Equation 4.

$$Apparent\ Fracture\ Intensity\ P_{21} = \frac{\sum Apparent\ Hypotenuse\ Extents}{Surface\ Area}$$

Apparent fracture spacing was derived by measuring the horizontal distance between fractures in ImageJ. This was accomplished by drawing equally spaced black horizontal lines oriented parallel to bedding planes, and changing the color of fractures from black to white and overlaying them on the equally spaced lines (Figure 23). This allowed for ImageJ to automatically measure the horizontal length of the black lines which represented the distance between fractures using the "Analyze Particles" function.

Dominant fracture orientations of the Eagle Ford group Facies B estimated using Google Earth Pro and field measurements taken from several pavements in side tributary Antonio Creek. Fracture lengths in Antonio Creek pavements were not measured in this study due to debris and vegetation which masked the full length and extent of fracture networks. Properties such as fracture aperture, conductivity, timing, kinematics, and diagenesis are unable to be measured effectively from our DOMs (Casini et al., 2016).

The purpose of a fracture analysis in this study was to provide a basic description of fracture characteristics of the primary subsurface reservoir, Facies B, and secondary reservoir, Facies C, in outcrop.

3.8 Locations for Each Study Component

In this study, each methodology described was conducted at all of the three primary study sites: Scott Ranch, Colonel Neck, and Colonel Bend. However, the exact location within those primary study sites varied. This is mainly attributed to visibility limits and irregular outcrop surfaces. Specific locations for each study component are listed in

Table 2. The relative direction of the study site (ex: Scott Ranch North) indicates what specific side of the outcrop was studied.

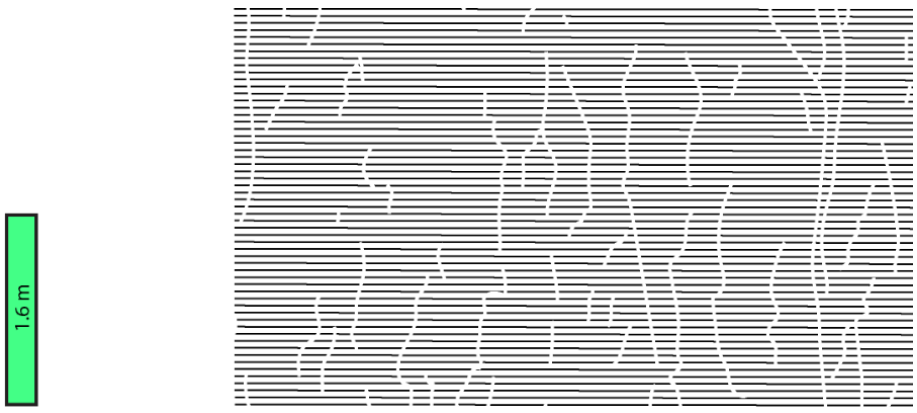

Figure 23. Illustration of methodology used to measure apparent fracture spacing lines on 2-D outcrop orthomosaics. Black horizontal lines are equally spaced and oriented parallel to bedding plane. Traced fractures are colored white and overlay the black spacing lines.

Table 2. Locations for each study component. Eagle Ford Facies Contacts were traced in every DOM. Study locations for stratigraphic analysis of Facies B, outcrop BLs, our measured section, and the fracture characterization were chosen based on visibility which was often limited. Check marks indicate locations of each study component.

Precise Locations for Each Study Component						
	Scott Ranch		**Colonel Neck**		**Colonel Bend**	
Relative Direction:	**North**	**South**	**North**	**South**	**East**	**West**
Latitude: Longitude:	29.893396° -101.808067°	29.889852° -101.804904°	29.813459° -101.796972°	29.809182° -101.794663°	29.803305° -101.782862°	29.801472° -101.792513°
Eagle Ford Facies Contacts	✓	✓	✓	✓	✓	✓
Stratigraphic Analysis (Facies B)	✓		✓		✓	✓
Outcrop BLs	✓		✓		✓	
Measured Section				✓		
Fracture Char.	✓		✓			✓

4. RESULTS

4.1 Stratigraphic Variability

Stratigraphic thicknesses of the overall Eagle Ford group, as well as each facies (A, B, C, D, E) and member (Lower Eagle Ford formation: Lower & Upper member; Upper Eagle Ford formation: Lower & Upper member) of the Eagle Ford group were determined from DOMs at the Scott Ranch site and south Lozier Canyon. Results from the Scott Ranch and south Lozier Canyon sites compared favorably with adjacent measured sections (Figure 24).

4.1.1 Eagle Ford Group

DOM results suggest that the total Eagle Ford group increases in average thickness from the northern Scott Ranch site (176.8 ft (53.89 m)) to south Lozier Canyon area (204.6 (62.36 m)) by approximately 27.8 ft (8.47 m) representing an increase in average stratigraphic thickness of 13.59% (Figure 25 & Figure 26), with a maximum thickness range of 46.7 ft (14.23 m). At the Scott Ranch site, the Eagle Ford group average thickness is 176.8 ft (53.88 m) with a minimum thickness of 173.2 ft (52.79 m) and a maximum thickness of 182.7 ft (55.68 m) (Table 3). In south Lozier Canyon, the Eagle Ford group average thickness is 204.6 ft (62.36 m) with a minimum thickness of 191.7 ft (58.44 m) and a maximum thickness of 219.9 ft (67.03 m) (Table 4). In Antonio

Creek, slightly east of Lozier Canyon, the Eagle Ford group is about 182.5 ft (55.6 m) thick (Gardner et al., 2013). Isopach maps of the Eagle Ford group within south Lozier Canyon indicate increased thickening toward the northeast (Figure 27).

4.1.2 Eagle Ford Formations

The Lower Eagle Ford formation has an average thickness of 93.4 ft (28.47 m) at the Scott Ranch site (Figure 26A; Table 3). In south Lozier Canyon, it has an average thickness of 105.85 ft (32.26 m) indicating a 12.45 ft (3.79 m) and 11.76% increase in average thickness from north-to-south Lozier Canyon (Table 4; Table 5). In Antonio Creek, the Lower Eagle Ford formation is about 96 ft (29.3 m) thick (Gardner et al., 2013). Isopach maps from DOM measurements of south Lozier Canyon show thickness gradually increasing eastward (Figure 28).

The Upper Eagle Ford formation has an average thickness of 83.9 ft (25.57 m) at the Scott Ranch site (Figure 26A; Table 3). In south Lozier Canyon, it has an average thickness of 99.19 ft (30.23 m) indicating a 15.29 ft (4.66 m) and 15.41% increase in average thickness from north-to-south Lozier Canyon (Table 4; Table 5). In Antonio Creek, the Upper Eagle Ford formation is about 86.5 ft (26.2 m) thick (Gardner et al., 2013). Isopach maps from DOM measurements of south Lozier Canyon show thickness gradually increasing to the east (Figure 29).

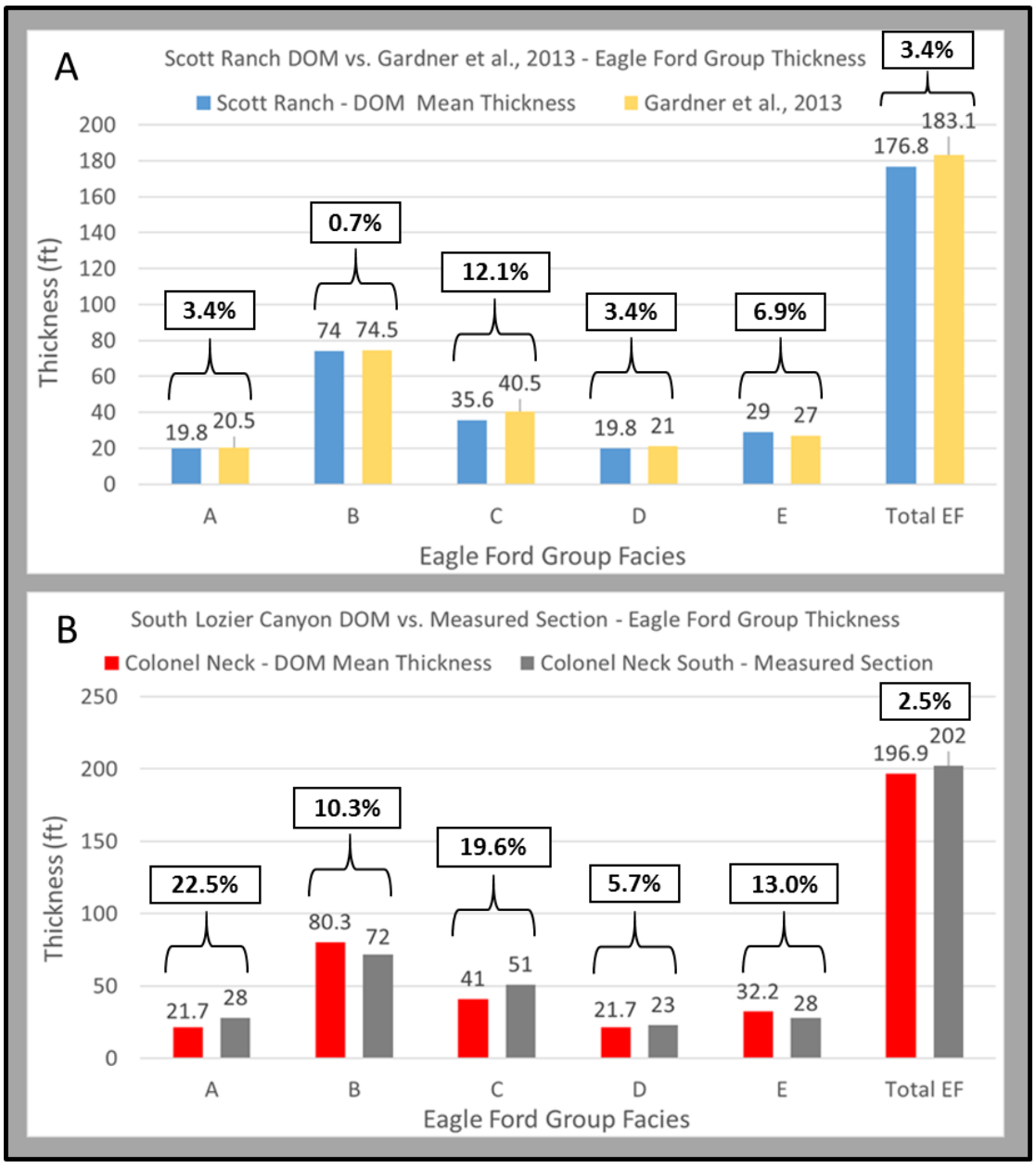

Figure 24. (A) Eagle Ford group mean thickness results from Scott Ranch DOM compared with Gardner's (2013) measured section. Percent difference in values are shown above bar graphs. (B) Eagle Ford group mean thickness results from the Colonel Neck site compared with the measured section taken from the southern Colonel Neck area. Facies thickness values for this measured section are unreliable. However, the total Eagle Ford group thickness value of 196.9 ft (60.02 m) is accurate with only a 2.5% difference between DOM measurements and hand-measured thickness.

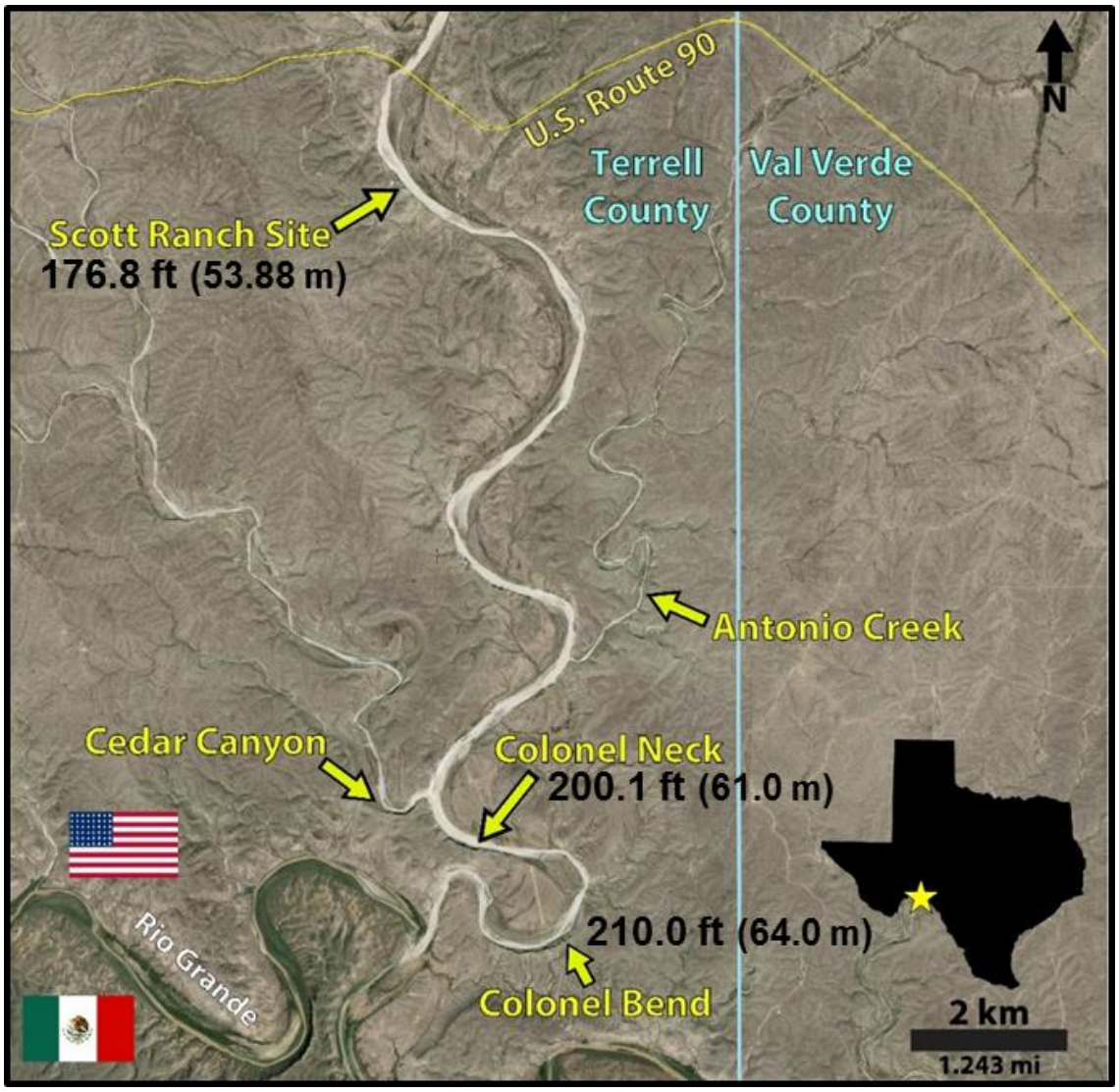

Figure 25. Annotated map of generalized mean thickness variation of the total Eagle Ford group in Lozier Canyon.

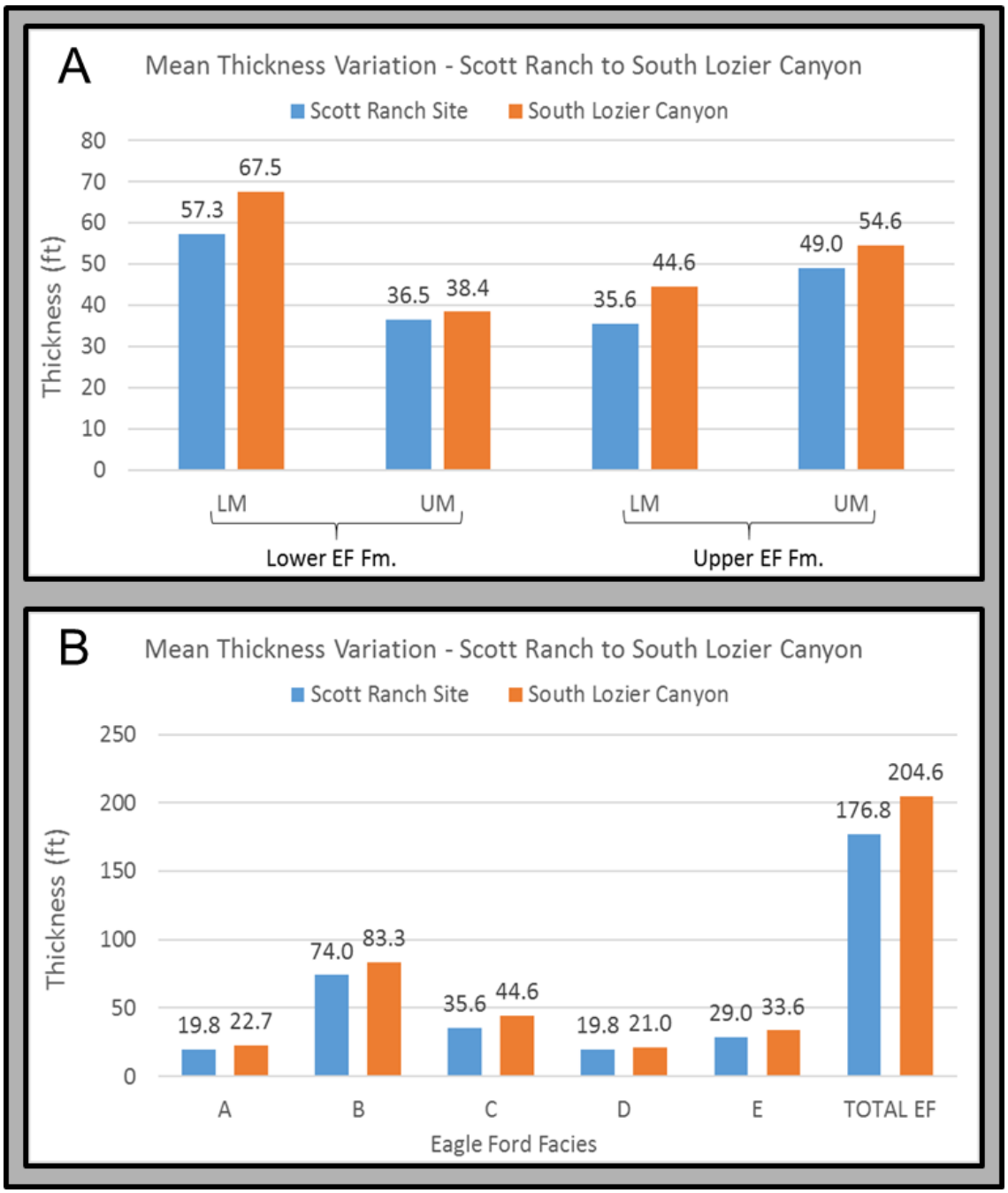

Figure 26. (A) Mean thickness variation of Eagle Ford group members at the Scott Ranch site compared to south Lozier Canyon. (B) Mean thickness variation of Eagle Ford group facies at the Scott Ranch site compared to south Lozier Canyon.

Table 3. Eagle Ford group thickness statistics at the Scott Ranch site in north Lozier Canyon.

Scott Ranch Site					
Unit	Mean Thickness	Min. Thickness	Max. Thickness	Std. dev.	Range
E	29.0 ft (8.84 m)	26.3 ft (8.02 m)	31.2 ft (9.52 m)	1.0 ft (0.3 m)	4.9 ft (1.5 m)
D	19.8 ft (6.02 m)	15.7 ft (4.8 m)	24.3 ft (7.4 m)	2.8 ft (0.84 m)	8.5 ft (2.6 m)
C	35.6 ft (10.86 m)	28.3 ft (8.64 m)	43.4 ft (13.22 m)	2.7 ft (0.81 m)	15.0 ft (4.58 m)
B	74.0 ft (22.56 m)	67.1 ft (20.45 m)	80.4 ft (24.5 m)	3.6 ft (1.09 m)	13.3 ft (4.05 m)
A	19.8 ft (6.03 m)	17.4 ft (5.3 m)	21.8 ft (6.64 m)	1.0 ft (0.32 m)	4.4 ft (1.34 m)
UEF, UM	49.0 ft (14.94 m)	40.6 ft (12.37 m)	54.4 ft (16.58 m)	2.85 ft (0.87 m)	13.8 ft (4.21 m)
UEF, LM	35.6 ft (10.86 m)	28.3 ft (8.64 m)	43.4 ft (13.22 m)	2.7 ft (0.81 m)	15.0 ft (4.58 m)
LEF, UM	36.5 ft (11.12 m)	28.9 ft (8.8 m)	42.7 ft (13.01 m)	3.1 ft (0.93 m)	13.8 ft (4.21 m)
LEF, LM	57.3 ft (17.48 m)	51.8 ft (15.78 m)	62.0 ft (18.9 m)	2.8 ft (0.85 m)	10.2 ft (3.12 m)
UEF Fm.	83.9 ft (25.57 m)	75.5 ft (23.01 m)	93.4 ft (28.47 m)	3.2 ft (0.98 m)	17.9 ft (5.46 m)
LEF Fm.	93.4 ft (28.47 m)	87.5 ft (26.67 m)	99.5 ft (30.33 m)	3.4 ft (1.04 m)	12.0 ft (3.66 m)
Eagle Ford Group	176.8 ft (53.88 m)	173.2 ft (52.79 m)	182.7 ft (55.68 m)	2.1 ft (0.63 m)	9.5 ft (2.89 m)

Table 4. Eagle Ford group thickness statistics in south Lozier Canyon. Resulting south Lozier Canyon statistics incorporate both Colonel Neck and Colonel Bend study sites.

South Lozier Canyon					
Unit	Mean Thickness	Min. Thickness	Max. Thickness	Std. dev.	Range
E	33.6 ft (10.24 m)	30.4 ft (9.27 m)	35.1 ft (10.71 m)	0.9 ft (0.26 m)	4.7 ft (1.44 m)
D	21.0 ft (6.4 m)	17.6 ft (5.35 m)	24.2 ft (7.39 m)	1.0 ft (0.31 m)	6.7 ft (2.04 m)
C	44.6 ft (13.59 m)	37.8 ft (11.52 m)	51.6 ft (15.72 m)	2.8 ft (0.86 m)	13.8 ft (4.2 m)
B	83.3 ft (25.39 m)	76.6 ft (23.36 m)	90.9 ft (27.72 m)	3.3 ft (1.0 m)	14.3 ft (4.36 m)
A	22.7 ft (6.91 m)	19.7 ft (6.01 m)	25.7 ft (7.84 m)	1.0 ft (0.32 m)	6.0 ft (1.83 m)
UEF, UM	54.6 ft (16.64 m)	51.2 ft (15.62 m)	56.5 ft (17.23 m)	0.9 ft (0.26 m)	5.3 ft (1.61 m)
UEF, LM	44.6 ft (13.59 m)	37.8 ft (11.52 m)	51.6 ft (15.72 m)	2.8 ft (0.86 m)	13.8 ft (4.2 m)
LEF, UM	38.4 ft (11.69 m)	33.7 ft (10.27 m)	42.8 ft (13.06 m)	2.0 ft (0.61 m)	9.2 ft (2.79 m)
LEF, LM	67.5 ft (20.58 m)	61.8 ft (18.85 m)	73.8 ft (22.48 m)	2.4 ft (0.74 m)	11.9 ft (3.63 m)
UEF Fm.	99.19 ft (30.23 m)	91.61 ft (27.92 m)	106.38 ft (32.42 m)	2.58 ft (0.79 m)	14.77 ft (4.50 m)
LEF Fm.	105.85 ft (32.26 m)	97.51 ft (29.72 m)	116.49 ft (35.51 m)	4.37 ft (1.33 m)	18.98 ft (5.79 m)
Eagle Ford Group	204.6 ft (62.36 m)	191.7 ft (58.44 m)	219.9 ft (67.03 m)	7.0 ft (2.13 m)	28.2 ft (8.59 m)

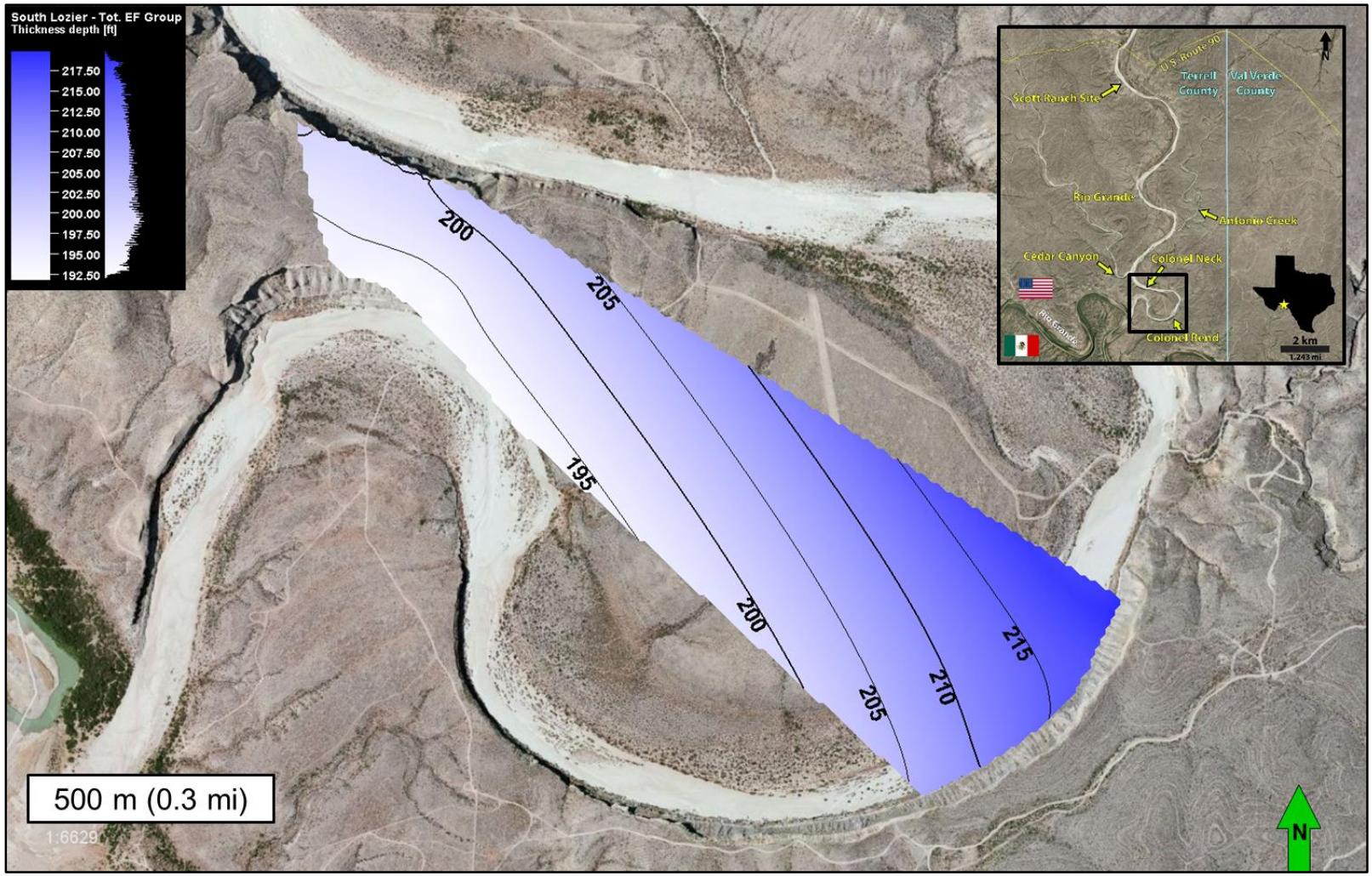

Figure 27. Isopach map of the Eagle Ford group (feet) at south Lozier Canyon produced from DOMs in Petrel 2014. Darker blue indicates thicker section.

Table 5. Stratigraphic thicknesses of Eagle Ford group members measured from DOMs. The percent difference in thickness is recorded in the furthest right column. The Lower member of the Upper Eagle Ford formation exhibits the largest percent difference in stratigraphic thickness from north-to-south Lozier Canyon.

Eagle Ford Group – Member Stratigraphic Thicknesses				
Formation	**Member**	**Scott Ranch site**	**South Lozier Canyon**	**Δ % Thickness**
Upper Eagle Ford	Upper	49.0 ft (14.94 m)	54.6 ft (16.64 m)	10.26 %
	Lower	35.6 ft (10.85 m)	44.6 ft (13.59 m)	20.18 %
Lower Eagle Ford	Upper	36.5 ft (11.13 m)	38.4 ft (11.70 m)	4.95 %
	Lower	57.3 ft (17.47 m)	67.5 ft (20.57 m)	15.11 %

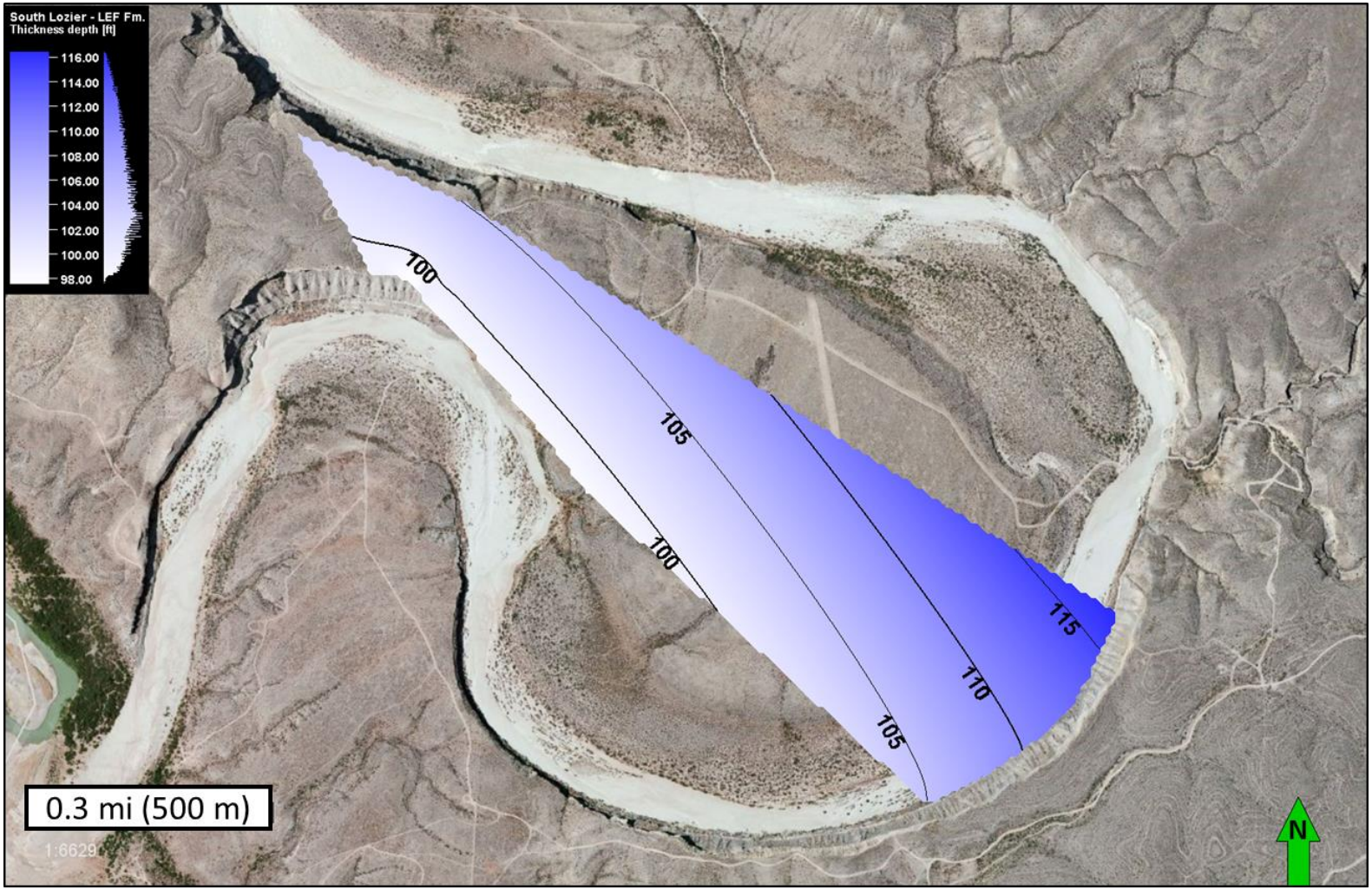

Figure 28. Isopach map of the Lower Eagle Ford formation (feet) at south Lozier Canyon from DOMs generated in Petrel 2014.

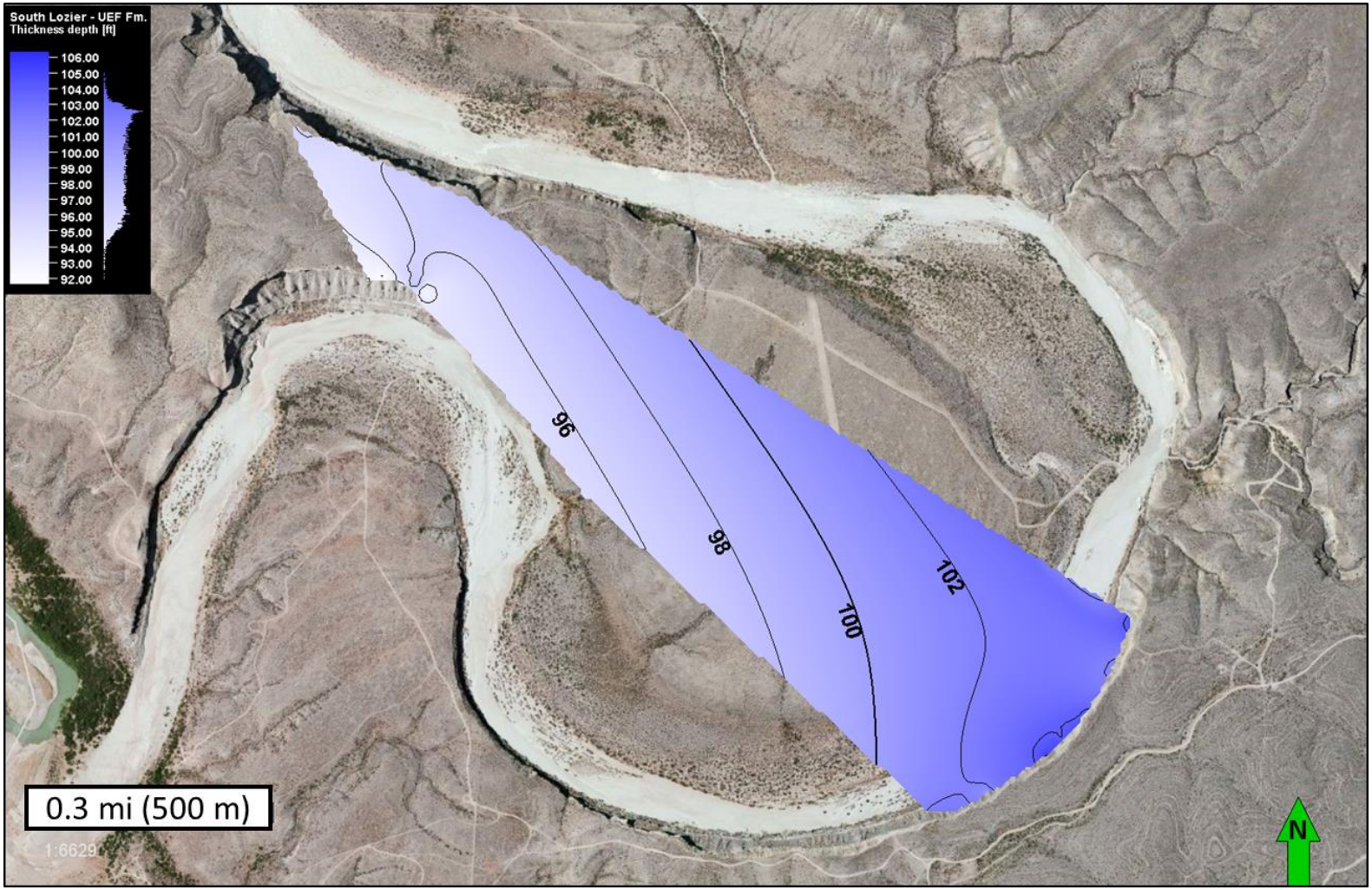

Figure 29. Isopach map of the Upper Eagle Ford formation (feet) at south Lozier Canyon from DOMs generated in Petrel 2014.

4.1.3 Eagle Ford Members

The Lower member of the Lower Eagle Ford formation has an average thickness of 57.3 ft (17.48 m) at the Scott Ranch site (Figure 26A; Table 3). In south Lozier Canyon, it has an average thickness of 67.5 ft (20.58 m) indicating a 10.2 ft (3.11 m) and 15.11% increase in average thickness from north-to-south Lozier Canyon (Table 4; Table 5). Isopach maps from DOM measurements of south Lozier Canyon show thickness gradually increasing northeastward (Figure 30).

The Upper member of the Lower Eagle Ford formation has an average thickness of 36.5 ft (11.12 m) at the Scott Ranch site (Figure 26A; Table 3). In south Lozier Canyon, it has an average thickness of 38.4 ft (11.69 m) indicating a 1.9 ft (0.58 m) and 4.95% increase in average thickness from north-to-south Lozier Canyon (Table 4; Table 5). This minor change in average thickness is well within measurement error and suggests that this member does not really vary in thickness between north and south Lozier Canyon. Isopach maps based on DOM measurements of south Lozier Canyon show thickness gradually increasing northeastward (Figure 31).

The Lower member of the Upper Eagle Ford formation has an average thickness of 35.6 ft (10.86 m) at the Scott Ranch site (Figure 26A; Table 3). In south Lozier Canyon, it has an average thickness of 44.6 ft (13.59 m) indicating a 9 ft (2.74 m) and 20.18% increase in average thickness from north-to-south Lozier Canyon (Table 4; Table 5). This member displays the greatest range in thickness of any other member at

the Scott Ranch site, 15.0 ft (4.58 m), and south Lozier Canyon, 13.8 ft (4.2 m). Thickness increases to the southeast within south Lozier Canyon (Figure 32).

The Upper member of the Upper Eagle Ford formation has an average thickness of 49.0 ft (14.94 m) at the Scott Ranch site (Figure 26A; Table 3). In south Lozier Canyon, it has an average thickness of 54.6 ft (16.64 m) indicating a 5.6 ft (1.71 m) and 10.26% increase in average thickness from north-to-south Lozier Canyon (Table 4; Table 5). Thickness varies minimally within south Lozier Canyon based on DOM isopach maps (Figure 33).

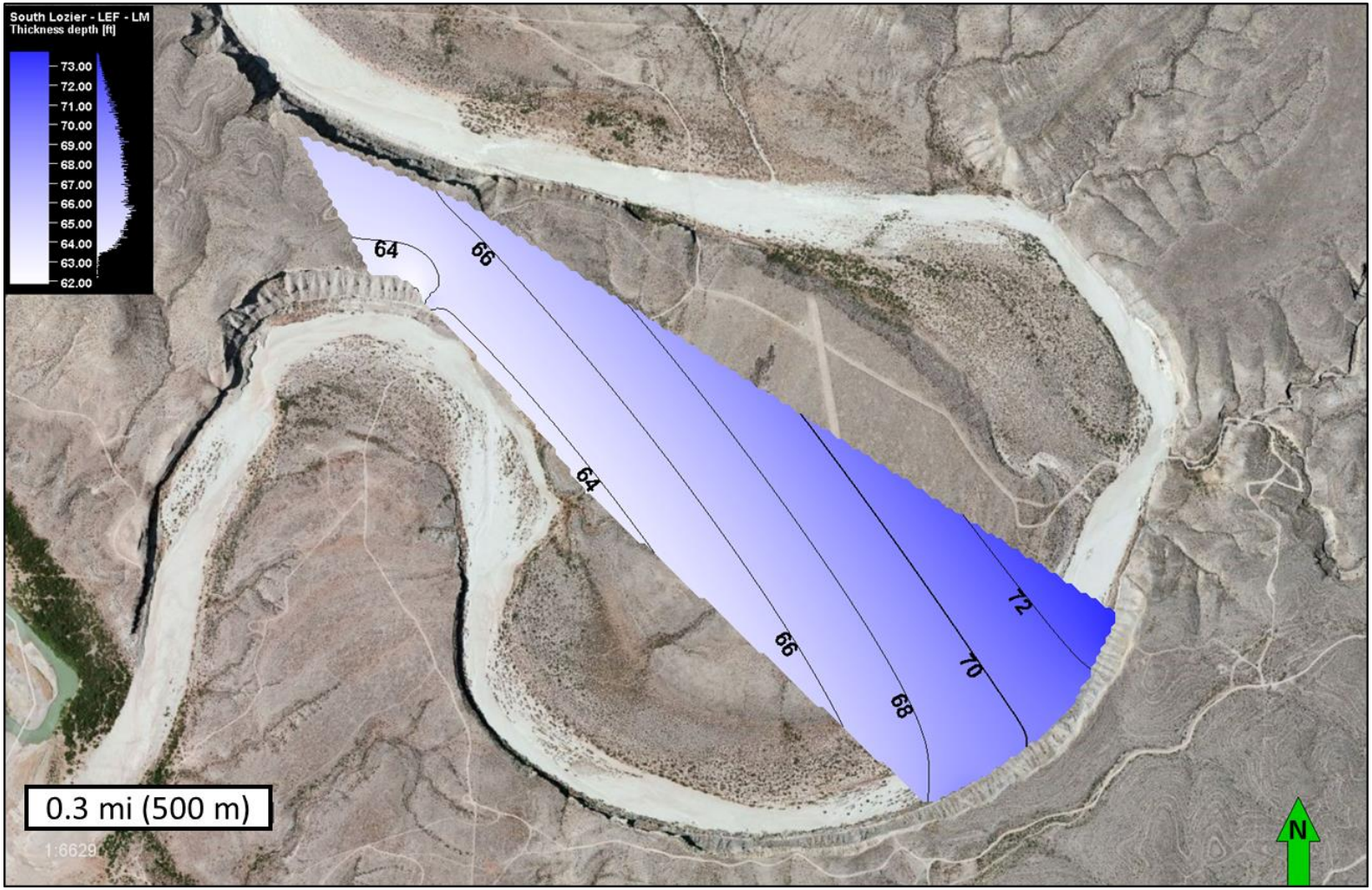

Figure 30. Isopach map of the Lower member of the Lower Eagle Ford formation (feet) at south Lozier Canyon from DOMs generated in Petrel 2014.

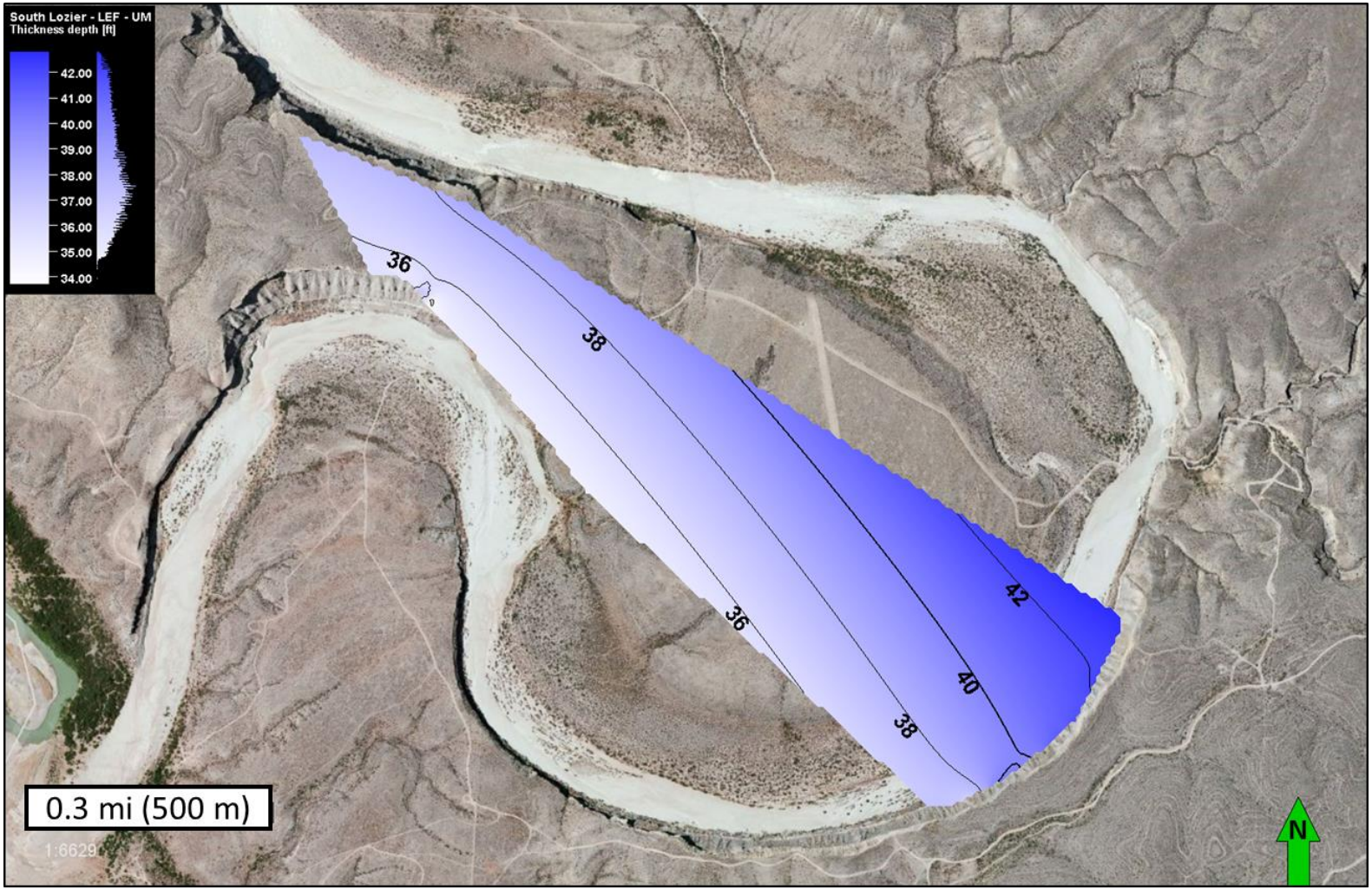

Figure 31. Isopach map of the Upper member of the Lower Eagle Ford formation (feet) at south Lozier Canyon from DOMs generated in Petrel 2014.

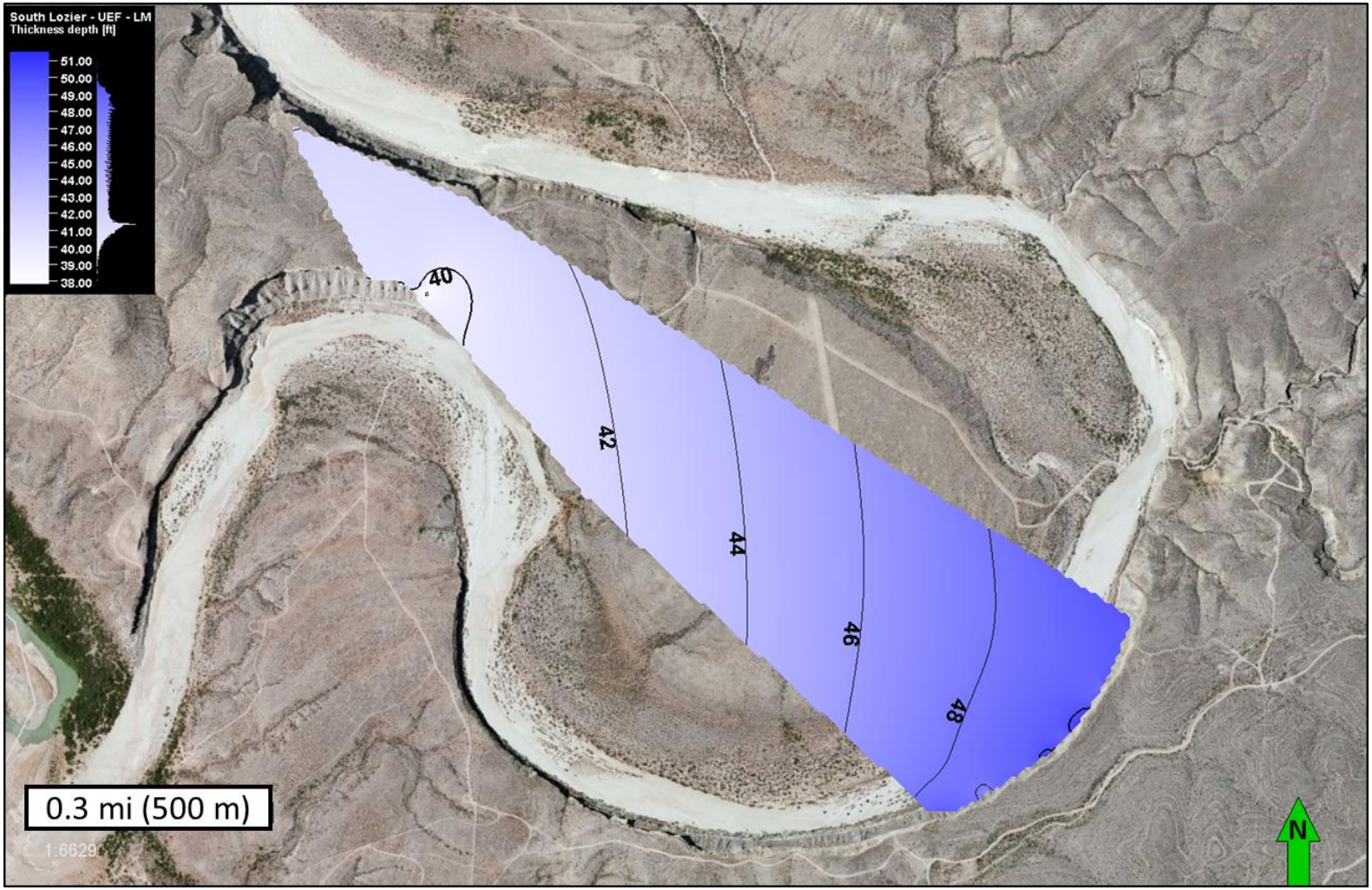

Figure 32. Isopach map of the Lower member of the Upper Eagle Ford formation (feet) at south Lozier Canyon from DOMs generated in Petrel 2014.

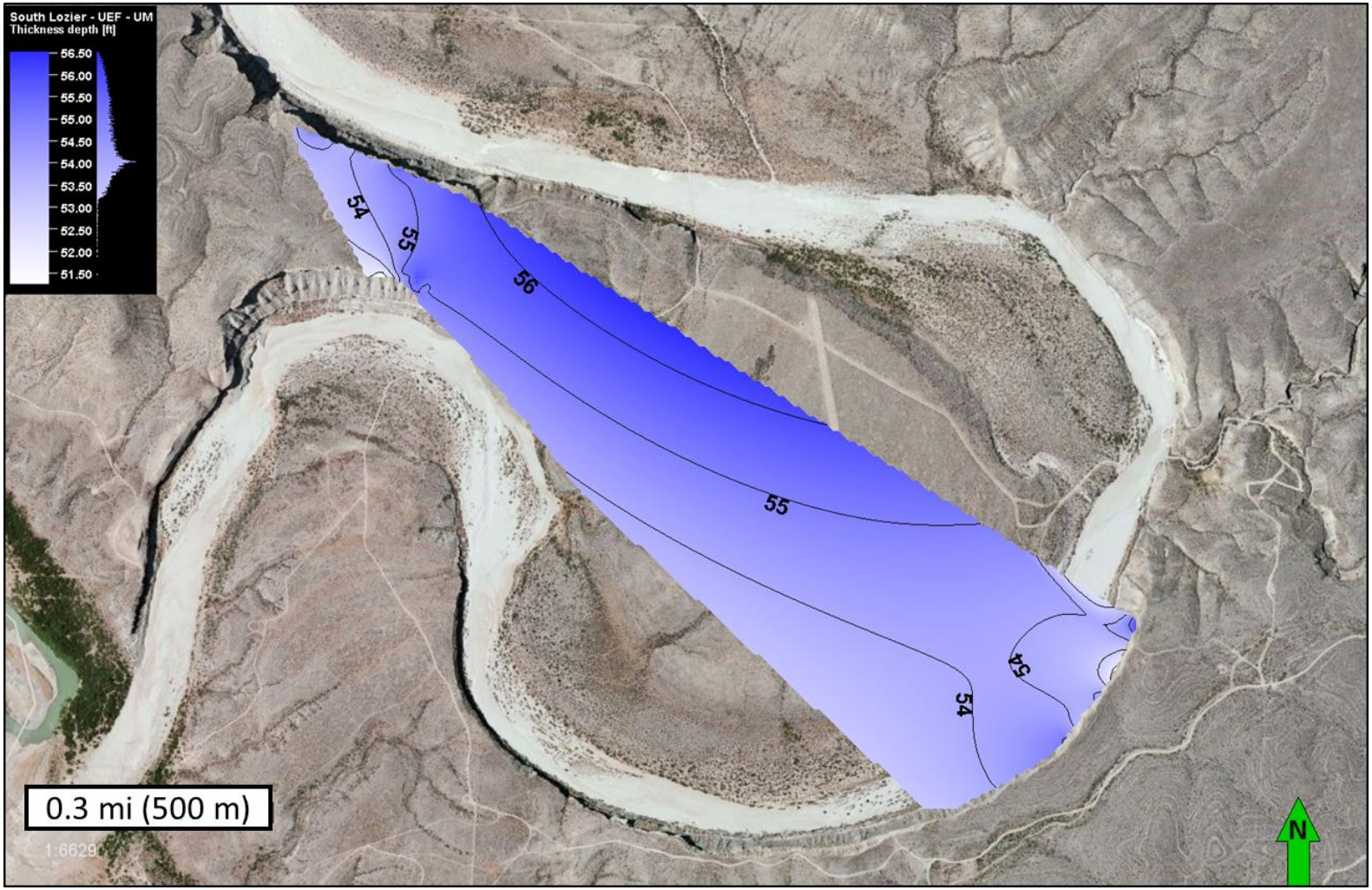

Figure 33. Isopach map of the Upper member of the Upper Eagle Ford formation (feet) at south Lozier Canyon from DOMs generated in Petrel 2014.

4.1.4 Eagle Ford Facies

Facies A of the Eagle Ford group has an average thickness of 19.8 ft (6.03 m) at the Scott Ranch site (Figure 26B; Table 3). In south Lozier Canyon, it has an average thickness of 22.7 ft (6.91 m) indicating a 2.9 ft (0.88 m) and 12.78% increase in average thickness from north-to-south Lozier Canyon (Table 4; Table 6). In Antonio Creek, Facies A is about 22.0 ft (6.7 m) thick (Gardner et al., 2013). Thickness increases minimally to the northeast within south Lozier Canyon (Figure 34).

Facies B of the Eagle Ford group has an average thickness of 74.0 ft (22.56 m) at the Scott Ranch site (Figure 26B; Table 3). In south Lozier Canyon, it has an average thickness of 83.3 ft (25.39 m) indicating a 9.3 ft (2.83 m) and 11.16% increase in average thickness from north-to-south Lozier Canyon (Table 4; Table 6). Facies B is the thickest facies of the Eagle Ford group and it shows the greatest standard deviation at both the Scott Ranch site, 3.6 ft (1.09 m), and south Lozier Canyon, 3.3 ft (1.0 m). In Antonio Creek, Facies B is about 74.0 ft (22.6 m) thick (Gardner et al., 2013). Thickness gradually increases to the northeast within south Lozier Canyon (Figure 35).

Facies C of the Eagle Ford group has an average thickness of 35.6 ft (10.85 m) at the Scott Ranch site (Figure 26B; Table 3). In south Lozier Canyon, it has average thickness of 44.6 ft (13.59 m) indicating a 9 ft (2.74 m) and 20.18% increase in average thickness from north-to-south Lozier Canyon (Table 4; Table 6). In Antonio Creek, Facies C is about 40.5 ft (12.3 m) thick (Gardner et al., 2013). Thickness gradually thickens to the east-southeast within south Lozier Canyon (Figure 36).

Facies D of the Eagle Ford group has an average thickness of 19.8 ft (6.02 m) at the Scott Ranch site (Figure 26B; Table 3). In south Lozier Canyon, it has an average thickness of 21.0 ft (6.4 m) indicating a 1.2 ft (0.37 m) and 5.71% increase in average thickness from north-to-south Lozier Canyon (Table 4; Table 6). In Antonio Creek, Facies D is about 20.0 ft (6.0 m) thick (Gardner et al., 2013). Thickness varies minimally within south Lozier Canyon (Figure 37).

Facies E of the Eagle Ford group has an average thickness of 29.0 ft (8.84 m) at the Scott Ranch site (Figure 26B; Table 3). In south Lozier Canyon, it has an average thickness of 33.6 ft (10.24 m) indicating a 4.6 ft (1.40 m) and 13.69% increase in average thickness from north-to-south Lozier Canyon (Table 4; Table 6). In Antonio Creek, Facies E is about 26.0 ft (7.9 m) thick (Gardner et al., 2013). Thickness varies minimally within south Lozier Canyon (Figure 38).

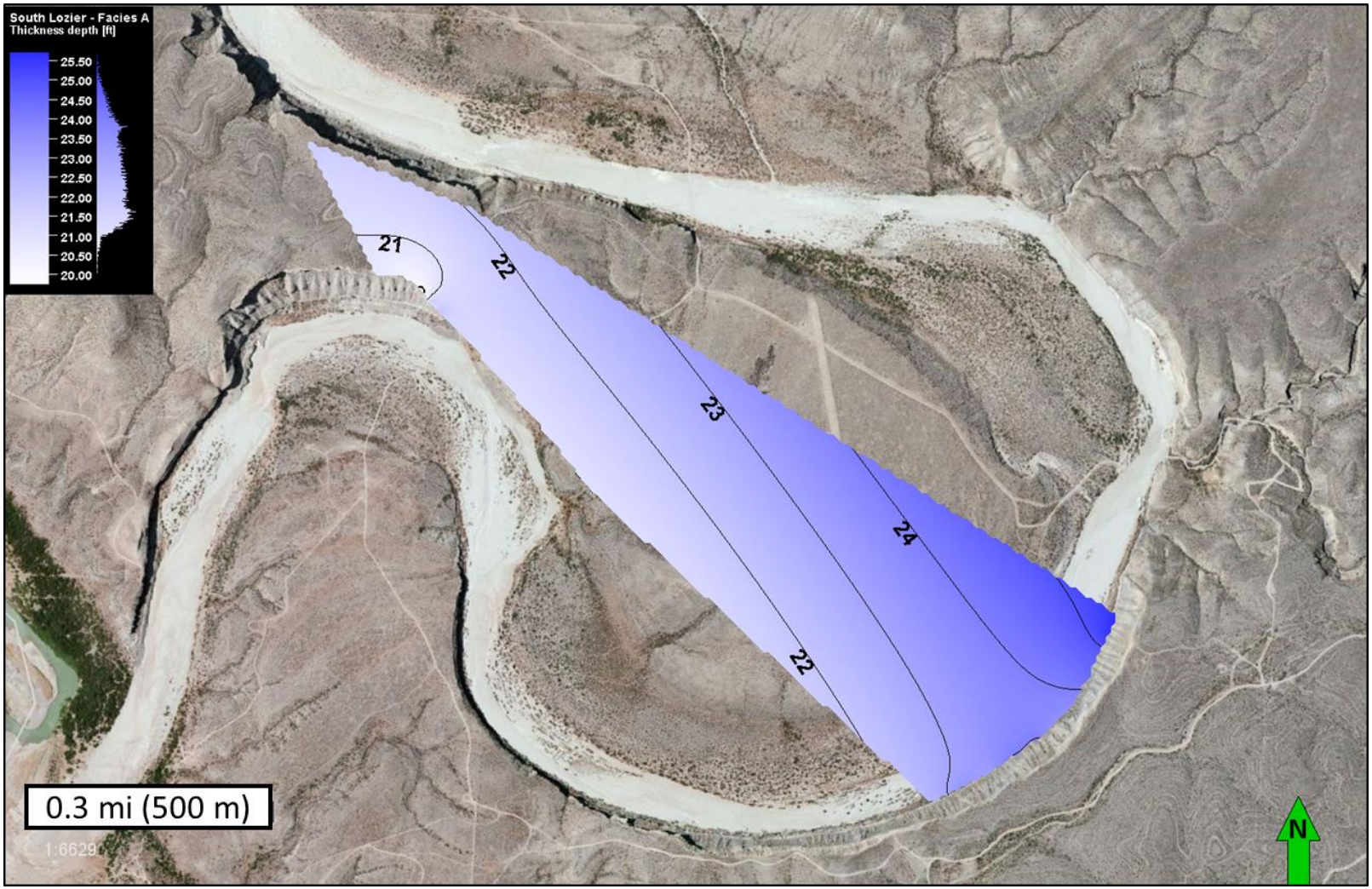

Figure 34. Isopach map of Eagle Ford group Facies A (feet) at south Lozier Canyon from DOMs generated in Petrel 2014.

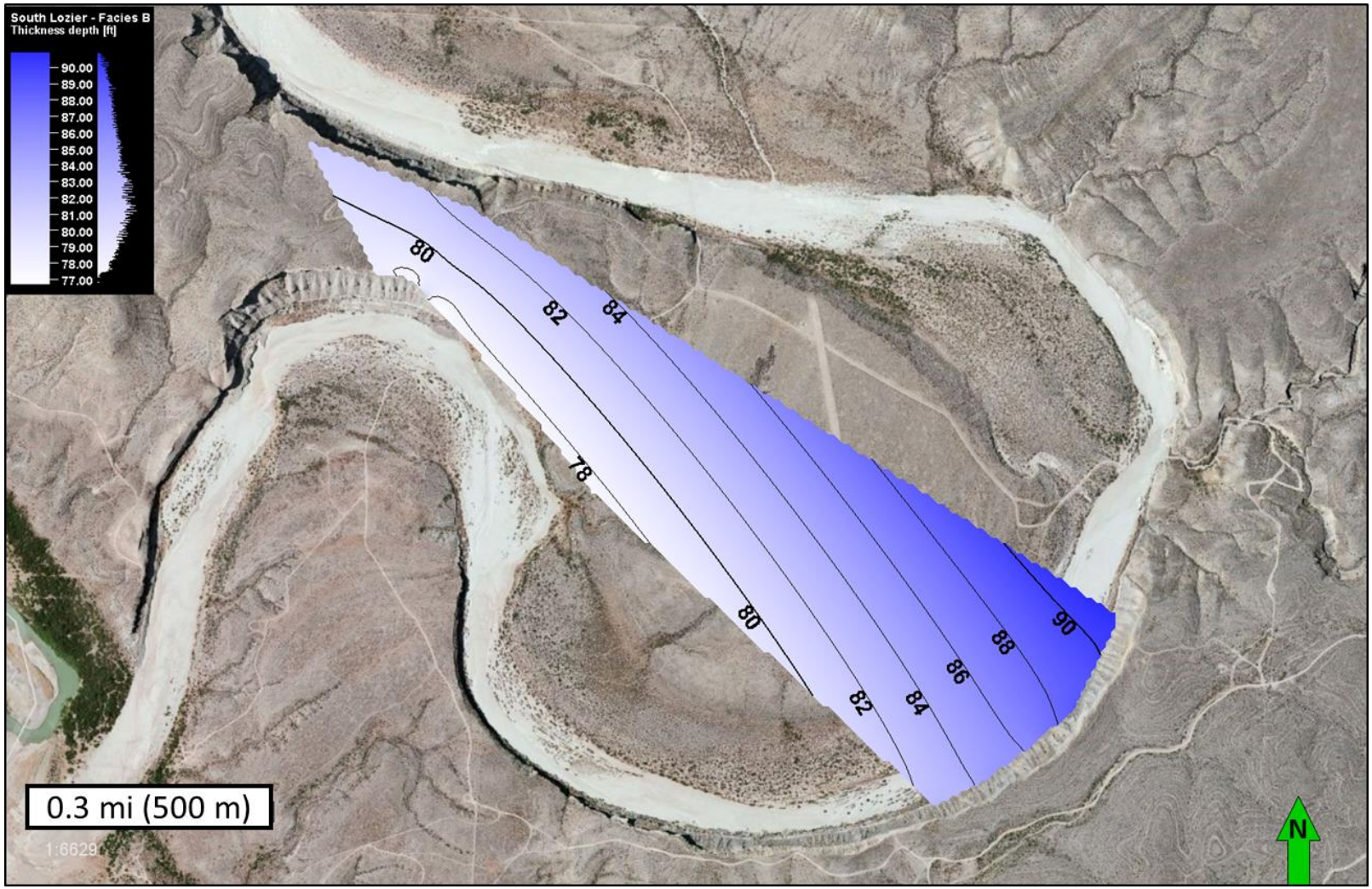

Figure 35. Isopach map of Eagle Ford group Facies B (feet) at south Lozier Canyon from DOMs generated in Petrel 2014.

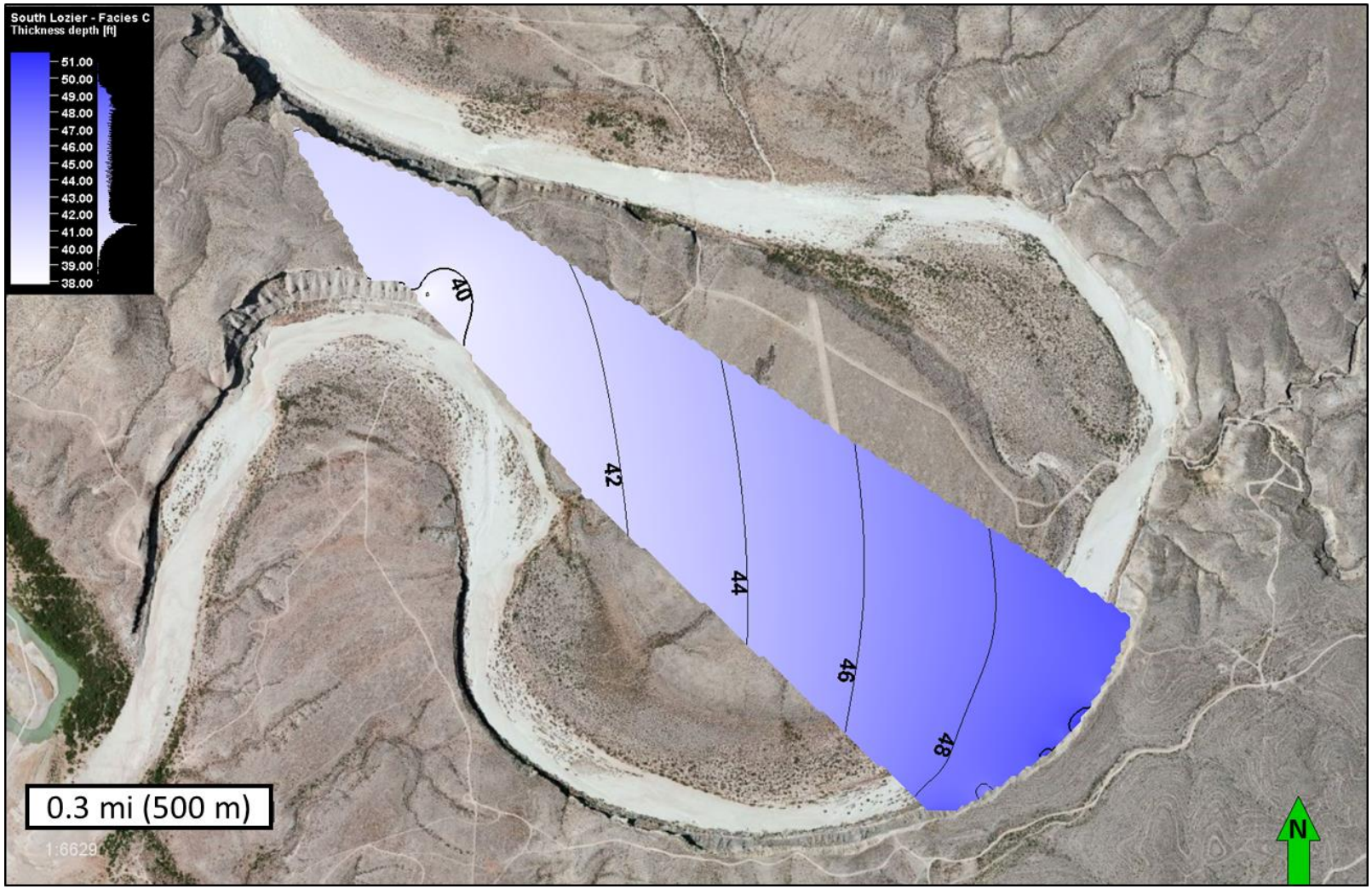

Figure 36. Isopach map of Eagle Ford group Facies C (feet) at south Lozier Canyon from DOMs generated in Petrel 2014.

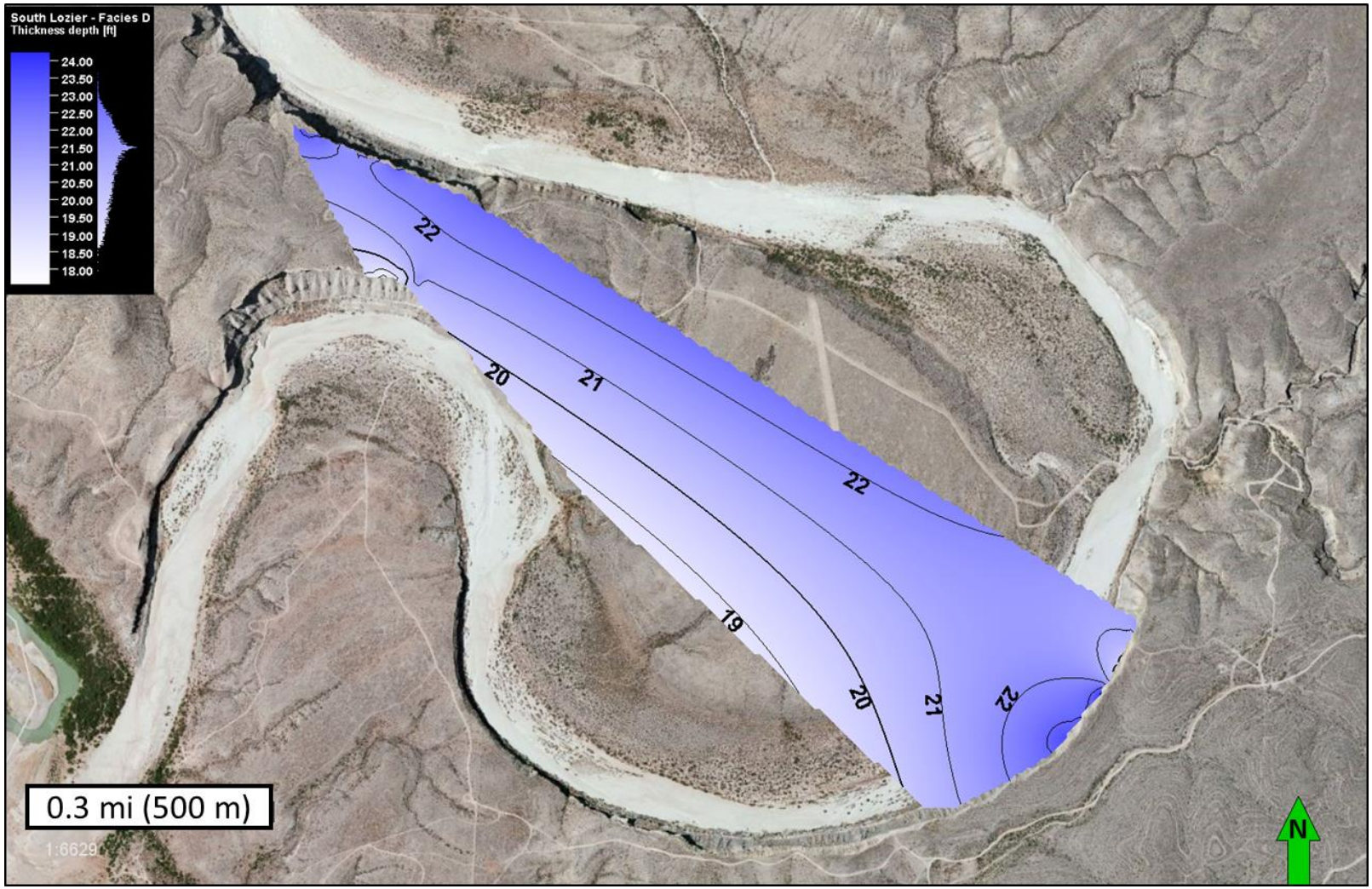

Figure 37. Isopach map of Eagle Ford group Facies D (feet) at south Lozier Canyon from DOMs generated in Petrel 2014.

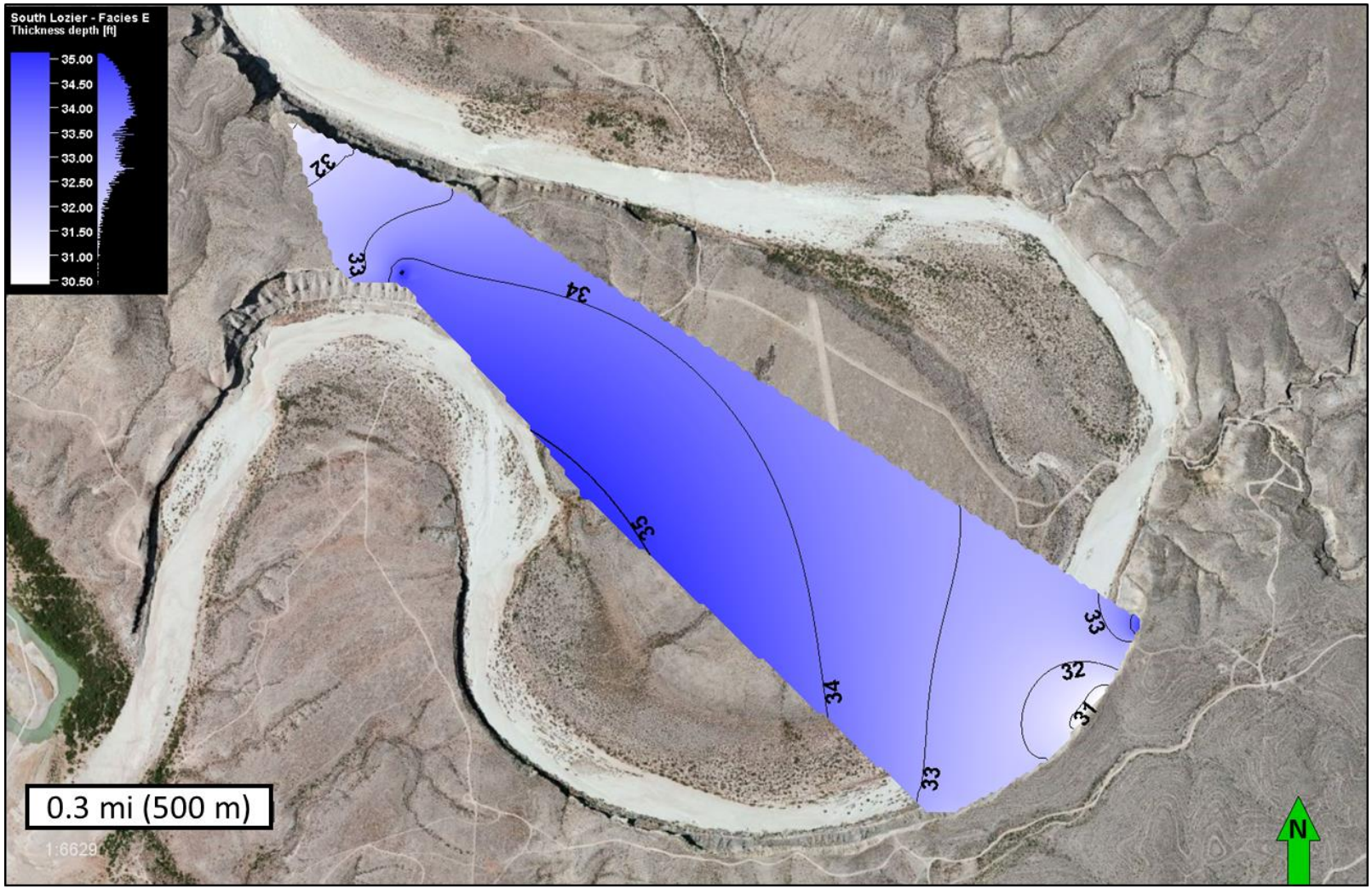

Figure 38. Isopach map of Eagle Ford group Facies E (feet) at south Lozier Canyon from DOMs generated in Petrel 2014.

Table 6. Stratigraphic thicknesses of each Eagle Ford group facies measured from DOMs. The percent difference in thickness is recorded in the furthest right column. Facies C exhibits the largest percent difference in stratigraphic thickness from north-to-south Lozier Canyon.

Eagle Ford Group – Facies Stratigraphic Thicknesses			
Facies	**Scott Ranch site**	**South Lozier Canyon**	**Δ % Thickness**
E	29.0 ft (8.84 m)	33.6 ft (10.24 m)	13.69 %
D	19.8 ft (6.04 m)	21.0 ft (6.4 m)	5.71 %
C	35.6 ft (10.85 m)	44.6 ft (13.59 m)	20.18 %
B	74.0 ft (22.56 m)	83.3 ft (25.39 m)	11.16 %
A	19.8 ft (6.04 m)	22.7 ft (6.92 m)	12.78 %

4.2 High-Resolution Stratigraphic Analysis of Facies B

Interbedded foraminiferal skeletal packstone – grainstone (PS – GS) beds and lenses observable in 2-D outcrop orthomosaics were analyzed in Eagle Ford group Facies B at three locations: Scott Ranch site, Colonel Neck site, and Colonel Bend site.

Combining the three study sites, median apparent lens length of all skeletal PS – GS lenses in Facies B of the Eagle Ford group is ~ 2.8 ft (0.85 m) (Figure 39; Table 7). An analysis of sub-facies apparent lens lengths (B1, B2, B3, B4, and B5) was accomplished at the Scott Ranch study site where all sub-facies contacts were precisely defined by previous studies (Donovan et al., 2012; Donovan et al., 2016; Gardner et al., 2013). Skeletal PS – GS lenses in Facies B tend to have longer apparent lens lengths towards the bottom of the unit (Sub-facies B1 and B2), and shorter apparent lens lengths towards the top (Sub-facies B4 and B5). Median skeletal PS – GS apparent lens length in Sub-facies B2 is 5.0 ft (1.5 m) with a maximum recorded length of 153.5 ft (46.8 m)

(Figure 40; Table 8). Skeletal PS – GS lenses in B2 are the greatest in average length compared to the other sub-facies. Skeletal PS – GS lenses in Sub-facies B4 and B5 are the shortest in median apparent lens length at 2.2 ft (0.7 m) respectively (Figure 40; Table 8). Just below the Facies B – C contact (uppermost B5), skeletal PS – GS beds are nonexistent and the strata is entirely mudstone.

Throughout Facies B, skeletal PS – GS lenses swell and pinch-out along parallel bedding planes, thus they are not positioned randomly in outcrop. Unlike Facies B, skeletal WS – PS beds in Facies C are much more continuous at all study sites and generally have bed thicknesses greater than skeletal PS – GS lenses in mid-to-upper Facies B. Skeletal PS – GS lenses in Facies B are typically only a few inches thick with the thickest lenses reaching 6 in (2.54 – 15.24 cm) in thickness (Donovan et al., 2012; Gardner et al., 2013). Skeletal WS – PS beds in Facies C vary from 2 in (5.08 cm) to 12 in (m) in thickness (Gardner et al., 2013).

In summation, skeletal PS – GS beds and lenses within Facies B become less prevalent and shorter in length in the upper part of the section from Sub-facies B2 through B5 (Figure 40 & Figure 41). Most prominent skeletal WS – PS beds in Facies C are much more laterally continuous than skeletal PS – GS beds in Facies B, and most may be correlated in outcrop photos from north-to-south Lozier Canyon (Figure 42).

Table 7. Statistics for Eagle Ford group Facies B skeletal packstone – grainstone lateral apparent lens lengths measured from 2-D orthomosaics. Values are reported in feet (mean/median).

Total Facies B - Packstone-Grainstone Apparent Lens Length Statistics				
Study Site	**Scott Ranch**	**Colonel Neck**	**Colonel Bend (East)**	**Colonel Bend (West)**
Count	1,363	3,462	1,599	1,049
Apparent Lens Length (ft)	4.7/2.7	4.0/2.5	5.0/2.7	6.0/3.1
Range (ft)	209.0	95.9	74.8	127.8
Minimum (ft)	0.5	0.1	0.1	0.4
Maximum (ft)	209.5	96.1	74.9	128.2

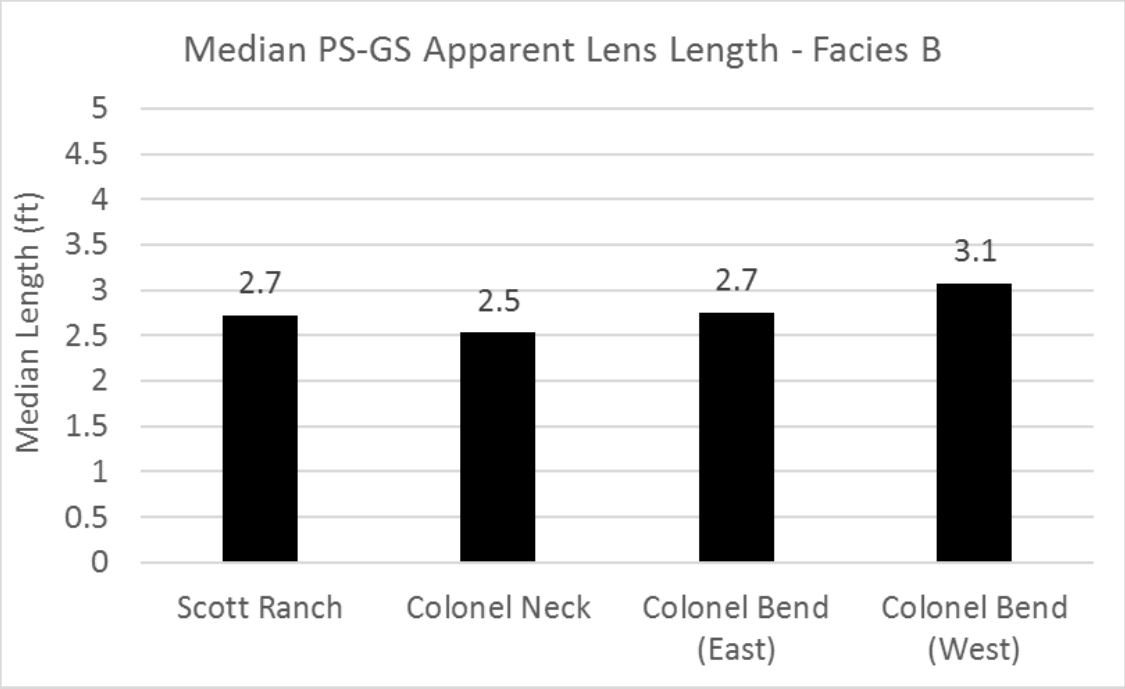

Figure 39. Median Packstone – Grainstone lateral apparent lens lengths in Eagle Ford group Facies B at the Scott Ranch, Colonel Neck, and Colonel Bend study sites. Two different locations were analyzed at the Colonel Bend site and they are designated directionally (East & West).

Table 8. Statistics for Eagle Ford group Sub-facies B1, B2, B3, B4, and B5 skeletal packstone – grainstone lateral apparent lens lengths at the Scott Ranch site in northern Lozier Canyon measured from 2-D orthomosaics. Values are reported in feet (mean/median).

Scott Ranch (North) - Sub-facies of Facies B - Packstone-Grainstone Apparent Lens Length Statistics					
Sub-facies:	**B1**	**B2**	**B3**	**B4**	**B5**
Count	113	145	176	79	37
Apparent Lens Length (ft)	5.0/2.4	10.5/5.0	3.9/2.9	2.6/2.2	3.2/2.2
Range (ft)	47.3	152.8	22.1	9.5	11.1
Minimum (ft)	0.5	0.7	0.7	0.9	0.6
Maximum (ft)	47.8	153.5	22.8	10.3	11.7

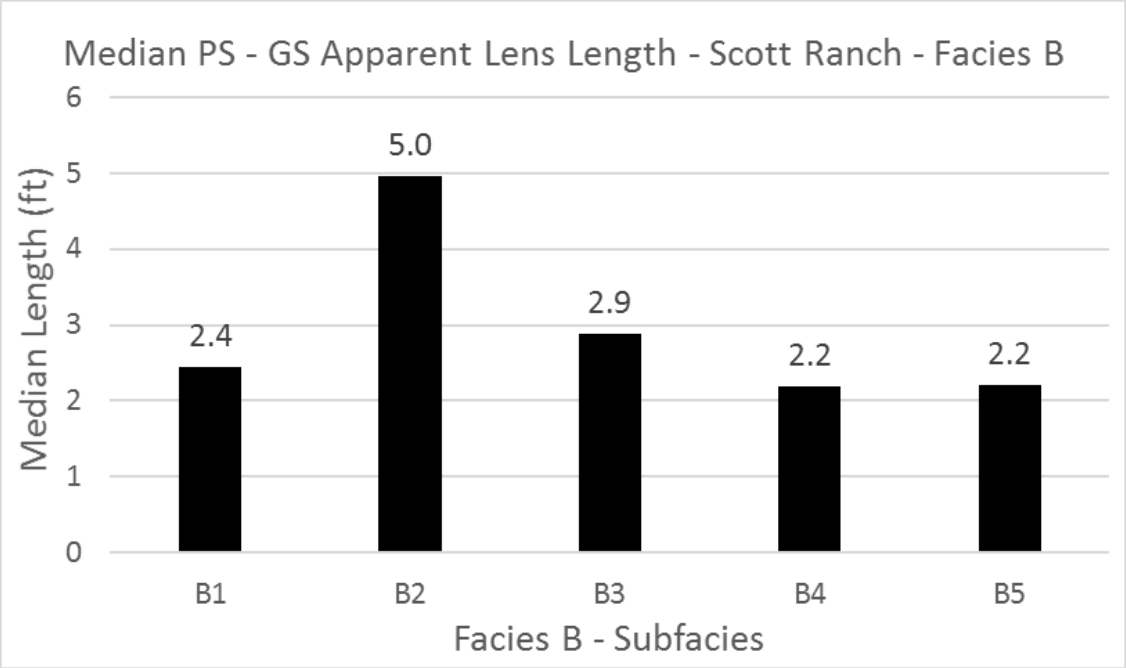

Figure 40. Median Packstone – Grainstone apparent lens lengths of Facies B – Sub-facies B1, B2, B3, B4, and B5 at the Scott Ranch study site in northern Lozier Canyon.

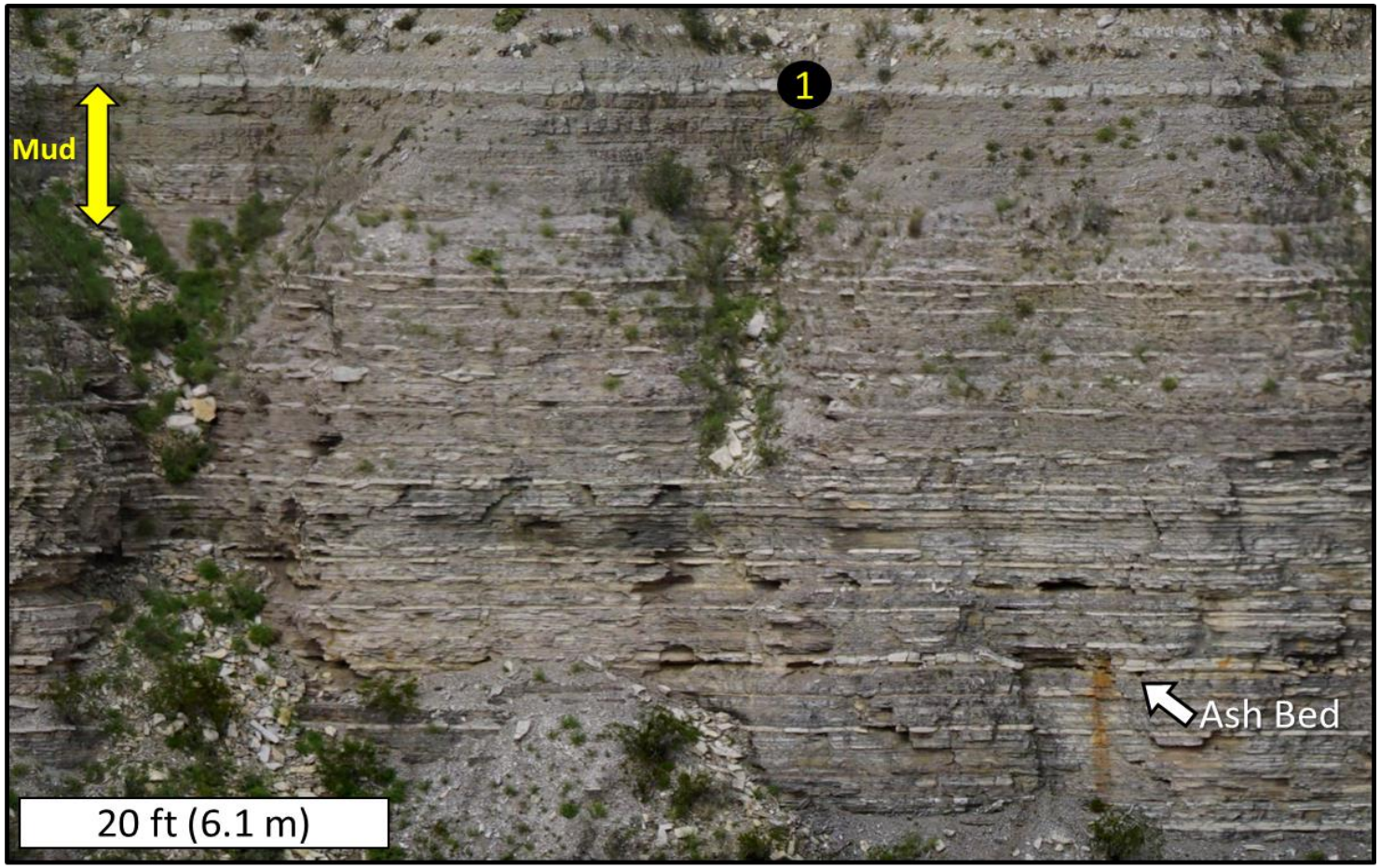

Figure 41. 2-D orthomosaic close-up of the Upper member of the Lower Eagle Ford formation Sub-facies (B3, B4, & B5) at the Scott Ranch site. Black circle with #1 indicates Facies B – C contact. White skeletal packstone-grainstone (PS – GS) lenses are more continuous and prevalent toward the bottom of the photo and are gradually less frequent up-section toward the Facies B – C contact. There are very little, if any, skeletal PS – GS beds just beneath the Facies B – C contact and it is dominantly calcareous mudstone shown by yellow arrow.

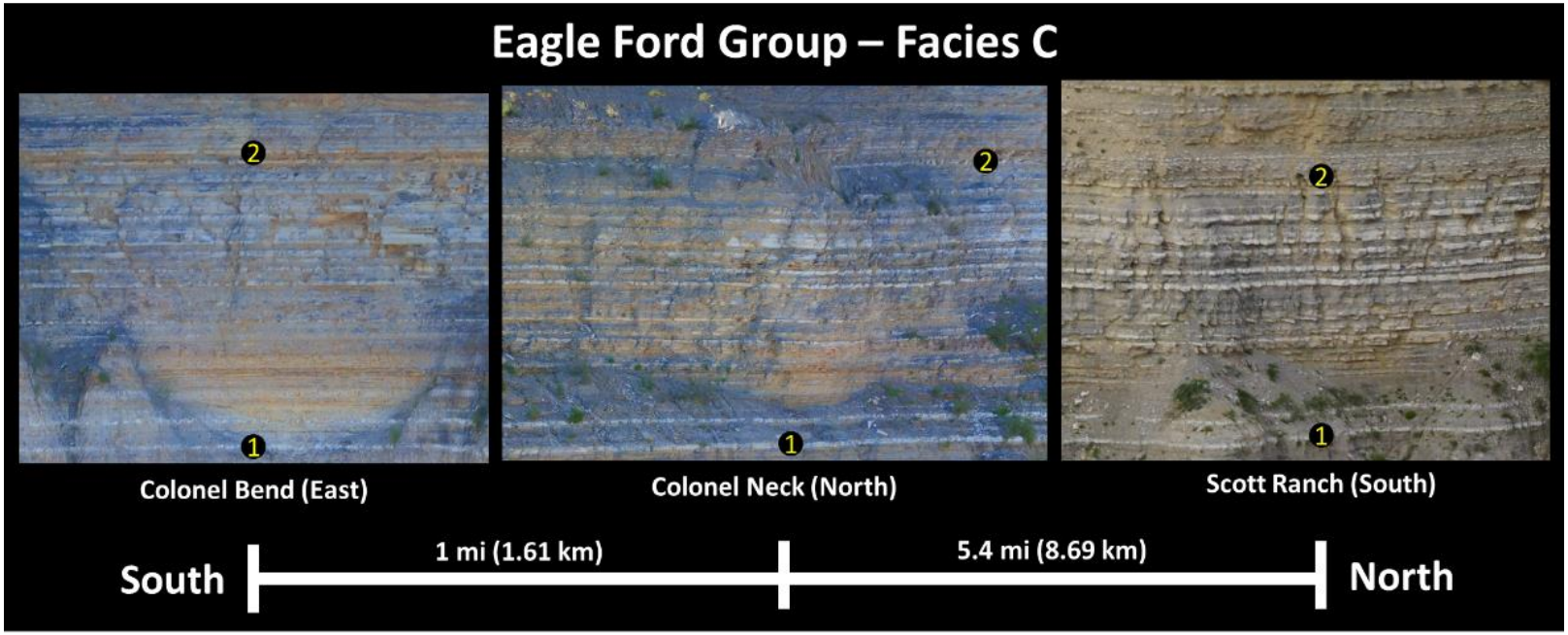

Figure 42. 2-D orthomosaic close-up of Eagle Ford group Facies C at three different study locations; Colonel Bend (East), Colonel Neck (North), and Scott Ranch (South). Black circles with #1 indicate Facies B – C contact. Black circles with #2 indicate Facies C – D contact. These three orthomosaics have been aligned based on the Facies B – C contact (#1). Skeletal wackestone-packstone beds (white colored beds) are continuous and the majority are correlative from north-to-south Lozier Canyon (a straight-line distance of 6.2 mi (10.0 km)).

4.3 Outcrop Brightness Logs – A Sub-Meter Scale Analysis

Outcrop brightness logs (BLs) produced from 2-D orthomosaics of the three primary study sites (Scott Ranch, Colonel Neck, and Colonel Bend) were constructed and analyzed with the objective of measure thickness at finer resolution sub-meter to cm scale. Facies contacts were interpreted using 2-D orthomosaics and BL characteristics. Polynomial trend lines were used to classify portions of the BL curve as either predominantly grain-dominated texture or mud-dominated texture (Figure 43).

While analyzing the BLs from each study site and organizing data by facies, inconsistencies among the data were evident. Calculated abundance of grain-dominated and mud-dominated rock of each facies from the three study sites reveal data ranges of greater than or equal to 22.86% (Table 9). Facies D yields the greatest data range at 57.51% (Table 9). Furthermore, discrepancies between the shape of the three BLs and the Scott Ranch BP GR logs were evident (Figure 44) once BLs were compressed to align with the measured GR logs of the Scott Ranch site (Donovan et al., 2015; Gardner et al., 2013).

Of the three BLs, the Colonel Bend BL most closely resembles the BP total gamma-ray curve (Figure 44). Using the polynomial trend line methodology, the Colonel Bend BL shows that Facies D had the highest abundance of mud-dominated texture (86.82% mud-dominated) followed by Facies B (71.10% mud-dominated) (Table 10). Facies C had the lowest abundance of mud-dominated texture and the highest abundance of grain-dominated texture (72.82% grain-dominated; 27.18% mud-dominated) (Table

10). These results are comparable with field observations where Facies D and Facies B are described as darker-colored rock with higher radioactivity and Facies C is described as lighter-colored/less radioactive mudstones with many thick and continuous white skeletal WS – PS beds.

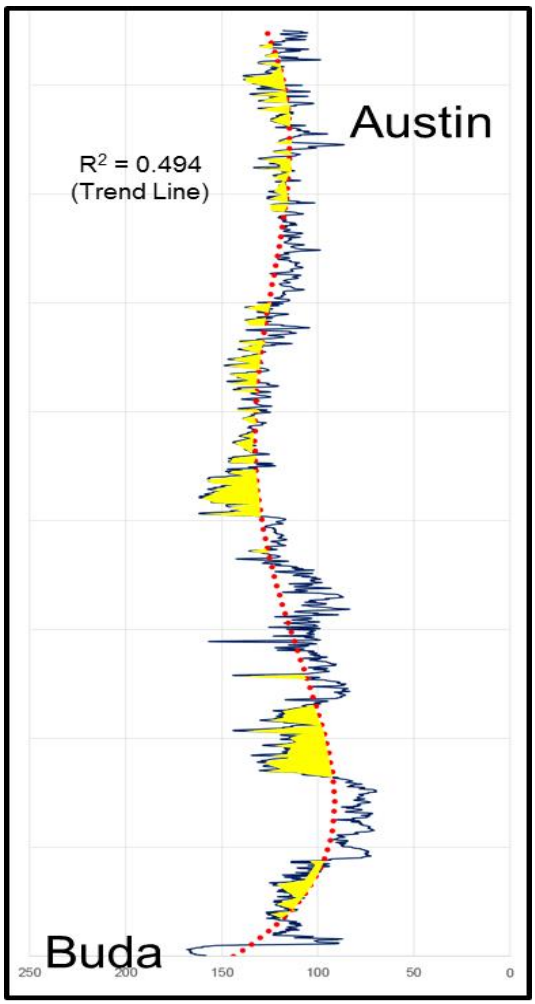

Figure 43. Outcrop brightness log (BL) of the Eagle Ford group at the Colonel Bend study site. The BL curve is navy blue and the 5th order polynomial trend line is the dashed red line. Yellow highlighted portions of the curve indicate portions of the BL that express greater (brighter) values than the trend line and would be classified as grain-dominated rather than mud-dominated. The Buda and Austin contacts are annotated and an R-squared coefficient of determination is provided for the polynomial trend line.

Table 9. Abundance of grain-dominated vs. mud-dominated texture for the Eagle Ford group BLs differentiated by facies. Average percentages of grain-dominated and mud-dominated rock are derived from the mean of all three study locations. The "Range" column is shown in bold to draw attention to the extreme range in data for each facies, particularly Facies D (57.51%).

Facies	Avg. % Grain-Dominated Texture	Avg. % Mud-Dominated Texture	Range
E	47.5%	52.5%	**45.4%**
D	42.2%	57.8%	**57.5%**
C	57.8%	42.2%	**22.9%**
B	53.1%	46.9%	**40.9%**
A	37.5%	62.5%	**44.0%**

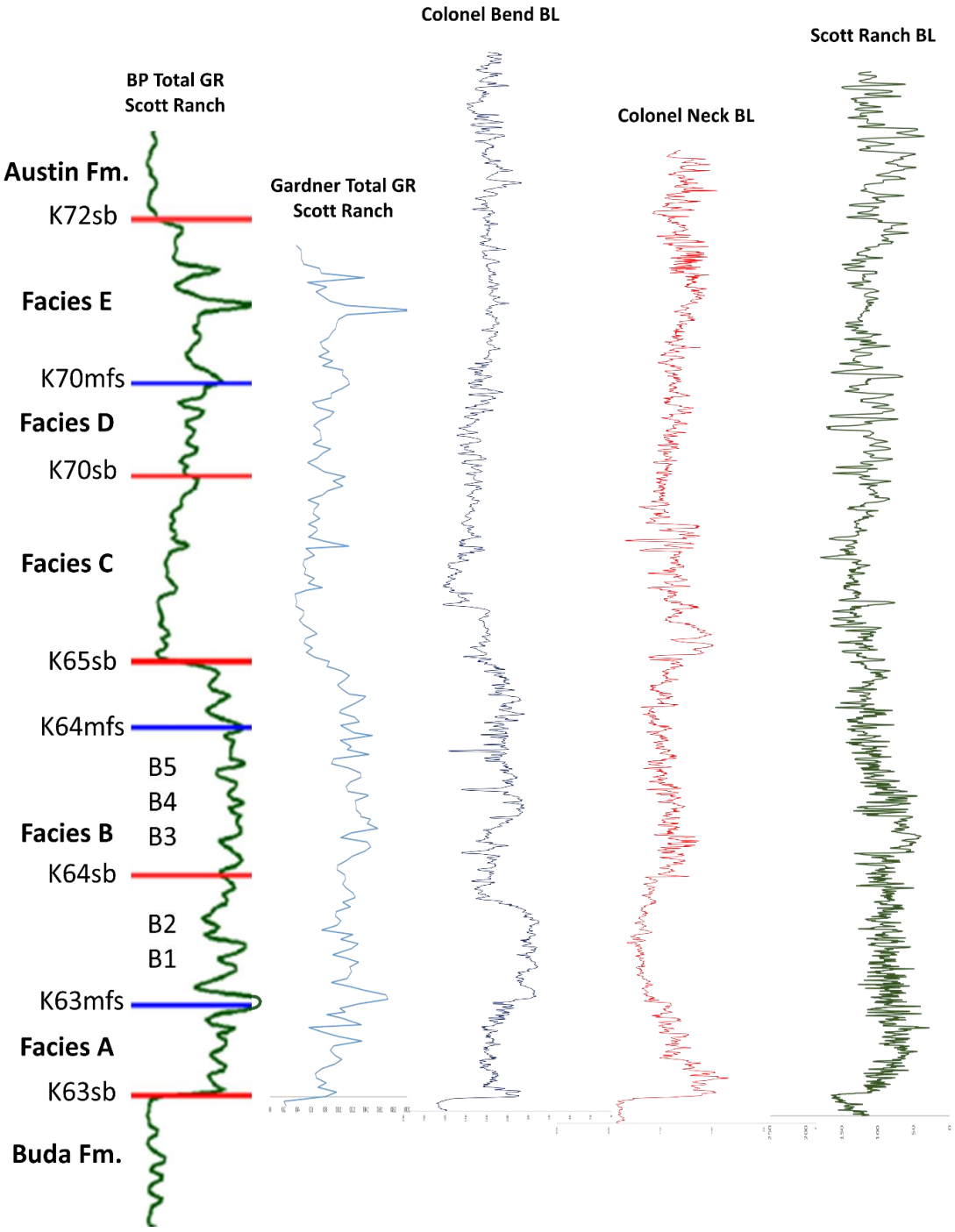

Figure 44. Annotated correlation of Scott Ranch Total Gamma-ray (GR) curves and the three BLs acquired in this study. The Scott Ranch BP Total GR log is on the far left (Donovan et al., 2015). The Scott Ranch handheld spectrometer Total GR curve from Gardner et al. (2013) is to the right of the BP Total GR Curve. BLs have been adjusted to best fit GR curves in order to compare log patterns.

Table 10. Abundance of grain-dominated vs. mud-dominated texture at the Colonel Bend (East) site calculated using the brightness log and polynomial trend lines. "% Grain-dominated texture" for each facies represents the amount of outcrop rock in that facies that is brighter than the polynomial trend line. "% Mud-dominated texture" represents the amount of outcrop rock in that facies that is less bright than the polynomial trend line.

Colonel Bend Brightness Log – Trend line Calculation for Abundance of Grains vs. Mud				
Facies	**Total Measurement Count**	**Brighter than Trend Line**	**% Grain-Dominated Texture**	**% Mud-Dominated Texture**
E	537	360	67.0%	33.0%
D	478	63	13.2%	86.8%
C	850	619	72.8%	27.2%
B	1588	459	28.9%	71.1%
A	396	249	62.9%	37.1%

4.4 Fracture Characterization

Fractures in Eagle Ford group Facies B and Facies C were analyzed from 2-D planar orthomosaics of outcrop faces from the Scott Ranch, Colonel Neck, and Colonel Bend study sites. Average measurements (mean/median) were reported for several fracture characteristics: apparent vertical fracture extent, apparent lateral fracture extent, apparent fracture spacing, and apparent fracture dip (Table 11; See Appendix C). Because of the large sample sizes of fractures (over 10,000 measured total) median values were mostly used in reporting fracture results because they were less effected by outlier data points than the mean values.

The data show that apparent vertical and lateral fracture extent (Figure 45 & Figure 46) and apparent fracture spacing (Figure 47) are less in Facies B than in Facies C at each respective study site. Facies B exhibits greater P_{21} apparent fracture intensity than Facies C (Figure 48). In general, fractures are shorter (vertically and laterally), more closely spaced, and more numerous in Facies B than in Facies C.

Average apparent dip (Figure 49) measured at the Scott Ranch site tends to be less inclined (~ 67°) than the steeper apparent dips measured at the Colonel Neck site (~75°) and Colonel Bend site (~73°) (Table 11). Average vertical and lateral extents of fractures are noticeably shorter at the Scott Ranch site in both Facies B and Facies C than the other two study sites (Figure 45 & Figure 46; Table 11). In both Facies B and Facies C, Scott Ranch median apparent vertical fracture extents are close to 1 ft (30 cm) shorter than median apparent vertical fracture extents at the Colonel Bend site. Average apparent spacing of fractures in both Facies B and Facies C at the Colonel Neck study site are significantly shorter than apparent spacing of fractures at the Scott Ranch and Colonel Bend sites (Figure 47; Table 11). Generally, within Facies B and Facies C, the shorter the apparent spacing of fractures, the more inclined the apparent dip (Table 11).

Fracture orientation cannot be accurately measured directly from 2-D orthomosaics of outcrop faces, thus, it was not measured in Lozier Canyon 2-D orthomosaics as part of this study (Casini et al., 2016). Field-measured fracture orientations in nearby Antonio Creek suggest a dominant set of fractures oriented N20°E, and a secondary fracture set oriented N60°W (Figure 50).

Table 11. Average fracture characteristics of Facies B and Facies C identified and measured visually from 2-D orthomosaics built from DOMs. Average values are reported in feet (mean/median).

Eagle Ford Facies:	Facies B Fractures			Facies C Fractures		
Study Site:	Scott Ranch (North)	Colonel Neck (North)	Colonel Bend (West)	Scott Ranch (North)	Colonel Neck (North)	Colonel Bend (West)
Count:	2,040	3,261	2,707	626	824	638
App. Vertical Extent (ft)	1.3 / 0.9	2.8 / 1.7	2.6 / 1.8	1.2 / 1.0	4.2 / 2.6	2.8 / 2.1
App. Lateral Extent (ft)	0.6 / 0.4	0.7 / 0.5	0.7 / 0.5	0.5 / 0.4	1.1 / 0.8	0.9 / 0.7
Apparent Spacing (ft)	5.6 / 3.3	3.2 / 2.0	5.0 / 3.1	6.8 / 3.7	3.7 / 2.7	6.6 / 3.4
Apparent Dip	64.8° / 66.8°	73.2° / 75.1°	71.8° / 73.4°	64.5° / 66.9°	72.1° / 74.7°	71.3° / 72.8°
Apparent Intensity (ft^{-1})	0.67	0.87	0.58	0.56	0.81	0.45

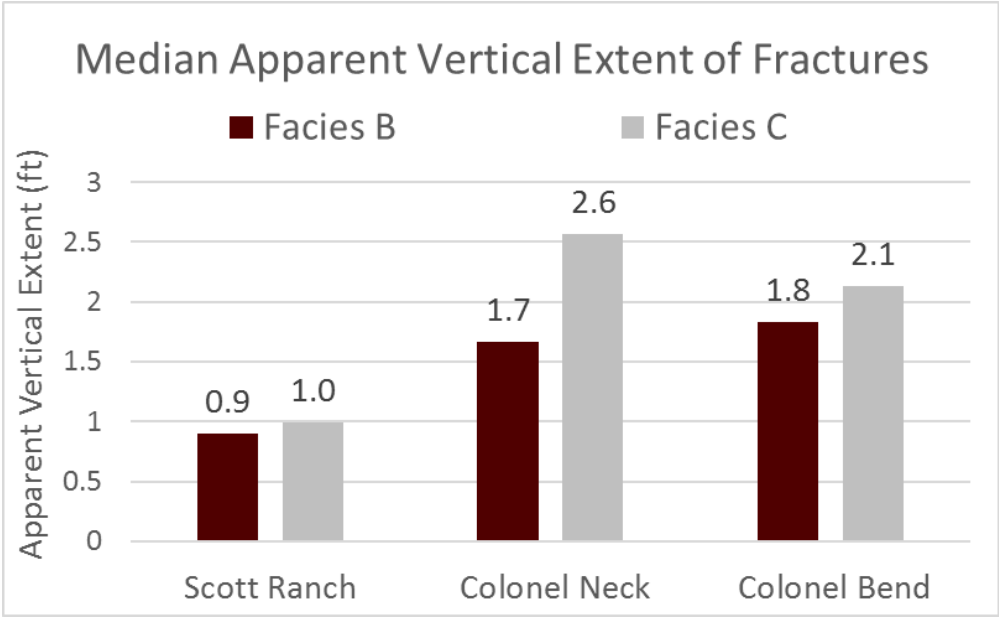

Figure 45. Median apparent vertical extent of fractures measured using 2-D orthomosaics from the Scott Ranch, Colonel Neck, and Colonel Bend study sites.

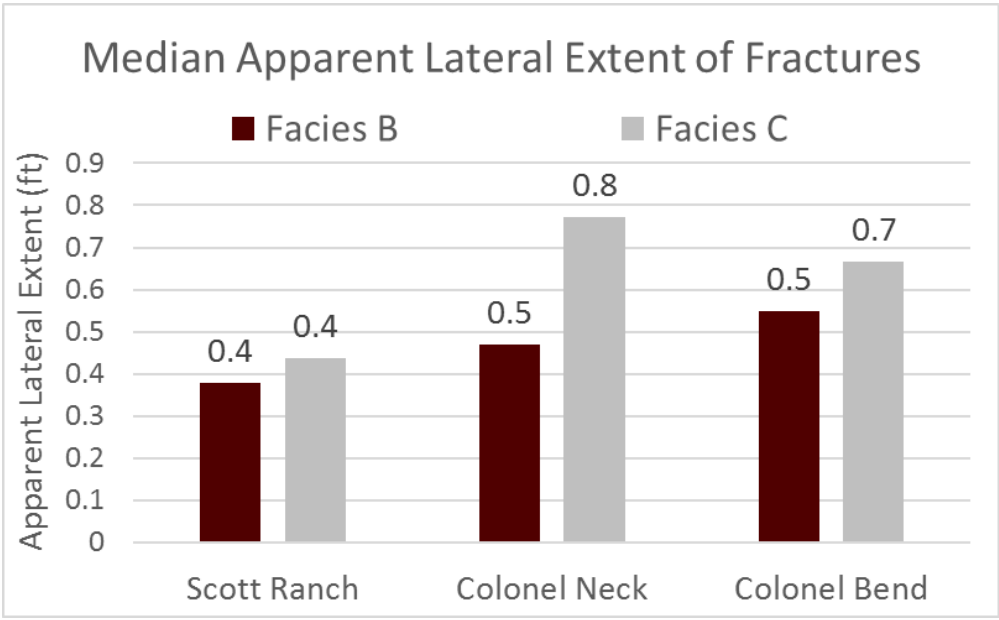

Figure 46. Median apparent lateral extent of fractures measured using 2-D orthomosaics from the Scott Ranch, Colonel Neck, and Colonel Bend study sites.

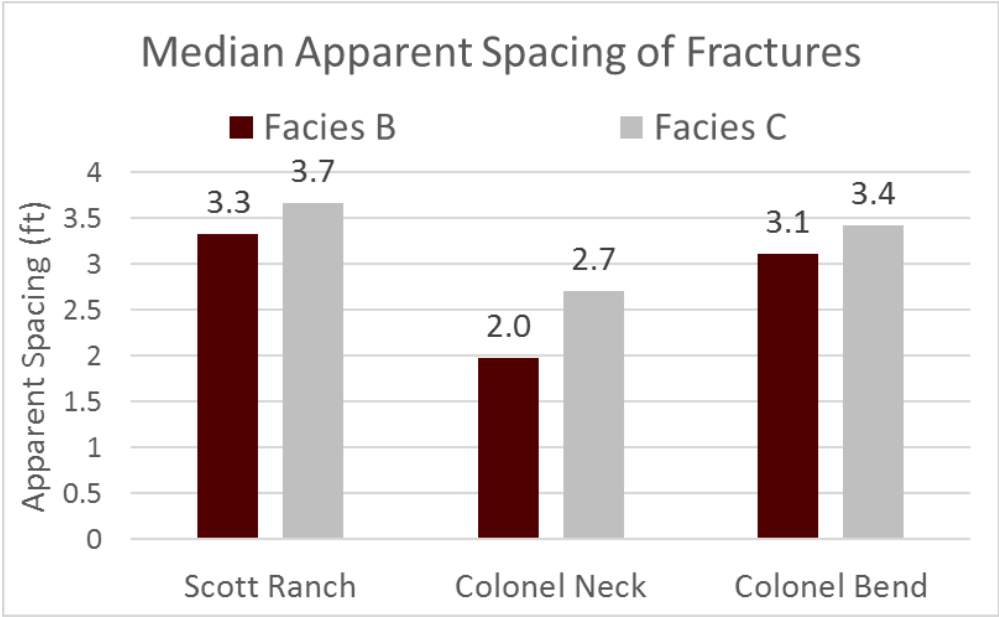

Figure 47. Median apparent spacing of fractures measured using 2-D orthomosaics from the Scott Ranch, Colonel Neck, and Colonel Bend study sites.

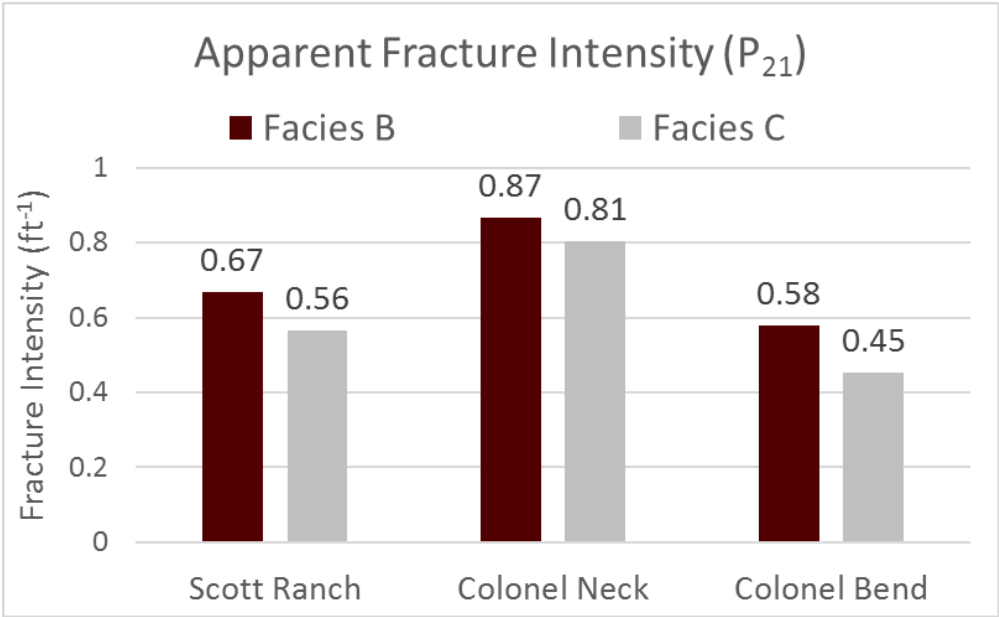

Figure 48. Apparent fracture intensity (P_{21}) calculated with measurements from 2-D orthomosaics of the Scott Ranch, Colonel Neck, and Colonel Bend study sites following (Mauldon et al., 2001) methodology.

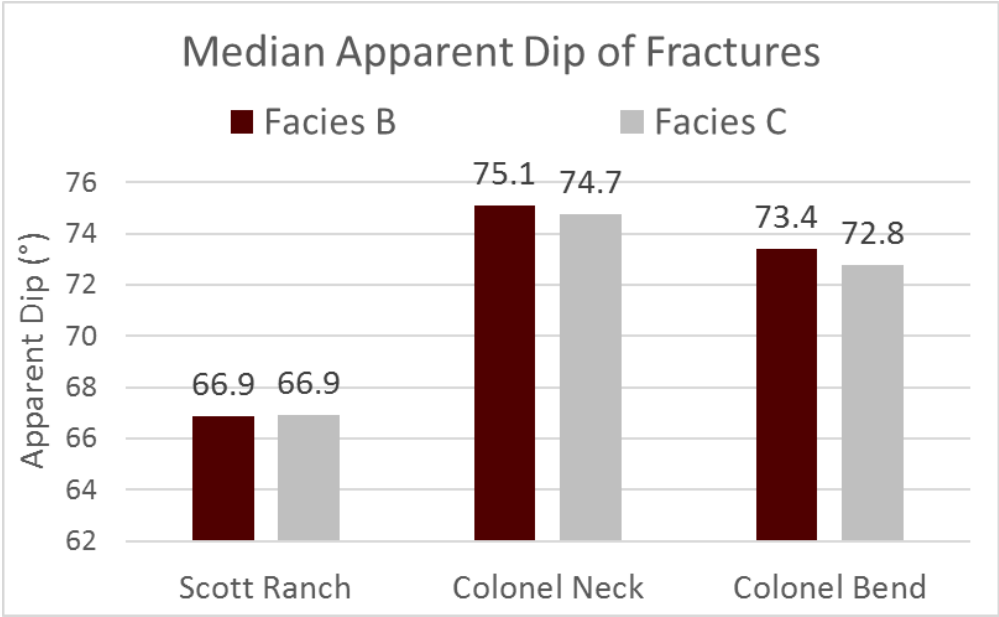

Figure 49. Median apparent dip of fractures calculated with measurements from 2-D orthomosaics of the Scott Ranch, Colonel Neck, and Colonel Bend study sites.

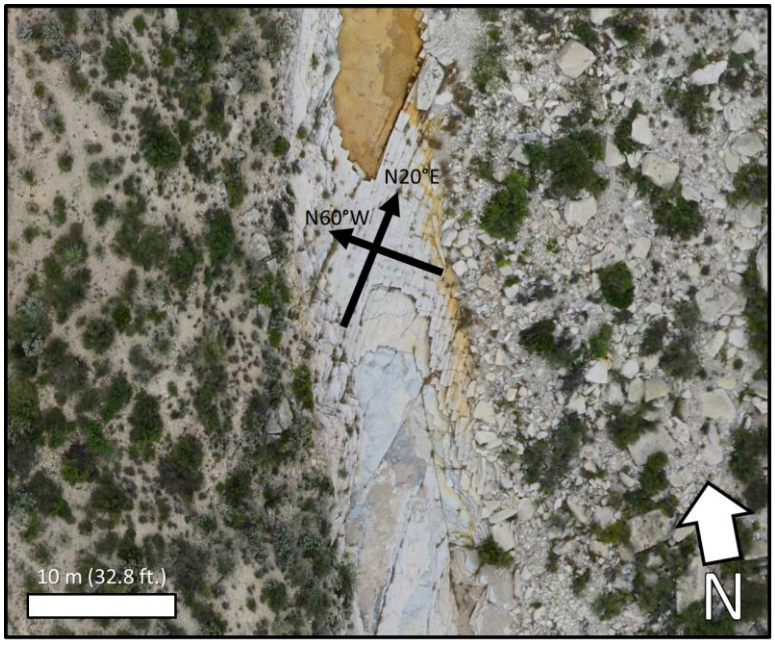

Figure 50. Pavement of Eagle Ford group Facies B, most likely Sub-facies B1 or B2, in Antonio Creek (Lat. = 29.847240°, Long. = -101.772626°). Fractures are predominantly oriented N20°E with some fractures cutting across oriented N60°W.

5. DISCUSSION

The Eagle Ford group generally thickens towards the south-southeast across state of Texas. In Lozier Canyon, Eagle Ford group strata increases by an average of 27.8 ft (8.47 m), a 13.59% increase in thickness, from north-to-south Lozier Canyon. These thicknesses are consistent with interpreted regional isopach maps (Figure 51) by Freeman (1968). Several wells were drilled to the southeast of the Lozier Canyon study area that confirm this regional variation. For example, the Shell research core Iona-1, located 75 mi (120.7 km) southeast of south Lozier Canyon near the Devils River Buildups (Figure 3), records an Eagle Ford group thickness of 365.8 ft (111.5 m), which is 161.2 ft (49.13 m) thicker than the average Eagle Ford group section in south Lozier Canyon (Eldrett et al., 2015). Eagle Ford group strata in the Maverick Basin, located about 100 miles (161 km) southeast of Lozier Canyon (Figure 3), is as thick as 650 ft (198.1 m) (Tian et al., 2012). Located southeast of the Maverick Basin were the South Texas Submarine Plateau, and the continental slope break (Figure 3B). These structural features resulted in progressively increasing water depths and accommodation toward the south-southeast that influenced deposition of Eagle Ford group sediments (Figure 3B).

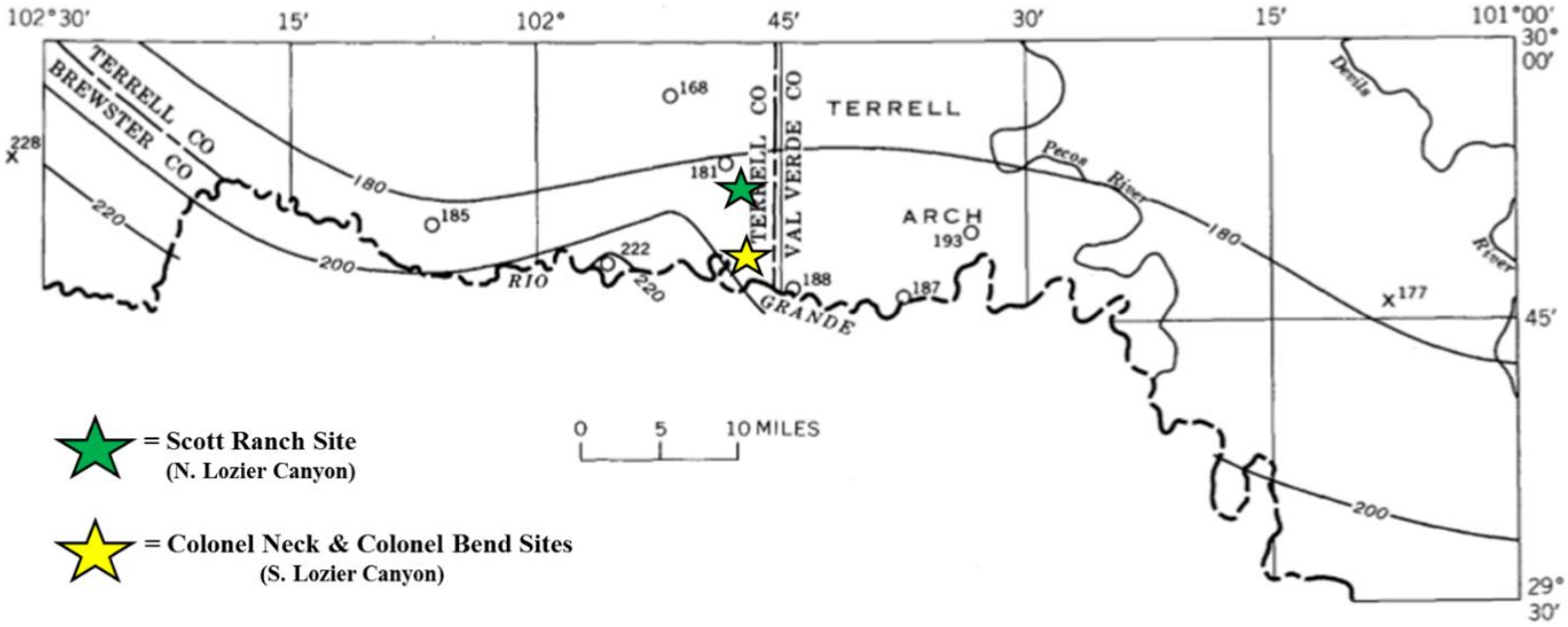

Figure 51. Isopach map of the Eagle Ford group in southwest Texas with the Scott Ranch (green star) and south Lozier Canyon (yellow star) study sites annotated. Modified from Freeman (1968).

5.1 Sedimentological Controls on Eagle Ford Group Deposition

Siliciclastic systems derive sediment from extra-basinal sources, whereas carbonate systems generate sediment from intra-basinal sources (Catuneanu, 2006). The Eagle Ford group, comprised of alternating beds of organic and clay-bearing calcareous mudstone and skeletal WS/PS/GS beds, was deposited within a mixed carbonate-clastic system. The two overriding controls governing sediment production and supply in any environment are tectonics and climate (Nichols, 2009; Tucker and Wright, 1990).

The primary skeletal grain constituent of the Eagle Ford group is pelagic foraminifera. Carbonate producing biota, such as pelagic foraminifera, rely on nutrients such as phosphate and iron to sustain high levels of production (Jones and Gislason, 2008). These nutrients are generally supplied to ocean waters by upwelling, or the influx of terrigenous sediments. Scholle et al. (1983) established that terrigenous sediments were the most dominant control on the accumulation of pelagic foraminifera during the Mid-to-Late Cretaceous.

Windblown volcanic ash, dominantly sourced by Sevier orogenic activity in Mexico west of the Western Interior Seaway (WIS), was delivered episodically and quite uniformly to the south Texas region throughout the Cretaceous (Deluca, 2016; Pierce et al., 2016). This is best evidenced by geochemical analysis of the numerous layered ash beds in the Eagle Ford group throughout south Texas (Pierce et al., 2016). Mineralogically, ash beds in the Lozier Canyon area dominantly are iron-oxides and clays (Deluca, 2016). Eagle Ford group ash beds in Comstock, TX, about 37 mi (59.5

km) east of Lozier Canyon, contained iron-bearing illite and minor amounts of hematite and pyrite (Pierce et al., 2016). These ash beds likely sourced much of the iron necessary to support biotic carbonate production across most of the platform.

In south Texas, under Mid-Cretaceous greenhouse conditions, temperatures and humidity increased, sea-levels rose, and precipitation increased (Hasegawa et al., 2012). Greater amounts of precipitation generally increase the intensity of erosional processes leading to greater volumes of transported sediment (Nearing, 2004; Nichols, 2009). Though, in the Mid-Cretaceous, increased erosional processes may have been somewhat compensated by the reduction in subaerially exposed landmass susceptible to erosion (Hallam, 1977). At that time, the vast majority of terrigenous sediments delivered to the south Texas region would have traveled from western Sevier orogenic sources almost entirely by fluvial processes following the traditional siliciclastic model of decreasing energy and sediment particle size with increasing distance (Nichols, 2009). Consequently, mature silts and clays that reached south Texas would have been deposited in troughs along the southwest and northeast platform margins and down-ramp toward the continental slope break (Figure 3A). Some fine terrigenous sediment in suspension likely was pushed up onto the carbonate platform top by high energy wave action produced by strong westerly trade winds and storms (Hasegawa et al., 2012).

It is most likely that the influx of volcanic ash was the controlling factor for production of pelagic carbonate sediments on the interior platform (Frébourg et al., 2016). After an episodic influx of nutrient-laden volcanic ash, pelagic foraminifera would begin to amass. Waves and surface currents within the WIS, generated primarily

by storms and westerly trade winds, would have re-worked and influenced deposition of these sediments (Hasegawa et al., 2012). Re-working of Eagle Ford sediments is apparent in the hummocky cross-stratification that dominates Facies A and E, as well as the lenticular bedding prevalent in Facies B (Wehner et al., 2015). During deposition of the Lower Eagle Ford formation (~ 97.2 – 94 Ma) the depositional environment is interpreted to have been an anoxic restricted shelf best evidenced by a lack of bioturbation and high TOC values (Deluca, 2016; Donovan et al., 2012; Donovan et al., 2016; Gardner et al., 2013). Circulation was restricted and bottom currents, driven by temperature and water density gradients, would have likely been weak. This is because temperature and water density (a product of temperature, salinity, and water depth) probably did not vary much within the restricted platform (Caron and Homewood, 1983). This restriction would likely have favored an increase in salinity on the interior platform away from platform margins as a result of poor circulation, analogous to the modern Bahama Platform (Tucker and Wright, 1990). Warmer, anoxic, and higher saline water atop the Comanche Platform would have differed considerably from the cooler and less saline waters of the Arctic Ocean and Tethys seaway.

However, as pre-existing accommodation on the Comanche Platform was filled during deposition of the Lower Eagle Ford formation and sea-level kept rising into the Turonian, the Arctic Ocean, WIS, and Tethys seaway were connected (Sageman et al., 1997). This connection led to more open circulation and likely significant changes in water density. Bottom circulation may have intensified due to the increased mixing of colder arctic ocean waters with warmer platform and Tethys waters (Gardner et al.,

2013). This adaptation of bottom current patterns likely encouraged the transportation of greater volumes of sediment from the platform top into pre-existing topographic lows such as the Maverick and Sabinas basins, the South Texas Submarine Plateau, and down-ramp toward the continental slope break. Once sediment settled into these topographic lows below storm wave base, it was considerably less likely to be disturbed.

Deposition of the Upper Eagle Ford formation (~ 92.5 – 91 Ma) took place in more oxygenated conditions best evidenced by widespread burrowing and a decrease in uranium abundance (Deluca, 2016; Gardner et al., 2013). Rising sea levels, driven by greenhouse conditions, increased the amount of submerged surface area which covered about 35% of the modern North American landmass at peak transgression (Hallam, 1977). This flooding led to greater carbonate production and relatively slow sea-level rise between 10 – 90 m/Ma (32.8 – 295.3 ft/Ma) allowing the carbonate factory to keep pace with overall sea-level rise (Catuneanu, 2006; Hancock and Kauffman, 1979). Differences between the stagnant, anoxic, Lower Eagle Ford and the openly circulated, oxygenated Upper Eagle Ford most likely led to its depositional variability.

5.2 Stratigraphic Variability

DOM measurements indicate that each facies of the Eagle Ford group increases in thickness toward south Lozier Canyon. The overall Eagle Ford group decreases in total thickness by 1 ft (0.30 m) between the Scott Ranch site and side tributary Antonio Creek located just 4 mi (6.44 km) southeast of the Scott Ranch study site (Figure 2), and

2.5 mi (4.02 km) northeast of south Lozier Canyon (Gardner et al., 2013). Considering the paleogeographic location of Lozier Canyon on the Comanche Platform (Figure 3), Antonio Creek would have been located more toward the shallower platform interior east of the Scott Ranch site and south Lozier Canyon. South Lozier Canyon, which is substantially thicker Eagle Ford group compared to the Scott Ranch and Antonio Creek sites would have been situated somewhat closer to the southwestern platform margin. As the WIS continued to deepen due to basin subsidence and rising seas throughout the Mid-to-Late Cretaceous, deeper shelf environments toward the southwest platform margin would have continued to collect sediments at a greater rate than shallow environments nearer to the San Marcos Arch east of Lozier Canyon (Donovan et al., 2016; Laubach and Jackson, 1990; Workman, 2013). This southwestward thickening from the Scott Ranch site toward the platform margin reflects an increase in accommodation toward the Chihuahua Trough and the Sabinas Basin (Figure 3) formed in the early Mesozoic on the southwestern margin of the North American craton (Alsaab et al., 2007; Freeman, 1968; Gardner et al., 2013).

Eagle Ford group exposures in Lozier Canyon and Antonio Creek cover an area of ~ 7.5 mi^2 (19.42 km^2) (Figure 2). Local thickness variability of the Eagle Ford group within this area is likely not related to sediment production rates. Volcanic ash, the limiting factor on the production of pelagic foraminifera, would have been distributed uniformly over the canyon area suggesting consistent nutrient availability and similar sediment production rates. Rather, increasing accommodation to the southwest and

erosional processes likely account for present day thicknesses of Eagle Ford group strata at Lozier Canyon.

DOM measurements indicate that each facies of the Eagle Ford group increases in thickness toward south Lozier Canyon. The largest difference in average thickness between the Scott Ranch site and south Lozier Canyon is in Facies C displaying a 20.18% increase to the south. This increase may be attributed to the disconformity that separates Facies C from Facies D (Figure 5). The most variable Eagle Ford group sub-facies, Sub-facies C3 (uppermost Facies C), was 36.4% thicker at the Scott Ranch site compared to Antonio Creek (Gardner et al., 2013). If variability within Facies C was dominantly controlled by accommodation, we would expect to observe increasing individual bed thicknesses within Facies C to the southwest. However, 2-D orthomosaic measurements of correlative skeletal WS – PS beds in Facies C show generally consistent bed thicknesses, between 2 – 12 in (6 – 30 cm), in both north and south Lozier Canyon (Figure 42). Furthermore, overlying Facies D showed the smallest difference in average thickness between the Scott Ranch site and south Lozier Canyon at 5.71%. Sometime between 94 – 92.5 Ma (Figure 5), erosional processes, best evidenced by rip-up clasts between Facies C and D, most likely beveled the topographic surface in upper Facies C creating a more even surface for subsequent deposition of Facies D (Deluca, 2016; Gardner et al., 2013). This may explain why Facies C displays the greatest amount of variability at Lozier Canyon whereas Facies D shows such little variation.

5.2.1 Effect of Depositional Environment on Stratigraphic Variability

Facies A, B, and E display sedimentary structures such as symmetric ripples, convex and concave internal laminae geometry, and lenticular bedding characteristic of hummocky cross-stratification (Donovan and Staerker, 2010; Donovan et al., 2012; Donovan et al., 2016; Gardner et al., 2013; Lyon, 2015; Trevino, 1988; Wehner et al., 2015). Facies A and Facies E are interpreted to have always been above storm wave base as indicated by the prevalence of symmetrical wave-formed sedimentary structures, whereas Facies B is interpreted to have been above storm wave base episodically indicated by lesser amounts of hummocky cross-stratification, lenticular bedding, and erosional scouring surfaces (Donovan and Staerker, 2010; Gardner et al., 2013; Wehner et al., 2015). This differs from interpretations that the observed inclined stratification in Facies A are current driven contourites deposited in moderately deep water (Lock and Peschier, 2006). However, the predominant internal stratification is symmetrical wave-formed structures, rather than asymmetrical current-driven structures, indicating they are hummocks (Donovan and Staerker, 2010; Lyon, 2015; Wehner et al., 2015).

Gardner et al. (2013) suggest that pre-existing topography on the Comanche Platform is most likely responsible for thickness variation of the Lower Eagle Ford formation (Facies A and B). Topographic lows may have been partially filled during deposition of Facies A and Facies B creating a level surface for deposition of subsequent facies of the Upper Eagle Ford formation to be deposited more evenly (Gardner et al., 2013). This explanation is supported by laterally continuous skeletal WS – PS beds in

Facies C (Figure 42) and the upward increase in oxygen interpreted by increasing bioturbation and decreasing uranium content beginning in Facies C (Gardner et al., 2013). Thickness variability in Facies E is likely related to the erosional contact that separates the Eagle Ford group from the Austin Formation (Figure 5).

Regarding BLs, high-resolution outcrop BLs aided in correlating stratigraphic surfaces throughout Lozier Canyon. Outcrop brightness values, measured at about 2 in (5 cm) vertical intervals in 2-D orthomosaics, provide much greater resolution than the resolution achieved by standard GR curves. BLs were useful in discerning the contact between the Lower and Upper members of the Lower Eagle Ford formation that separates the organic-rich primary reservoir from the avoided bentonite-rich zone (Figure 44). The Colonel Bend BL provided the most reasonable estimates for lithofacies abundances likely due to higher quality outcrop exposure and more uniform lighting conditions (Table 11). In the future, Lozier Canyon BLs have the potential to aid in astrochronologic study. In the Iona-1 core, Eldrett et al. (2015) demonstrates that brightness values of the Eagle Ford group may be used to determine orbital signals. Refined outcrop BLs of Eagle Ford group strata bounded by known ash bed dates may have potential application in determining sedimentation rates and cyclostratigraphy of the Eagle Ford group at Lozier Canyon (Deluca, 2016).

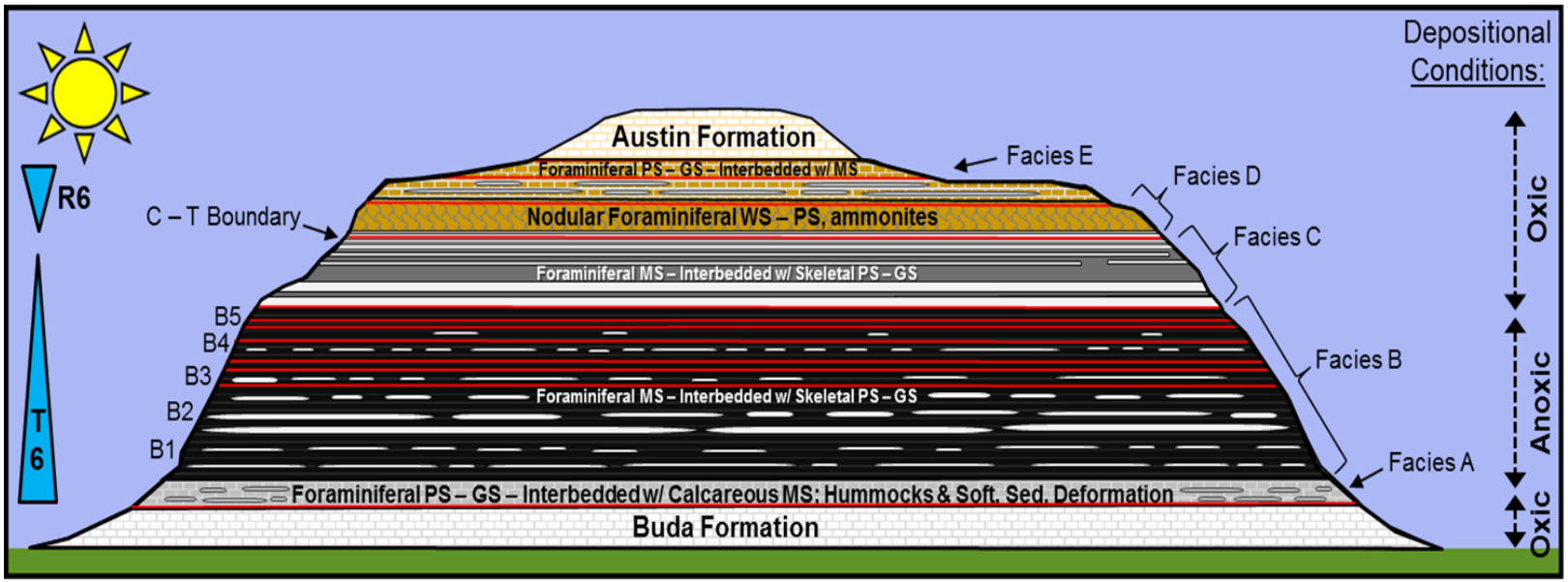

Figure 52. Generalized illustration of Eagle Ford group outcrop at Lozier Canyon. Horizontal red lines represent ash beds. White lens-shaped bodies in Facies A, B, C, and E represent interbedded skeletal grain-rich beds. Colors used for the Buda Formation, Eagle Ford group facies, and Austin Formation are based on color descriptions of fresh surfaces from those units. The C – T boundary is illustrated on the left side of the figure just beneath the Facies C – D contact.

5.2.2 Stratigraphic Variability Within Facies B

At the Scott Ranch site, dark organic calcareous mudstone comprises about 80% of Facies B by volume and they are interbedded with skeletal PS – GS beds that account for roughly 15% of the unit volume (Gardner et al., 2013). Ash beds are numerous in the Upper member of the Lower Eagle Ford formation (Sub-facies B3, B4, & B5) and account for about 5% of the unit volume (Figure 6 & Figure 52) (Gardner et al., 2013). These ash beds indicate a drastic increase in volcanic activity that likely impacted pelagic sediment production. Influx of this volcanic ash delivered a boost of iron that most likely would have encouraged a short-term bloom of primary producing pelagic organisms that waned once nutrients were depleted (Frébourg et al., 2016). To support this relationship between increased volcanic activity and skeletal PS – GS beds in Facies B, Frébourg et al. (2016) notes that skeletal PS – GS beds typically overlie volcanic ash beds. While this phenomenon is observed in outcrop at Lozier Canyon, it is also common to find skeletal PS – GS beds, such as in Sub-facies B1 & B2, that do not directly overlie ash beds.

Significant increases in nutrient supply would suggest a boom in pelagic foraminifera production; however, as ash beds appear more frequently Sub-facies B3, B4, and B5, skeletal PS – GS beds become less frequent at the Scott Ranch site. Moving upward in the section from the B3 – B4 contact, Eagle Ford strata becomes increasingly mud-dominated and skeletal PS – GS beds become less continuous (Figure 41 & Figure 52). This is likely related to backstepping of the shoreline and increased flooding of the

platform during the T6 Cenomanian-Turonian transgressive cycle leading into the Sub-facies B5 highstand (Donovan and Staerker, 2010; Donovan et al., 2012; Donovan et al., 2015; Donovan et al., 2016; Hart, 2015). As sea level rose, Lozier Canyon likely transitioned into a more distal environment with greater water depths. Changing environmental conditions, increasing temperatures, and increased water depth may have altered water density and reduced pelagic foraminifera production in the area (Caron and Homewood, 1983). Thus, basal Facies B strata would represent a shallow and more proximal depositional environment while upper Facies B strata would preserve more mud-dominated distal portions.

Throughout Facies B, skeletal PS – GS beds are mostly discontinuous and broken up into individual lenses. Wavy and lenticular bedded skeletal PS – GS bedforms are common throughout Facies B, especially in Sub-facies B3 and B4. These bed morphologies were interpreted to be distal storm beds formed above storm wave base (Gardner et al., 2013; Wehner et al., 2015). This interpretation is based on the presence of symmetric ripples in Facies B that suggest oscillatory flow environments indicative of wave action (Nichols, 2009; Wehner et al., 2015). For this reason, bottom currents are unlikely to have influenced bed morphology in Facies B, as asymmetrical ripples signifying unidirectional flow would be expected to be far more prevalent.

Skeletal PS – GS lenses have the longest apparent lens lengths and are most continuous in Sub-facies B2 (Figure 40; Table 8). High TOC values suggest that anoxia was greatest during this time and greater bed continuity indicates that bottom waters were likely stagnant and generally below storm wave base. Thus, stagnation, anoxia, and

weak-to-inactive bottom currents likely account for longer apparent lens lengths, greater bed continuity, and the lack of skeletal PS – GS bedforms observed in Sub-facies B2 (Figure 52).

The lateral continuity of skeletal PS – GS beds within Facies B of the Eagle Ford group was studied in U.S. Route 90 outcrops near Comstock, Texas about 37 mi (59.5 km) east of the Scott Ranch study site (Frébourg et al., 2016). The vast majority of bentonite ash beds in Facies B are not laterally continuous; however, they are generally more continuous than pelagic GS beds (Frébourg et al., 2016). The thickness of pelagic GS beds does not vary much between sub-facies (Frébourg et al., 2016). DOM results from the Scott Ranch site compliment these findings; ash beds are significantly more laterally continuous than skeletal PS – GS beds and bed thicknesses do not differ substantially between sub-facies.

5.3 Relationship Between Fractures and Strata

Fractures are influenced by lithology, bed thickness, bed competency, and the degree of deformation (Ladeira, 1981). In general, as bed thickness increases, fracture spacing proportionally increases (Price, 1966; Wu and D. Pollard, 1995). In the Eagle Ford specifically, McGinnis et al. (2017) has demonstrated this relationship in a recent study of the Ernst Member of the Boquillas Formation (equivalent to the Eagle Ford group) at Ernst Tinaja in Big Bend National Park, located 84 mi (135.2 km) southwest of the Scott Ranch study site. This study confirms that as thickness of competent skeletal

PS – GS beds increases, fracture spacing increases proportionally (McGinnis et al., 2017). This is likely related to the brittle nature of skeletal grain-rich beds that promote fracture propagation far more than ductile clays that tend to inhibit fracture growth (McGinnis et al., 2017).

Results from Lozier Canyon DOMs support this argument as Facies C, which features thicker-bedded and more continuous skeletal grain-rich beds (2-12 in thick (6-30 cm)), displays greater apparent fracture spacing (Figure 47) and apparent vertical and lateral fracture extents (Figure 45 & Figure 46), compared to mud-dominated Facies B which features thinner skeletal PS – GS beds and lenses (1-6 in thick (3-15 cm)) (Gardner et al., 2013). Furthermore, DOM results suggest a relationship between skeletal PS – GS apparent lens length and apparent fracture intensity in Facies B; as median apparent lens length increases, apparent fracture intensity decreases (Figure 53). This relationship is most likely related to similar aspect ratios visually observed in outcrop between lens length and lens thickness (Figure 7B). As lens length increases, lens thickness appears to increase rather proportionally. This may explain why there are generally less fractures and greater fracture spacing when grain-rich limestone beds and lenses are greater in length and continuity in Eagle Ford group strata.

In both Facies B and Facies C (relative to study site), shorter apparent fracture spacing corresponds to higher-inclined apparent dips; and larger apparent fracture spacing corresponds to lower-inclined apparent dips (Figure 54; Table 11). This is expected based on the geometric relationship between outcrop strike and fracture orientation (Figure 55).

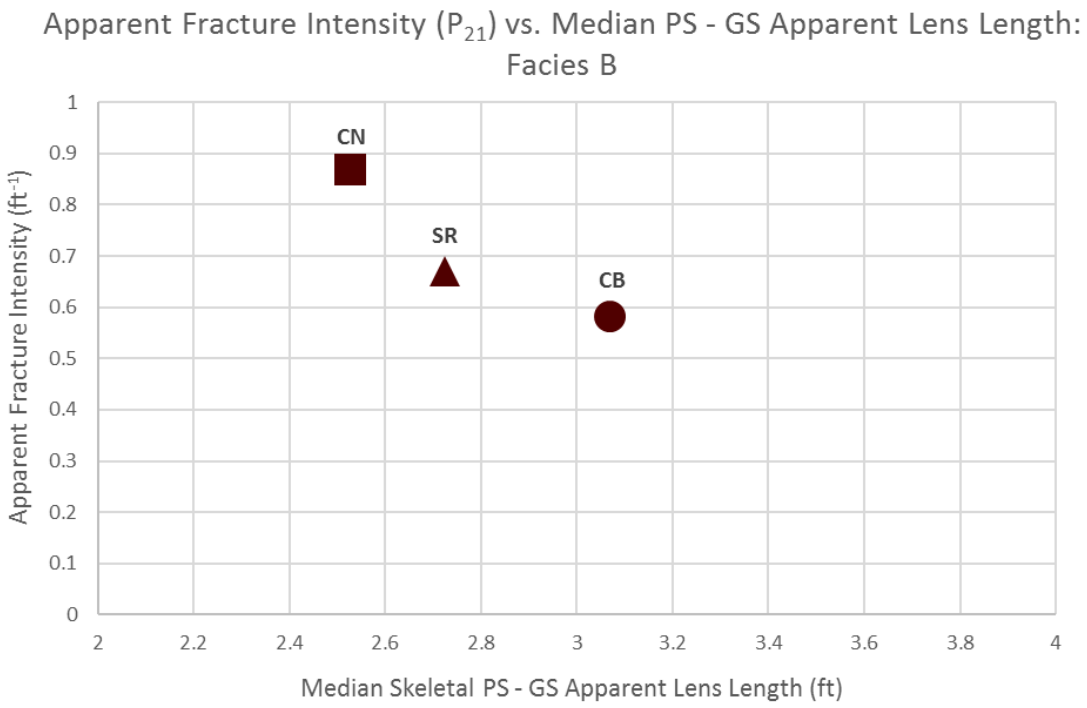

Figure 53. Scatter plot of apparent P_{21} fracture intensity (y-axis) versus median skeletal packstone – grainstone apparent lens lengths in Eagle Ford group Facies B. "SR" = Scott Ranch; "CN" = Colonel Neck; "CB" = Colonel Bend. As median apparent lens length increases, apparent fracture intensity decreases.

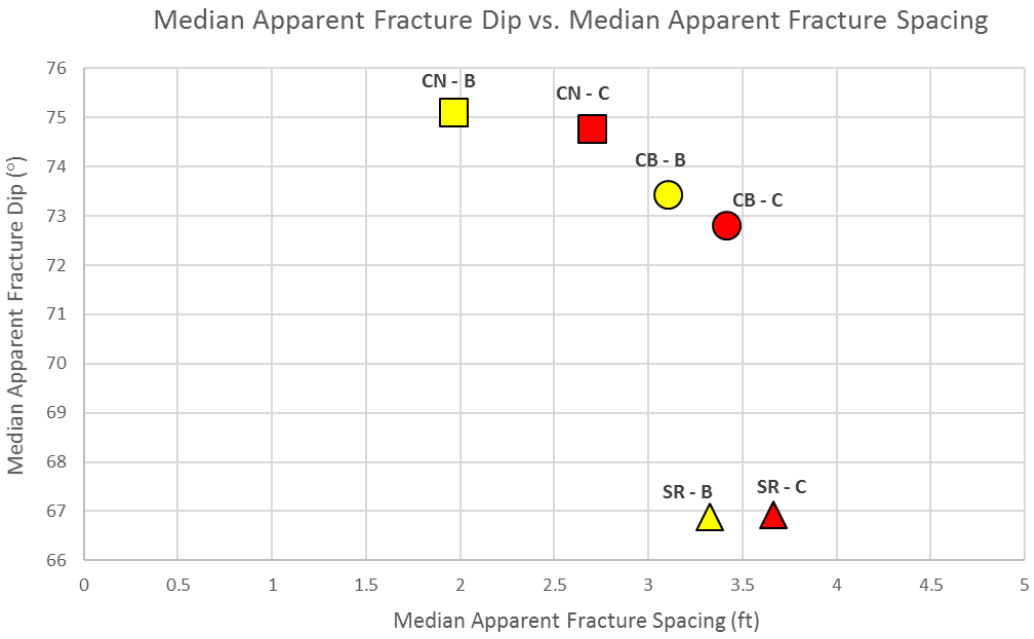

Figure 54. Scatter plot of median apparent fracture dip (y-axis) vs median apparent fracture spacing (x-axis). Yellow colors indicate Facies B results. Red Colors indicate Facies C results. “SR” = Scott Ranch; “CN” = Colonel Neck; “CB” = Colonel Bend. Scott Ranch has the lowest apparent dip values and the highest apparent spacing respective to facies.

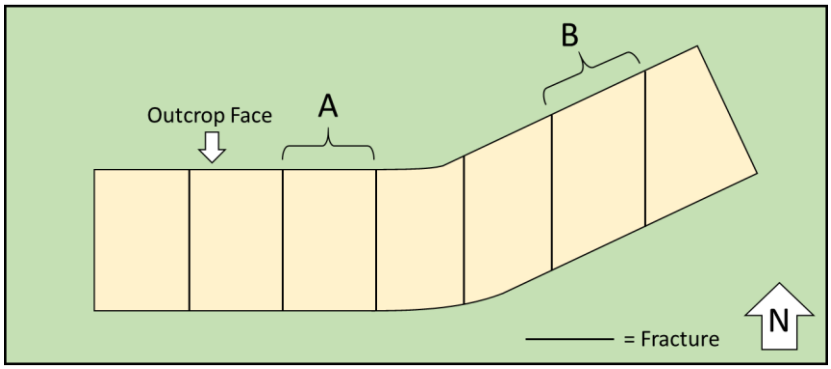

Figure 55. Cartoon illustrating how apparent fracture spacing is related to the strike of an outcrop face. This diagram is projected in map view. The tan polygon represents an outcrop with fractures (black lines) oriented north-south cutting through the outcrop. Apparent fracture spacing at location “A” would appear smaller and equal true fracture spacing. Apparent fracture spacing at location “B” will be greater even though fracture orientation has not changed.

The Colonel Neck site features the most inclined median apparent dips for fractures in Facies B and Facies C (75.1° & 74.7°) followed closely by the Colonel Bend study site (73.4° & 72.8°) (Figure 49 & Figure 54; Table 11). Scott Ranch site fractures have lower median apparent dips (66.9° & 66.9°) than both the Colonel Neck and Colonel Bend study sites (Figure 49 & Figure 54; Table 11). These results are most likely linked to the relationship between strike direction of outcrop faces and fracture orientations.

Outcrop faces at the Colonel Neck and Colonel Bend study sites have similar strike direction. The Colonel Neck site outcrop face strikes N70°W and the analyzed section of the Colonel Bend outcrop strikes N78°W (Figure 56). The Scott Ranch site outcrop face strikes N39°W (Figure 56). Based on field measurements from a few Antonio Creek Facies B pavements and observations of the area using Google Earth Pro, a dominant fracture set is oriented N20°E (Figure 50). Fractures oriented N20°E would be perpendicular to the N70°W striking Colonel Neck outcrop face and close to perpendicular at the N78°W striking Colonel Bend study site assuming that dominant fracture orientation remains consistent between Antonio Creek and Lozier Canyon (Figure 56). This fracture set would be oriented oblique relative to strike of outcrop faces at the Scott Ranch site. Thus, if the dominant orientation of fractures throughout north-and-south Lozier Canyon is N20°E, it would make sense that apparent fracture spacing would be smallest, and apparent dip values largest, at the Colonel Neck site (Figure 54). Large apparent fracture spacing and smaller apparent dip values would be expected at the Scott Ranch site and this hypothesis is supported by DOM results.

This discussion on fractures makes no distinction between fractures formed at depth and fractures formed due to exhumation. Therefore, fracture characteristics offered in this manuscript should not be assumed to flawlessly replicate fractures in the subsurface. Similarly, the reader must also be cautioned regarding the scale of fractures analyzed. Vegetation, debris, and digital photograph resolution limited fracture identification only to those that were readily apparent and able to be traced and analyzed. This methodology neglects many small fractures that were unidentifiable in 2-D orthomosaics and likely skews fracture results toward more observable macro-fractures. A more detailed fracture study that isolates fractures within each individual facies of the Eagle Ford for analysis would yield more complete results, however the methodology used in this work was efficient under time constraints and provides a general characterization of fractures in Facies B and Facies C. Extensive field study is needed to refine and supplement fracture characteristics in this study.

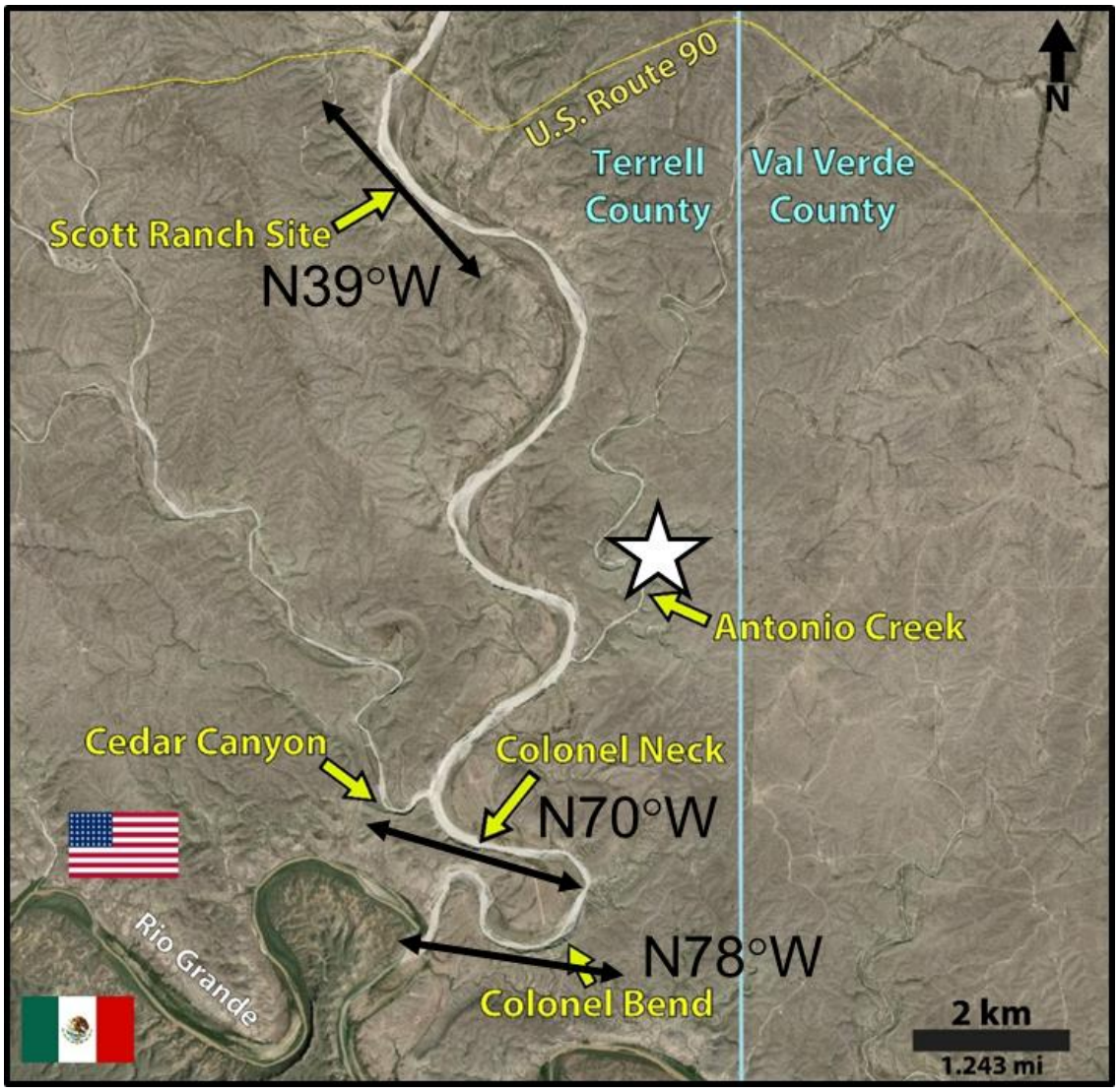

Figure 56. Study area with outcrop strike indicated and Antonio Creek pavement with N20°E oriented fractures shown with white star. Outcrop strike was measured using Google Earth Pro.

6. CONCLUSIONS

Lateral stratigraphic variability of the Eagle Ford group at Lozier Canyon was resolved using photogrammetry techniques and DOMs. The Eagle Ford group increases in average thickness by 13.59%, a 27.8 ft (8.47 m) difference, from the Scott Ranch site in north Lozier Canyon to south Lozier Canyon over a straight-line distance approximating 6.2 mi (10 km). DOM measured thicknesses of the Eagle Ford group at Lozier Canyon are consistent with regional thickness maps produced by Freeman (1968) that indicate general thickening from north-to-south. While climate was likely consistent across the south Texas region during the Mid-Cretaceous, tectonics certainly varied and influenced accommodation. Windblown volcanic ash was episodically distributed to the area uniformly supporting the notion that accommodation and erosional processes, not sediment supply, likely account for local stratigraphic variability observed in the Eagle Ford group at Lozier Canyon today.

Skeletal PS – GS beds and lenses become less laterally continuous moving up-section from the Sub-facies B2 – B5. We infer that increasingly mud-dominated strata in upper Facies B is related to back-stepping as a result of the T6 Cenomanian-Turonian transgressive cycle that placed the Lozier Canyon area in a more distal environment (Donovan and Staerker, 2010; Donovan et al., 2012; Donovan et al., 2015; Donovan et al., 2016; Hart, 2015). Hummocky bedding prevalent in Sub-facies B3 and B4 were likely formed as distal storm beds periodically above storm wave base.

Outcrop BLs are useful as a tool to analyze sub-meter scale bedding, differentiate between mudstone/grainstone textures, and to correlate with GR logs under the correct conditions (e.g. uniform lighting, minimal vegetation, and minimal debris). Outcrop BLs may have value in helping to determine orbital signals and sedimentation rates though more research is needed to improve and refine BLs for an astrochronologic study in Lozier Canyon.

A basic characterization of fractures in Facies B and Facies C was achieved using 2-D orthomosaics. The results suggest a direct relationship between fractures and bedding features in Eagle Ford group strata. Fractures identified in DOMs are generally shorter (vertically and laterally), more closely spaced, and more numerous in Facies B than in Facies C. This is related to the thickness, length, and frequency of brittle skeletal grain-rich bedding that is far more common in Facies C than Facies B. The relationship between apparent fracture spacing, apparent fracture dip, and outcrop strike was used to estimate a dominant fracture orientation.

This work has demonstrated the advantages of using UAVs to study lateral variability over large areas; especially in places less accessible by foot. Results from this study are ultimately intended to provide a basic stratigraphic framework in which future data may be stored to produce high-resolution reservoir models of the Eagle Ford group at Lozier Canyon. These reservoir models may have application for industry in predicting subsurface reservoir variability in the Eagle Ford group and in improving our understanding of other unconventional carbonate mudstone reservoirs such as the Haynesville and Utica shales. Lozier Canyon DOMs may also be used as a teaching

tools to allow students to visit Eagle Ford group outcrops virtually in the classroom, and to provide a workflow for subsequent studies at Texas A&M University which may require the construction of 3-D DOMs in the study of outcrop exposures.

REFERENCES

Alsaab, D., Suarez-Ruiz, I., Elie, M., Izart, A., and Martinez, L., 2007, Comparison of generative capacities for bitumen and gas between Carboniferous coals from Donets Basin (Ukraine) and a Cretaceous coal from Sabinas–Piedras Negras Basin (Mexico) during artificial maturation in confined pyrolysis system: International Journal of Coal Geology, v. 71, no. 1, p. 85-102.

Barron, E. J., and Washington, W. M., 1984, The role of geographic variables in explaining paleoclimates: Results from Cretaceous climate model sensitivity studies: Journal of Geophysical Research: Atmospheres, v. 89, no. D1, p. 1267-1279.

Bemis, S. P., Micklethwaite, S., Turner, D., James, M. R., Akciz, S., Thiele, S. T., and Bangash, H. A., 2014, Ground-based and UAV-Based photogrammetry: A multi-scale, high-resolution mapping tool for structural geology and paleoseismology: Journal of Structural Geology, v. 69, Part A, p. 163-178.

Bice, K. L., and Norris, R. D., 2002, Possible atmospheric CO_2 extremes of the Middle Cretaceous (late Albian - Turonian): Paleoceanography, v. 17, no. 4, p. 22-21 - 22-17.

Birch, J. S., 2006, Using 3DM Analyst Mine Mapping Suite for Rock Face Characterisation, *in* Tonon, F., and Kottenstette, J. T., eds., The 41st U.S. Rock Mechanics Symposium, Laser and Photogrammetric Methods for Rock Face Characterization: Golden, Colorado, American Rock Mechanics Association, p. 13-32.

Bowman, M. B. J., and Smyth, H. R., 2016, Reducing uncertainty and risk through field-based studies, Geological Society of London, Geological Society Special Publication, 1-8 p.:

Caron, M., and Homewood, P., 1983, Evolution of Early Planktic Foraminifers: Marine Micropaleontology, v. 7, no. 1982/1983, p. 453-462.

Casini, G., Hunt, D. W., Monsen, E., and Bounaim, A., 2016, Fracture characterization and modeling from virtual outcrops: AAPG Bulletin, v. 100, no. 1, p. 41-61.

Catuneanu, O., 2006, Principles of Sequence Stratigraphy, Amsterdam, The Netherlands, Elsevier.

Deluca, M. J., 2016, Ash Bed Analysis of the Cretaceous Eagle Ford Shale using ID-TIMS U/PB Methods: Implications for Biostratigraphic Refinement and Correlations within the Western Interior Seaway [Master's Thesis]: Texas A&M University, 68 p.

Donovan, A. D., and Staerker, T. S., 2010, Sequence Stratigraphy of the Eagle Ford (Boquillas) Formation in the Subsurface of South Texas and the Outcrops of West Texas: Transactions - Gulf Coast Association of Geologic Societies, v. 60, p. 861-899.

Donovan, A. D., Staerker, T. S., Pramudito, A., Li, W., Corbett, M. J., Lowery, C. M., Romero, A. M., and Gardner, R. D., 2012, The Eagle Ford Outcrops of West Texas: A Laboratory for Understanding Heterogeneities within Unconventional Mudstone Reservoirs: Gulf Coast Association of Geologic Societies Journal, v. 1, p. 162-185.

Donovan, A. D., Gardner, R. D., Pramudito, A., Staerker, T. S., Wehner, M., Corbett, M. J., Lundquist, J. J., Romero, A. M., Henry, L. C., Rotzien, J. R., and Boling, K. S., 2015, Chronostratigraphic Relationships of the Woodbine and Eagle Ford Groups across Texas: Gulf Coast Association of Geologic Societies Journal, v. 4, p. 67-87.

Donovan, A. D., Staerker, S., Gardner, R. D., Pope, M. C., Pramudito, A., and Wehner, M. P., 2016, Findings from the Eagle Ford Outcrops of West Texas and Implications to the Subsurface of South Texas, American Association of Petroleum Geologists, ed., The Eagle Ford Shale: A renaissance in U.S. oil production,, Volume AAPG Memoir 110, AAPG, p. 301-336.

Eldrett, J. S., Ma, C., Bergman, S. C., Lutz, B., Gregory, F. J., Dodsworth, P., Phipps, M., Hardas, P., Minisini, D., Ozkan, A., Ramezani, J., Bowring, S. A., Kamo, S. L., Ferguson, K., Macaulay, C., and Kelly, A. E., 2015, An astronomically calibrated stratigraphy of the Cenomanian, Turonian and earliest Coniacian from the Cretaceous Western Interior Seaway, USA: Implications for global chronostratigraphy: Cretaceous Research, v. 56, p. 316-344.

Frébourg, G., Ruppel, S. C., Loucks, R. G., and Lambert, J., 2016, Depositional controls on sediment body architecture in the Eagle Ford/Boquillas system: Insights from outcrops in west Texas, United States: AAPG Bulletin, v. 100, no. 4, p. 657-682.

Freeman, V. L., 1961, Contact of the Boquillas Flags and Austin Chalk in Val Verde and Terrell counties, Texas: American Association of Petroleum Geologists Bulletin, v. 45, p. 105-107.

Freeman, V. L., 1968, Geology of the Comstock-Indian Wells Area Val Verde, Terrell, and Brewster counties, Texas: U.S. Geological Survey Professional Paper, no. 594-K, p. 263.

Gardner, R. D., Pope, M. C., Wehner, M. P., and Donovan, A. D., 2013, Comparative Stratigraphy of the Eagle Ford Group Strata in Lozier Canyon and Antonio Creek, Terrell County, Texas: Transactions- Gulf Coast Association of Geological Societies, v. 63, p. 673-674.

Hackley, P. C., 2012, Geological and geochemical characterization of the Lower Cretaceous Pearsall Formation, Maverick Basin, south Texas: A future shale gas resource?: American Association of Petroleum Geologists Bulletin, v. 96, no. 8, p. 1449-1482.

Hallam, A., 1977, Secular changes in marine inundation of USSR and North America through the Phanerozoic: Nature, v. 269, no. 5631, p. 769-772.

Hancock, J. M., and Kauffman, E. G., 1979, The Great Transgressions Of The Late Cretaceous: Journal of the Geological Society, v. 136, no. 197934, p. 175-186.

Hart, B. S., 2015, The Greenhorn Cyclothem of the Cretaceous Western Interior Seaway: Lithology Trends, Stacking Patterns, Log Signatures, and Application to the Eagle Ford of West Texas: Gulf Coast Association of Geologic Societies Transactions, v. 65, p. 155-174.

Hasegawa, H., Tada, R., Jiang, X., Suganuma, Y., Imsamut, S., Charusiri, P., Ichinnorov, N., and Khand, Y., 2012, Drastic shrinking of the Hadley circulation during the mid-Cretaceous Supergreenhouse: Clim. Past, v. 8, no. 4, p. 1323-1337.

Hazzard, R. T., 1959, Measured Section, *in* Geology of the Val Verde Basin, West Texas Geological Society Guidebook: Midland, p. 118.

Hill, R. T., 1887, The Texas section of the American Cretaceous: American Journal of Science, 3rd Series, v. 34, p. 287-309.

Jacquemyn, C., Huysmans, M., Hunt, D., Casini, G., and Swennen, R., 2015, Multi-scale three-dimensional distribution of fracture- and igneous intrusion-controlled hydrothermal dolomite from digital outcrop model, Latemar platform, Dolomites, northern Italy: AAPG Bulletin, v. 99, no. 5, p. 957-984.

Jones, M. T., and Gislason, S. R., 2008, Rapid releases of metal salts and nutrients following the deposition of volcanic ash into aqueous environments: Geochimica et Cosmochimica Acta, v. 72, no. 15, p. 3661-3680.

Kauffman, E. G., 1977, Geological and Biological Overview: Western Interior Cretaceous Basin: The Mountain Geologist, v. 14, no. 3-4, p. 75-99.

Ladeira, F. L., 1981, Relationship Between Fracture Spacing and Bed Thickness: Journal of Structural Geology, v. 3, no. 2, p. 179-183.

Laubach, S. E., and Jackson, M. L. W., 1990, Origin of Arches in the Northwestern Gulf of Mexico Basin: Geology, v. 18, p. 595-598.

Leberl, F., Gruber, M., and Wiechert, A., Speculative Comparison Between Laser Scanning and 3D Photogrammetry, *in* Proceedings 14th Münchner Fortbildungsseminar Geoinformationssysteme, Muenchen, Deutschland, 2009, Technische Universitaet Muenchen.

Leberl, F., Irschara, A., Pock, T., Meixner, P., Gruber, M., Scholz, S., and Wiechert, A., 2010, Point clouds: Lidar versus 3D Vision: Photogrammetric Engineering & Remote Sensing, v. 76, no. 10, p. 1123-1134.

Lock, B. E., and Peschier, L. S., 2006, Boquillas (Eagle Ford) upper slope sediments, West Texas: Outcrop analogs for potential shale reservoirs: Gulf Coast Association of Geologic Societies Transactions, v. 56, p. 491-508.

Lyon, T. S., 2015, Determining the Depositional Environment of the Lower Eagle Ford in Lozier Canyon, Antonio Creek, and Osman Canyon, Texas: An Outcrop Study of Bedding Features at Outcrop Scale [Master's Thesis]: Texas A&M University, 56 p.

Mauldon, M., and Dershowitz, W., 2000, A multi-dimensional system of fracture abundance measures: Geological Society of America Abstracts with Programs, v. 32, no. 7, p. A474.

Mauldon, M., Dunne, W. M., and Rohrbaugh Jr, M. B., 2001, Circular scanlines and circular windows: new tools for characterizing the geometry of fracture traces: Journal of Structural Geology, v. 23, no. 2–3, p. 247-258.

McGinnis, R. N., Ferrill, D. A., Morris, A. P., Smart, K. J., and Lehrmann, D., 2017, Mechanical stratigraphic controls on natural fracture spacing and penetration: Journal of Structural Geology, In Press, Accepted Manuscript.

McNeal, R. P., 1959, Lithologic Analysis of Sedimentary Rocks: American Association of Petroleum Geologists Bulletin, v. 43, no. 4, p. 854-879.

Miskimins, J. L., 2008, Design and Life Cycle Considerations for Unconventional Reservoir Wells, Society of Petroleum Engineers.

Montgomery, S. L., Petty, A. J., and Post, P. J., 2002, James Limestone, northeastern Gulf of Mexico: Refound opportunity in a Lower Cretaceous trend: American Association of Petroleum Geologists Bulletin, v. 86, no. 3, p. 381-397.

Nearing, M. A., 2004, Expected climate change impacts on soil erosion rates: a review: Journal of Soil and Water Conservation, v. 59, no. 1, no. 1.

Nichols, G., 2009, Sedimentology and Stratigraphy, West Sussex, UK, John Wiley & Sons, Ltd.

Norris, R. D., Bice, K. L., Magno, E. A., and Wilson, P. A., 2002, Jiggling the tropical thermostat in the Cretaceous hothouse: Geological Society of America, v. 30, no. 4, p. 299-302.

Peschier, L. S., 2006, The depositional environments of the Boquillas Formation, West Texas: M.S. Thesis, University of Louisiana at Lafayette, p. 82.

Pessagno, E. A., 1969, Upper Cretaceous Stratigraphy of the Western Gulf Coast Area of México, Texas, and Arkansas: Geological Society of America Memoirs, v. 111, p. 1-139.

Pierce, J. D., Ruppel, S. C., Rowe, H., and Stockli, D. F., 2016, Zircon U-Pb Geochronology and Sources of Volcanic Ash Beds in the Upper Cretaceous Eagle Ford Shale, South Texas: Gulf Coast Association of Geologic Societies Journal, v. 5, p. 253-274.

Price, N. J., 1966, Fault and Joint Development in Brittle and Semi-Brittle Rock, Oxford, Pergamon Press.

Qiao, Z., Shen, A., Zheng, J., Chang, S., and Chen, Y., 2015, Three-dimensional carbonate reservoir geomodeling based on the digital outcrop model: Petroleum Exploration and Development, v. 42, no. 3, p. 358-368.

Railroad Commision of Texas, 2016, Eagle Ford Shale Information: http://www.rrc.state.tx.us/oil-gas/major-oil-gas-formations/eagle-ford-shale/.

Russell, W. L., 1945, Relation of Radioactivity, Organic Content, and Sedimentation: American Association of Petroleum Geologists Bulletin, v. 29, no. 10, p. 1470-1494.

Sageman, B. B., Rich, J., Arthur, M. A., Birchfield, G. E., and Dean, W. E., 1997, Evidence for Milankovitch Periodicities in Cenomanian-Turonian Lithologic and Geochemical Cycles, Western Interior U.S.A.: Journal of Sedimentary Research, Section B: Stratigraphy and Global Studies, v. 67, no. 2, p. 286-302.

Schlanger, S. O., and Jenkyns, H. C., 1976, Cretaceous Oceanic Anoxic Events: Causes and Consequences: Geologie en Mijnbouw, v. 55, p. 179-184.

Scholle, P. A., Bebout, D. G., and Moore, C. H., 1983, Carbonate Depositional Environments, Tulsa, OK, American Association of Petroleum Geologists, AAPG Memoir.

Sloss, L. L., 1963, Sequences in the Cratonic Interior of North America: Geological Society of America Bulletin, v. 74, no. 2, p. 93-114.

Tian, Y., Ayers, W. B., and McCain, W. D., 2012, Regional analysis of stratigraphy, reservoir characteristics, and fluid phases in the Eagle Ford Shale, South Texas: Gulf Coast Association of Geologic Societies Transactions, v. 62, p. 471-483.

Trevino, R. H., 1988, Facies and depositional environments of the Boquillas Formation, Upper Cretaceous of southwest Texas: M.S. Thesis, University of Texas at Arlington, p. 135.

Tucker, M. E., and Wright, V. P., 1990, Carbonate Sedimentology, Blackwell Science Ltd, a Blackwell Publishing Company.

U.S. Energy Information Administration, 2015, Monthly Energy Review November 2015, Office of Energy Statistics, Monthly Energy Review, U.S. Department of Energy, p. 1-224, https://www.eia.gov/totalenergy/data/monthly/archive/00351511.pdf.

Wehner, M., Tice, M. M., Pope, M. C., Gardner, R., Donovan, A. D., and Staerker, T. S., 2015, Anoxic, Storm Dominated Inner Carbonate Ramp Deposition of Lower Eagle Ford Formation, West Texas, Society of Petroleum Engineers.

Winker, C. D., and Buffler, R. T., 1988, Paleogeographic evolution of early deepwater Gulf of Mexico and margins, Jurassic to Middle Cretaceous (Comanchean): American Association of Petroleum Geologists Bulletin, v. 72, no. 3, p. 318-346.

Workman, S. J., 2013, Integrating Depositional Facies and Sequence Stratigraphy in Characterizing Unconventional Reservoirs: Eagle Ford Shale, South Texas [Master's Thesis]: Western Michigan University, 141 p.

Wu, H., and D. Pollard, D., 1995, An experimental study of the relationship between joint spacing and layer thickness: Journal of Structural Geology, v. 17, no. 6, p. 887-905.

Young, K., 1972, Cretaceous Paleogeography: Implications of Endmeic Ammonite Faunas: The Bureau of Economic Geology, The University of Texas, Geological Circular, v. 72, no. 2, p. 13.

APPENDIX A – UAV FLIGHT MAPS & STATISTICS

North Lozier Canyon – Scott Ranch Site (Map View)

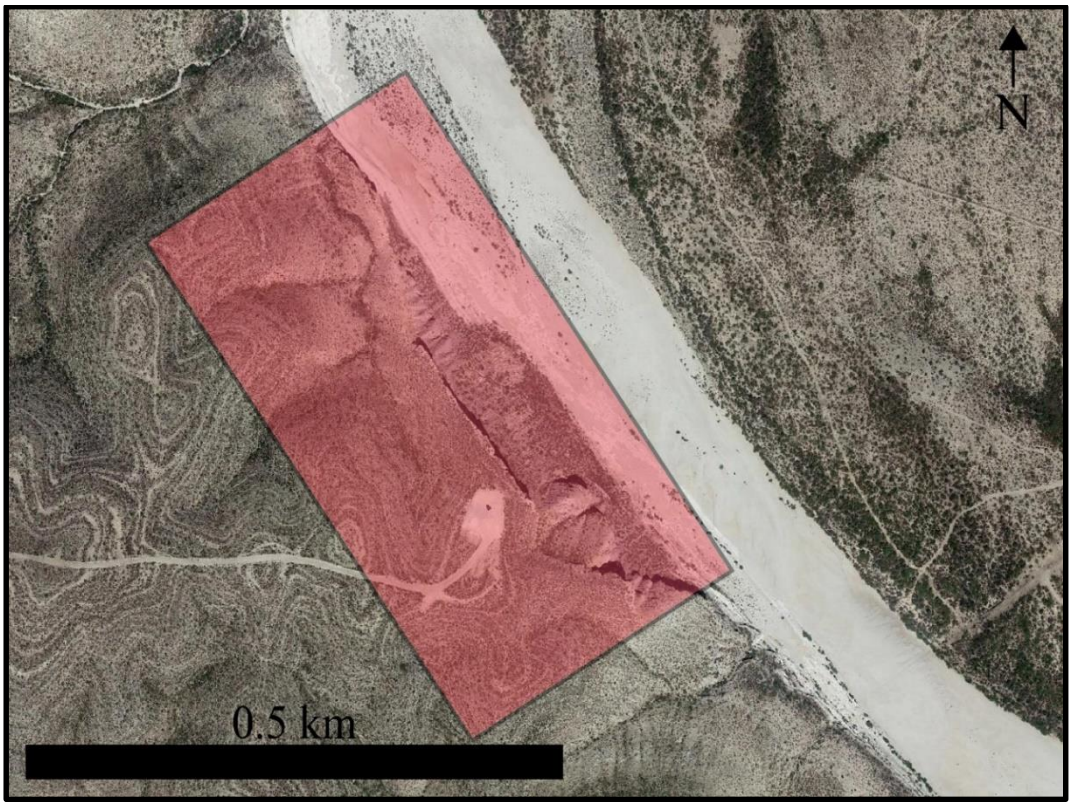

Figure A-1. Satellite image of the Scott Ranch site in North Lozier Canyon. The area imaged in map view is highlighted in red.

Table A-1. Flight information for map view imaging at the Scott Ranch site in North Lozier Canyon.

North Lozier Canyon - Scott Ranch Site - Map View - June 28th, 2015					
	Flight Number	**Takeoff Time**	**Landing Time**	**Flight Duration**	**Total Photos**
	1	11:40 AM	12:01 PM	21 min.	282
TOTAL	1			21 min.	282

North Lozier Canyon – Scott Ranch Site (Outcrop Face)

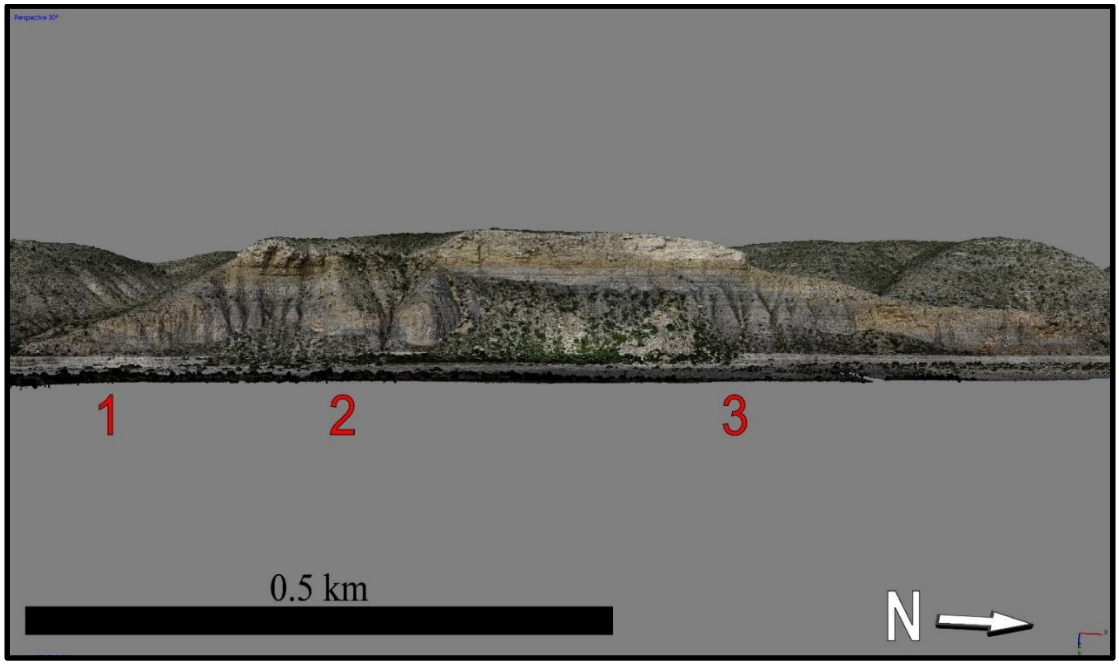

Figure A-2. UAV Digital Outcrop Model of the Scott Ranch site in North Lozier Canyon. The numbers in red correspond to drone flights and illustrate what section of outcrop was imaged in each flight.

Table A-2. Flight information for imaging outcrop faces at the Scott Ranch site in North Lozier Canyon.

North Lozier Canyon - Scott Ranch Site - Outcrop Faces - June 28th, 2015					
	Flight Number	**Takeoff Time**	**Landing Time**	**Flight Duration**	**Total Photos**
	1	9:50 AM	9:53 AM	3 min.	44
	2	9:59 AM	10:12 AM	13 min.	149
	3	10:30 AM	10:42 AM	12 min.	173
TOTAL	3			28 min.	366

South Lozier Canyon – Colonel Neck (Map View)

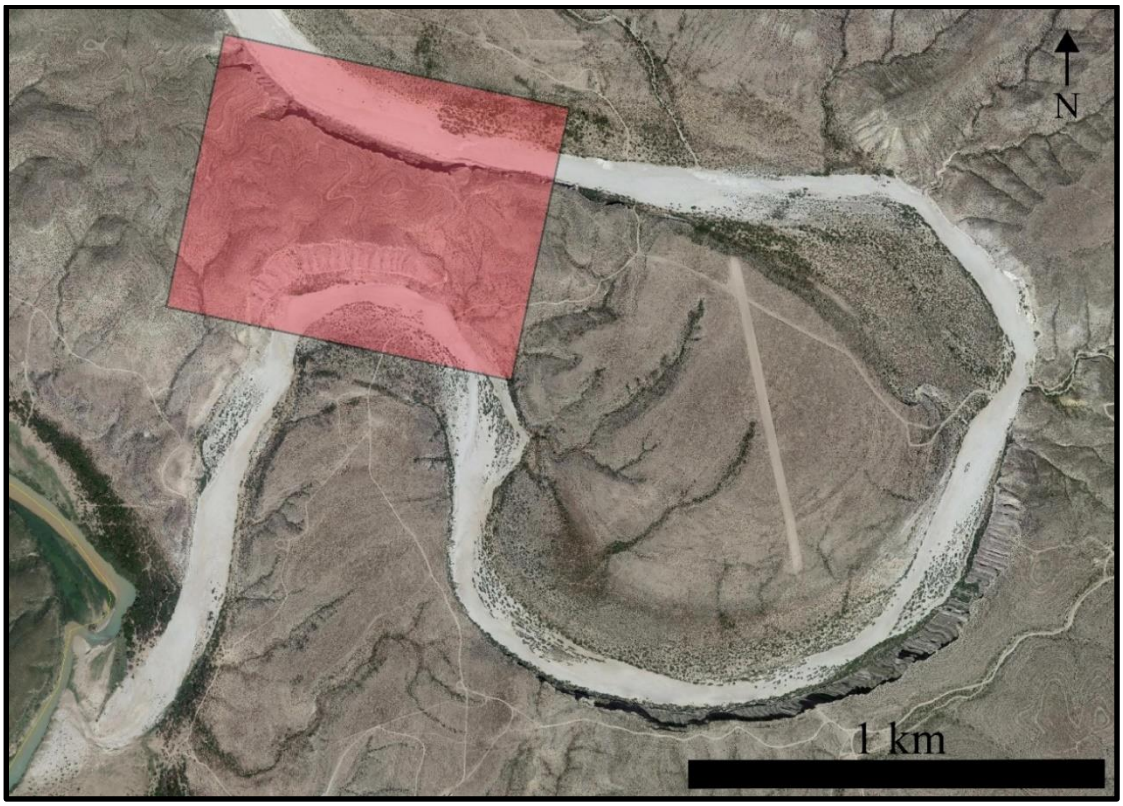

Figure A-3. Satellite image of the Colonel Neck site in South Lozier Canyon. The area imaged in map view is highlighted in red.

Table A-3. Flight Information for map view imaging at Colonel Neck site in South Lozier Canyon

South Lozier Canyon - Colonel Neck - Map View - June 27th, 2015					
	Flight Number	**Takeoff Time**	**Landing Time**	**Flight Duration**	**Total Photos**
	1	1:20 PM	1:35 PM	15 min.	185
	2	2:14 PM	2:30 PM	16 min.	203
TOTAL				31 min.	388

South Lozier Canyon – Colonel Neck (Outcrop Face)

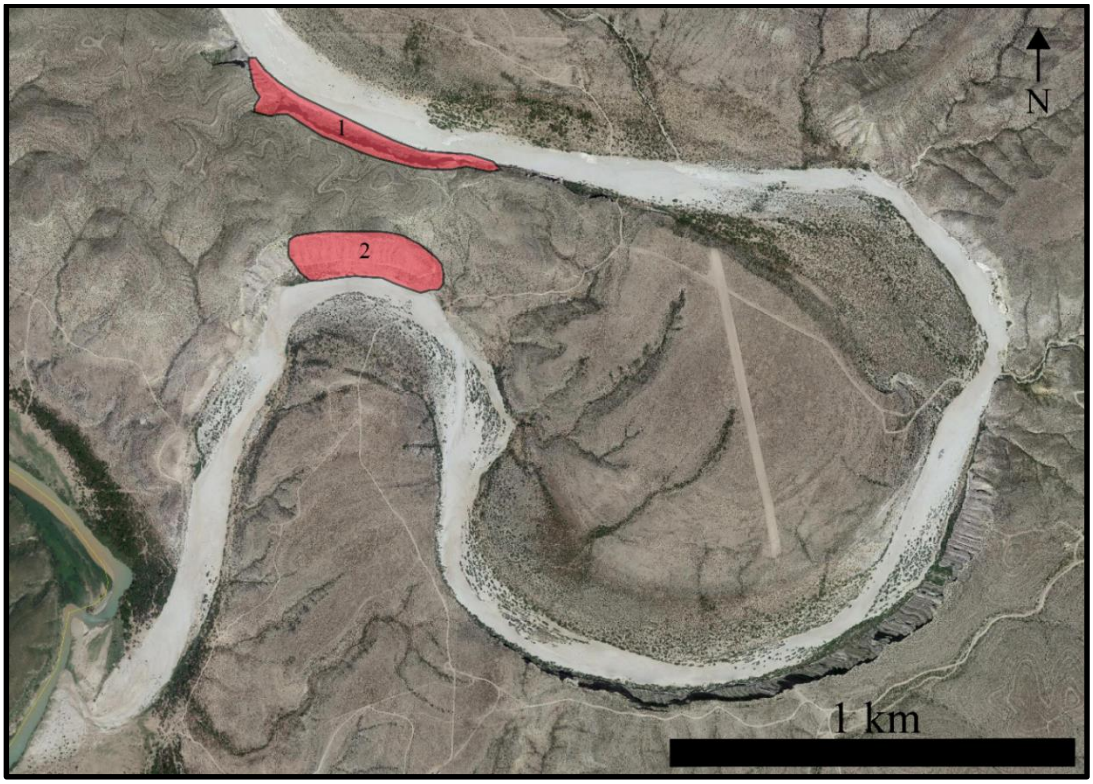

Figure A-4. Satellite image of the Colonel Neck site in South Lozier Canyon. Imaged Eagle Ford outcrop is highlighted in red. Numbers correspond to drone flights and illustrate what section of outcrop was imaged in each flight. The first flight (1) imaged Colonel Neck North. The second flight (2) imaged Colonel Neck South.

Table A-4. Flight information for imaging outcrop faces at Colonel Neck in South Lozier Canyon.

South Lozier Canyon - Colonel Neck - Outcrop Faces - November 3rd, 2015					
	Flight Number	**Takeoff Time**	**Landing Time**	**Flight Duration**	**Total Photos**
	1 – Col. Neck N	9:15 AM	9:45 AM	30 min.	131
	2 - Col. Neck S	4:20 PM	4:45 PM	25 min.	61
TOTAL	2			55 min.	192

South Lozier Canyon – Colonel Bend (Map View)

Figure A-5. Satellite image of the Colonel Bend site in South Lozier Canyon. The area imaged in map view is highlighted in red.

Table A-5. Flight information for map view imaging at Colonel Bend in South Lozier Canyon.

South Lozier Canyon - Colonel Bend - Map View - June 27th, 2015					
	Flight Number	**Takeoff Time**	**Landing Time**	**Flight Duration**	**Total Photos**
	1	5:41 PM	5:50 PM	9 min.	146
TOTAL	1			9 min.	146

South Lozier Canyon – Colonel Bend (Outcrop Faces)

Figure A-6. Satellite image of the Colonel Bend site in South Lozier Canyon. Imaged Eagle Ford outcrop is highlighted in red. Numbers correspond to drone flights and illustrate what section of outcrop was imaged in each flight.

Table A-6. Flight information for imaging outcrop faces at Colonel Bend in South Lozier Canyon.

South Lozier Canyon - Colonel Bend - Outcrop Faces - November 3rd, 2015					
	Flight Number	**Takeoff Time**	**Landing Time**	**Flight Duration**	**Total Photos**
	1	10:25 AM	10:35 AM	10 min.	89
	2	10:50 AM	11:01 AM	11 min.	84
	3	11:30 AM	11:45 AM	15 min.	124
	4	12:33 PM	12:41 PM	8 min.	75
	5	12:50 PM	1:03 PM	13 min.	34
	6	3:10 PM	3:18 PM	8 min.	59
	7	3:23 PM	3:30 PM	7 min.	55
	8	3:39 PM	3:47 PM	8 min.	81
	9	4:00 PM	4:12 PM	12 min.	101
TOTAL	9			92 min.	702

Antonio Creek (Map View)

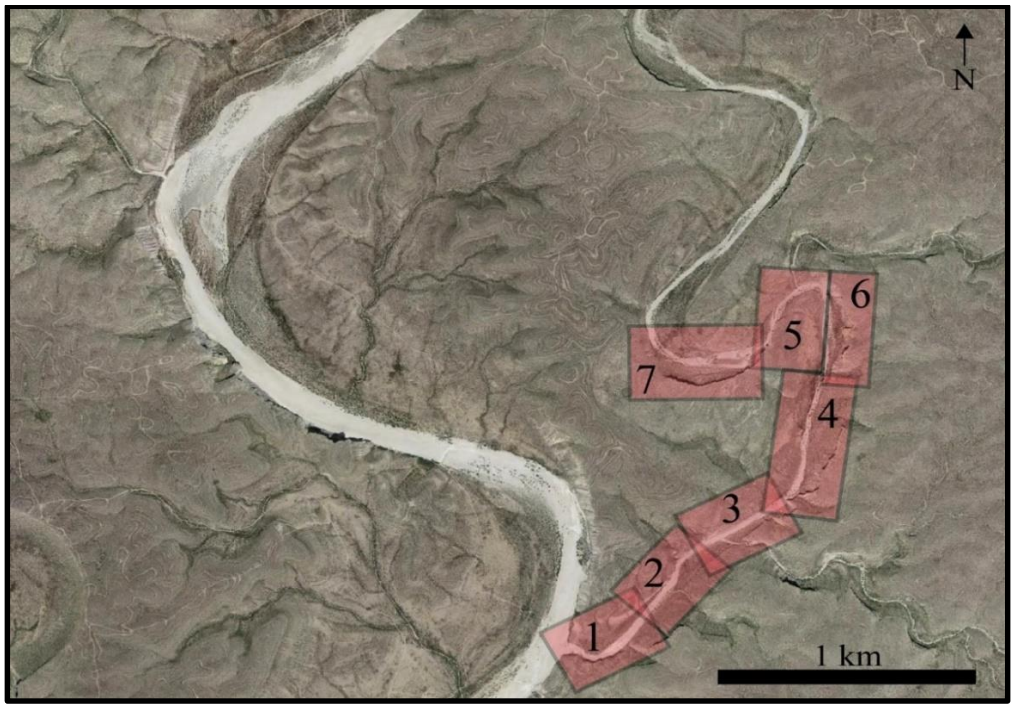

Figure A-7. Satellite image of Antonio Creek. The area imaged in map view is highlighted in red. Numbers correspond to drone flights and illustrate what section of outcrop was imaged in each flight.

Table A-7. Flight information for map view imaging in Antonio Creek.

Antonio Creek - Map View - November 4th, 2015					
	Flight Number	**Takeoff Time**	**Landing Time**	**Flight Duration**	**Total Photos**
	1	9:30 AM	9:43 AM	13 min.	179
	2	9:54 AM	10:03 AM	9 min.	86
	3	10:18 AM	10:31 AM	13 min.	200
	4	10:49 AM	11:07 AM	18 min.	263
	5	11:19 AM	11:36 PM	17 min.	181
	6	11:47 AM	12:02 PM	15 min.	148
	7	12:16 PM	12:37 PM	21 min.	293
TOTAL	7			106 min.	1350

Antonio Creek (Outcrop Face)

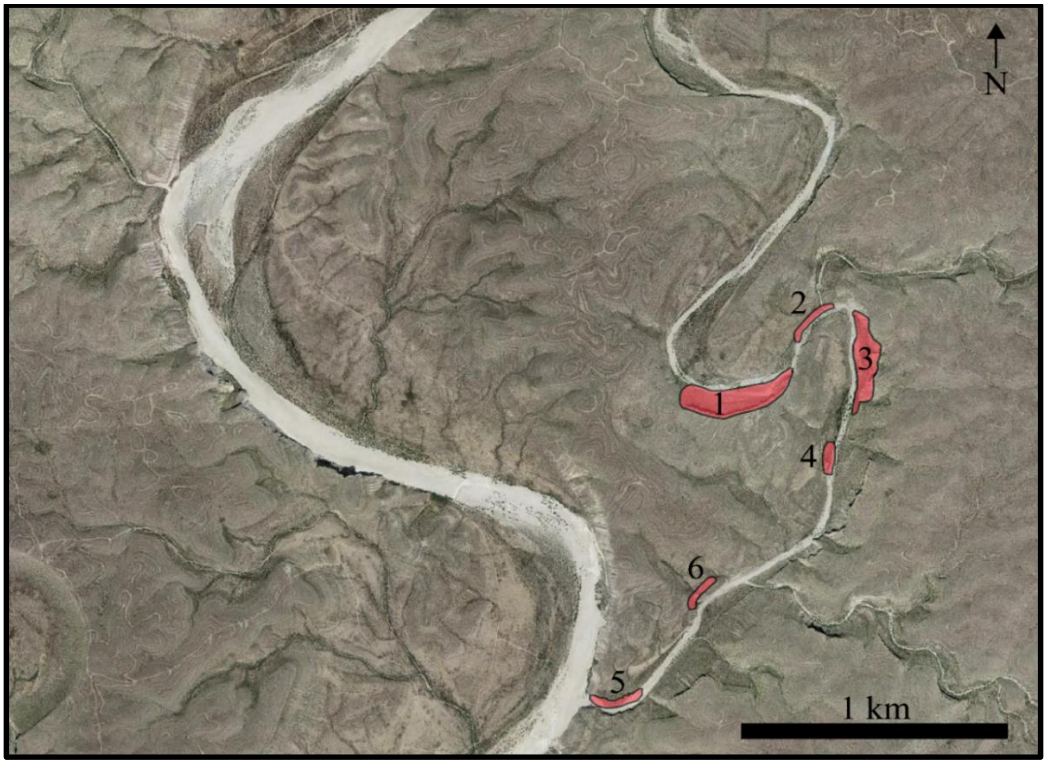

Figure A-8. Satellite image of outcrop faces imaged in Antonio Creek. Imaged Eagle Ford outcrop is highlighted in red. Numbers correspond to drone flights and illustrate what section of outcrop was imaged in each flight.

Table A-8. Flight information for imaging outcrop faces in Antonio Creek.

Antonio Creek - Outcrop Faces - November 4th, 2015					
	Flight Number	**Takeoff Time**	**Landing Time**	**Flight Duration**	**Total Photos**
	1	2:20 PM	2:29 PM	9 min.	48
	2	2:39 PM	2:50 PM	11 min.	70
	3	3:00 PM	3:02 PM	2 min.	20
	4	3:12 PM	3:14 PM	2 min.	13
	5	3:49 PM	4:00 PM	11 min.	85
	6	4:30 PM	4:35 PM	5 min.	22
TOTAL	6			40 min.	258

APPENDIX B – CAMERA CALIBRATIONS

Table B-1. Camera Calibrations for the Sony ILCE 5100 camera.

Sony ILCE 5100 – Aerial Map View			
f	5207.39		
cx	-40.4829	**b1**	-0.485211
cy	-27.1492	**b2**	0.374856
k1	-0.155764	**p1**	-0.000391405
k2	0.0770601	**p2**	0.000373821
k3	0.194923	**p3**	0
k4	-0.166523	**p4**	0

Table B-2. Camera Calibrations for the DJI FC550 camera.

DJI FC550 – Outcrop Face View			
f	3083.01		
cx	-757.902	**b1**	190.924
cy	7.49438	**b2**	8.06674
k1	0.0161689	**p1**	0.00155532
k2	-0.00479289	**p2**	-0.000273568
k3	-0.00231415	**p3**	0
k4	0.00213492	**p4**	0

APPENDIX C – STATISTICS OF APPARENT FRACTURE EXTENTS

FACIES B

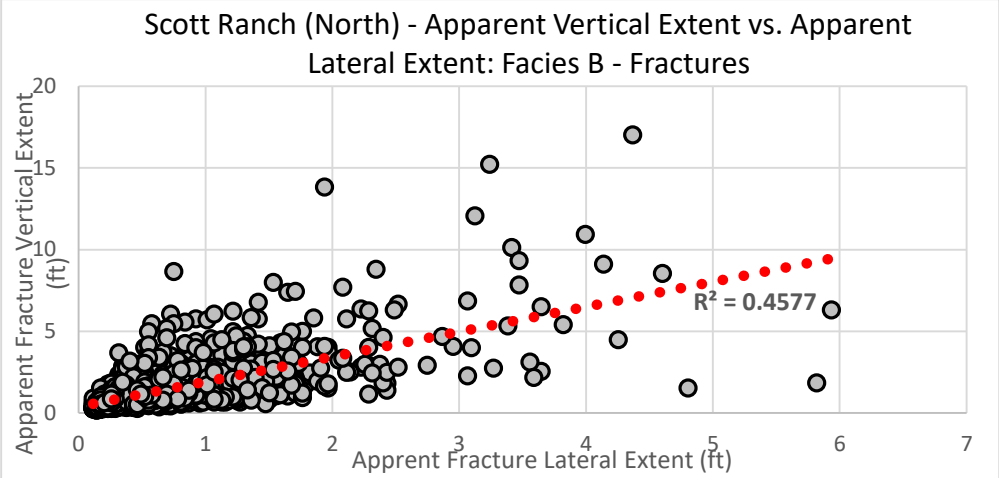

Figure C-1. Scatter plot of apparent fracture lateral extent (x-axis) vs. apparent fracture vertical extent (y-axis) at the Scott Ranch (North) site for fractures identified in 2-D orthomosaics of Eagle Ford group Facies B. The linear trend line is shown in red dots and the regression coefficient is displayed in bold.

Table C-1. Statistics for SRN Apparent Lateral Extent.

Facies B: Apparent Lateral Extent (ft)	
Mean	0.57
Standard Error	0.01
Median	0.38
Mode	0.17
Standard Deviation	0.56
Sample Variance	0.31
Kurtosis	18.74
Skewness	3.51
Range	5.82
Minimum	0.11
Maximum	5.94
Sum	1160.61
Count	2040
Confidence Level (95.0%)	0.02

Table C-2 Statistics for SRN Apparent Vertical Extent.

Facies B: Apparent Vertical Extent (ft)	
Mean	1.27
Standard Error	0.03
Median	0.90
Mode	0.58
Standard Deviation	1.26
Sample Variance	1.60
Kurtosis	34.82
Skewness	4.64
Range	16.85
Minimum	0.17
Maximum	17.02
Sum	2582.19
Count	2040
Confidence Level (95.0%)	0.05

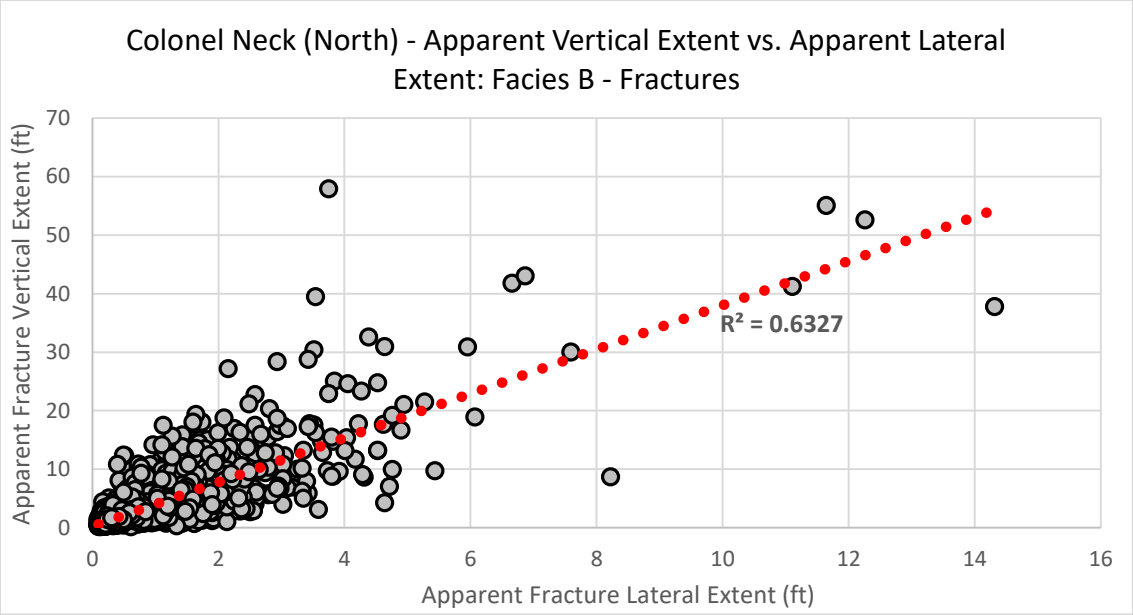

Figure C-2. Scatter plot of apparent fracture lateral extent (x-axis) vs. apparent fracture vertical extent (y-axis) at the Colonel Neck (North) site for fractures identified in 2-D orthomosaics of Eagle Ford group Facies B. The linear trend line is shown in red dots and the regression coefficient is displayed in bold.

Table C-3. Statistics for CNN Apparent Lateral Extent.

.

Facies B: Apparent Lateral Extent (ft)	
Mean	0.70
Standard Error	0.01
Median	0.47
Mode	0.26
Standard Deviation	0.82
Sample Variance	0.68
Kurtosis	61.65
Skewness	5.84
Range	14.22
Minimum	0.10
Maximum	14.32
Sum	2279.33
Count	3261
Confidence Level (95.0%)	0.03

Table C-4. Statistics for CNN Apparent Vertical Extent

Facies B: Apparent Vertical Extent (ft)	
Mean	2.84
Standard Error	0.07
Median	1.66
Mode	0.75
Standard Deviation	3.91
Sample Variance	15.32
Kurtosis	51.10
Skewness	5.70
Range	57.74
Minimum	0.16
Maximum	57.91
Sum	9275.10
Count	3261
Confidence Level (95.0%)	0.13

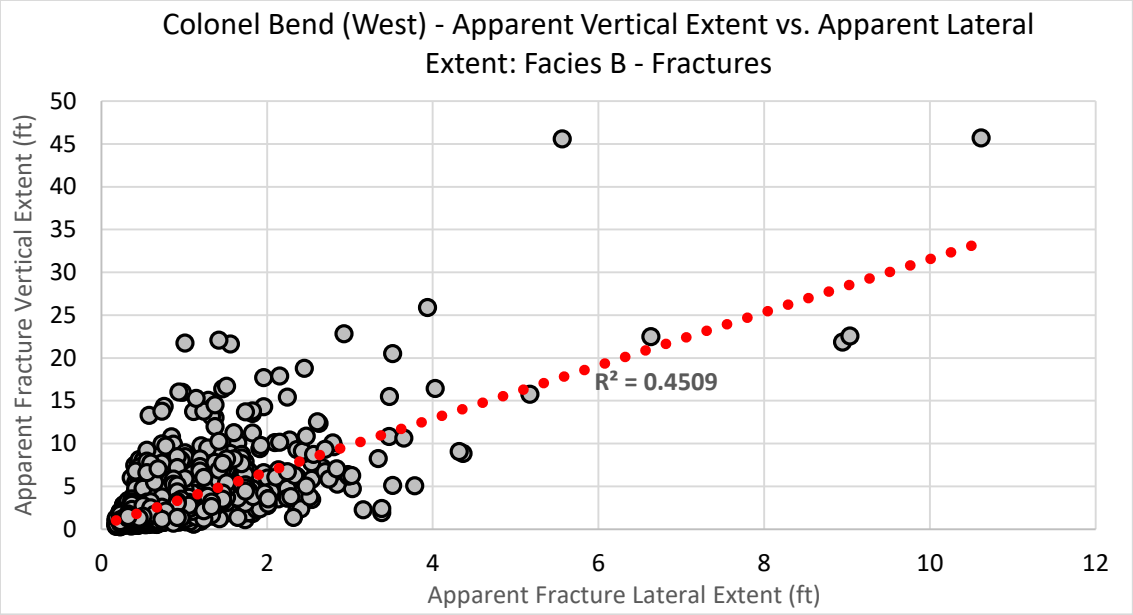

Figure C-3. Scatter plot of apparent fracture lateral extent (x-axis) vs. apparent fracture vertical extent (y-axis) at the Colonel Bend (West) site for fractures identified in 2-D orthomosaics of Eagle Ford group Facies B. The linear trend line is shown in red dots and the regression coefficient is displayed in bold.

Table C-5. Statistics for CBW Apparent Lateral Extent.

Facies B: Apparent Lateral Extent (ft)	
Mean	0.70
Standard Error	0.01
Median	0.55
Mode	0.36
Standard Deviation	0.60
Sample Variance	0.36
Kurtosis	65.18
Skewness	5.83
Range	10.44
Minimum	0.18
Maximum	10.62
Sum	1908.14
Count	2707
Confidence Level (95.0%)	0.02

Table C-6. Statistics for CBW Apparent Vertical Extent.

Facies B: Apparent Vertical Extent (ft)	
Mean	2.64
Standard Error	0.05
Median	1.83
Mode	1.60
Standard Deviation	2.76
Sample Variance	7.63
Kurtosis	55.28
Skewness	5.44
Range	45.46
Minimum	0.27
Maximum	45.72
Sum	7147.80
Count	2707
Confidence Level (95.0%)	0.10

FACIES C

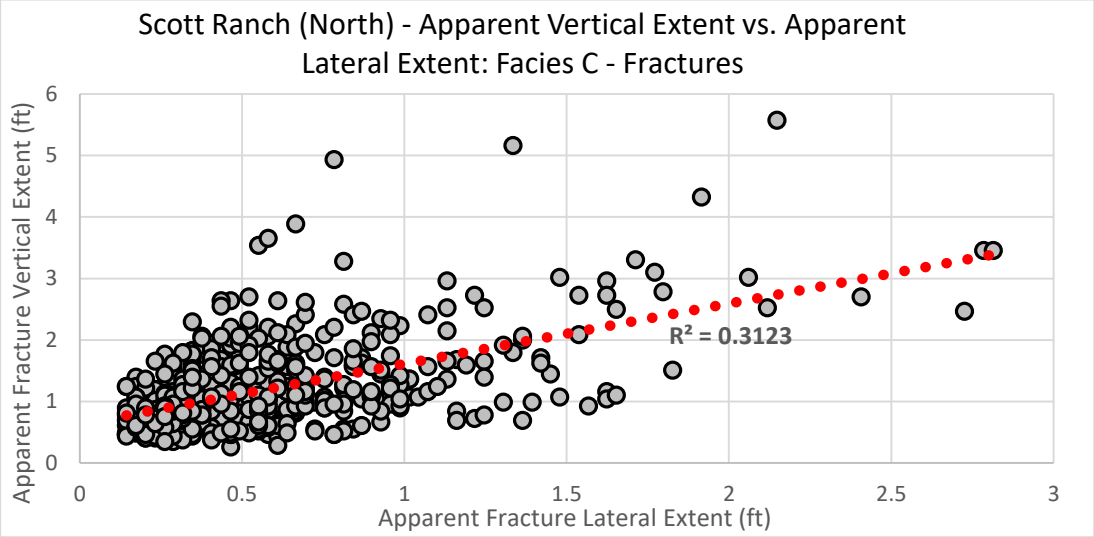

Figure C-4. Scatter plot of apparent fracture lateral extent (x-axis) vs. apparent fracture vertical extent (y-axis) at the Scott Ranch (North) site for fractures identified in 2-D orthomosaics of Eagle Ford group Facies C. The linear trend line is shown in red dots and the regression coefficient is displayed in bold.

Table C-7. Statistics for SRN Apparent Lateral Extent.

Facies C: Apparent Lateral Extent (ft)	
Mean	0.54
Standard Error	0.02
Median	0.44
Mode	0.29
Standard Deviation	0.38
Sample Variance	0.15
Kurtosis	7.76
Skewness	2.35
Range	2.67
Minimum	0.14
Maximum	2.81
Sum	338.75
Count	626
Confidence Level (95.0%)	0.03

Table C-8. Statistics for SRN Apparent Vertical Extent.

Facies C: Apparent Vertical Extent (ft)	
Mean	1.16
Standard Error	0.02
Median	0.99
Mode	0.67
Standard Deviation	0.67
Sample Variance	0.45
Kurtosis	7.87
Skewness	2.24
Range	5.31
Minimum	0.26
Maximum	5.57
Sum	728.07
Count	626
Confidence Level (95.0%)	0.05

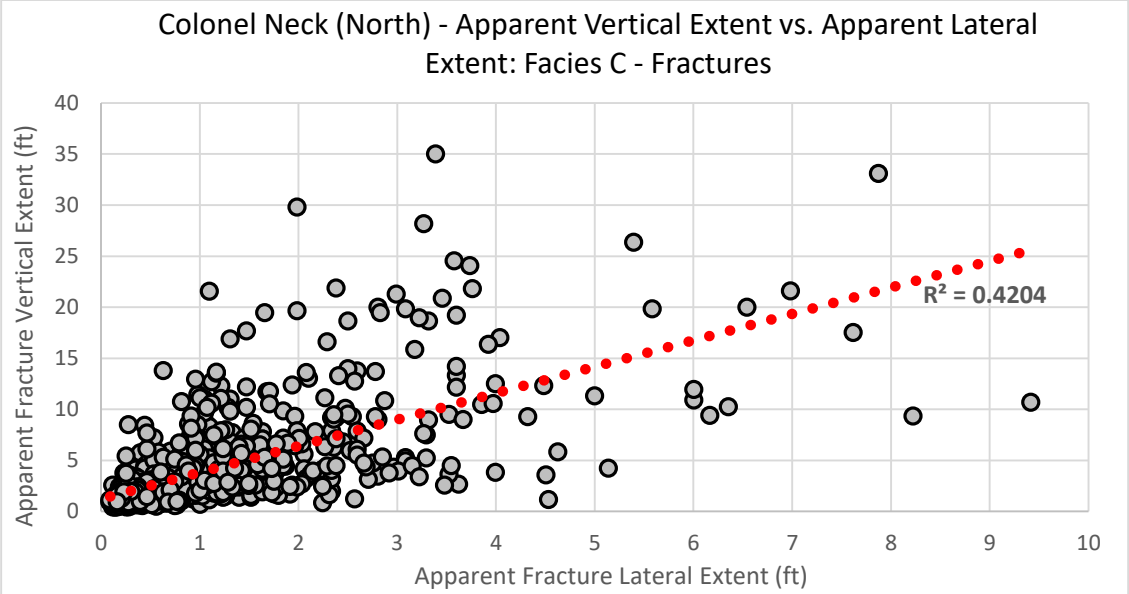

Figure C-5. Scatter plot of apparent fracture lateral extent (x-axis) vs. apparent fracture vertical extent (y-axis) at the Colonel Neck (North) site for fractures identified in 2-D orthomosaics of Eagle Ford group Facies C. The linear trend line is shown in red dots and the regression coefficient is displayed in bold.

Table C-9. Statistics for CNN Apparent Lateral Extent.

Facies C: Apparent Lateral Extent (ft)	
Mean	1.13
Standard Error	0.04
Median	0.77
Mode	0.26
Standard Deviation	1.14
Sample Variance	1.29
Kurtosis	11.05
Skewness	2.78
Range	9.32
Minimum	0.09
Maximum	9.42
Sum	929.51
Count	824
Confidence Level (95.0%)	0.08

Table C-10. Statistics for CNN Apparent Vertical Extent.

Facies C: Apparent Vertical Extent (ft)	
Mean	4.16
Standard Error	0.16
Median	2.57
Mode	1.56
Standard Deviation	4.53
Sample Variance	20.54
Kurtosis	10.06
Skewness	2.80
Range	34.58
Minimum	0.42
Maximum	35
Sum	3428.70
Count	824
Confidence Level (95.0%)	0.31

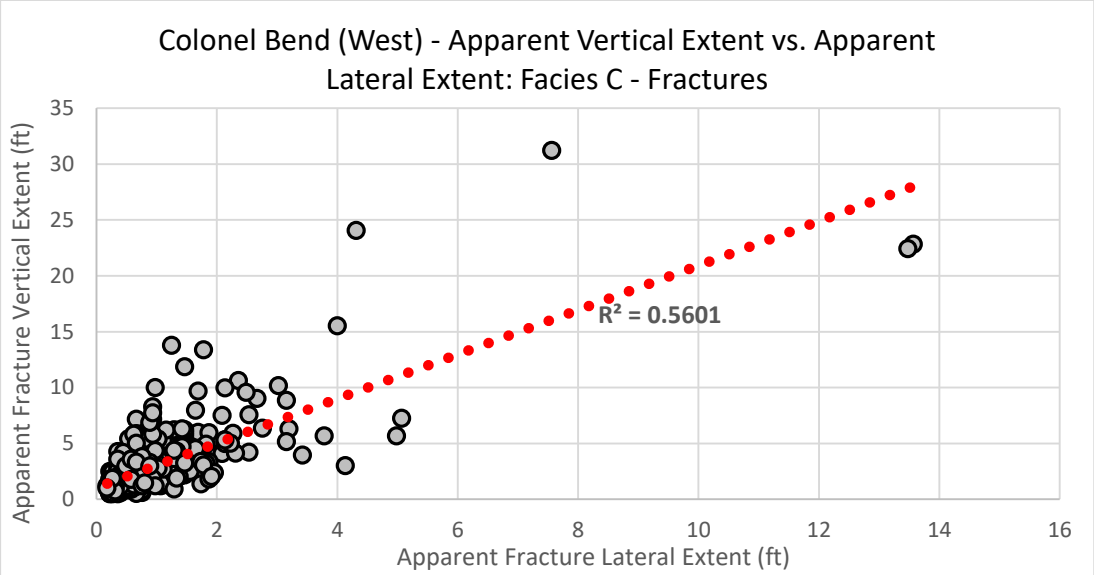

Figure C-6. Scatter plot of apparent fracture lateral extent (x-axis) vs. apparent fracture vertical extent (y-axis) at the Colonel Bend (West) site for fractures identified in 2-D orthomosaics of Eagle Ford group Facies C. The linear trend line is shown in red dots and the regression coefficient is displayed in bold.

Table C-11. Statistics for CBW Apparent Lateral Extent.

Facies C: Apparent Lateral Extent (ft)	
Mean	0.87
Standard Error	0.04
Median	0.67
Mode	0.31
Standard Deviation	0.97
Sample Variance	0.94
Kurtosis	93.82
Skewness	8.11
Range	13.39
Minimum	0.18
Maximum	13.57
Sum	557.50
Count	638
Confidence Level (95.0%)	0.076

Table C-12. Statistics for CBW Apparent Vertical Extent.

Facies C: Apparent Vertical Extent (ft)	
Mean	2.78
Standard Error	0.10
Median	2.14
Mode	1.16
Standard Deviation	2.58
Sample Variance	6.66
Kurtosis	42.04
Skewness	5.27
Range	30.74
Minimum	0.49
Maximum	31.23
Sum	1774.32
Count	638
Confidence Level (95.0%)	0.20